Charles University in Prague
Faculty of Mathematics and Physics

DOCTORAL THESIS

Štěpán Uxa

Transport and optical properties of CdTe/CdZnTe single crystals

Institute of Physics of Charles University

Supervisor of the doctoral thesis:	Assoc. Prof. Eduard Belas, PhD
Study programme:	Physics
Specialization:	Quantum Optics and Optoelectronics

Prague 2014

Acknowledgement

I would like to express my gratitude to my supervisor Assoc. Prof. Eduard Belas and to Assoc. Prof. Roman Grill for their invaluable help and challenging consultations. I would also like to thank to Prof. Jan Franc, Assoc. Prof. Pavel Hlídek, and other colleagues from the Institute of Physics of Charles University for their contributions to this work and their help with my research and study.

I declare that I carried out this doctoral thesis independently, and only with the cited sources, literature and other professional sources.

I understand that my work relates to the rights and obligations under the Act No. 121/2000 Coll., the Copyright Act, as amended, in particular the fact that the Charles University in Prague has the right to conclude a license agreement on the use of this work as a school work pursuant to Section 60 paragraph 1 of the Copyright Act.

In Prague, August 4, 2014 Štěpán Uxa

Název práce: Transportní a optické vlastnosti monokrystalů CdTe/CdZnTe

Autor: Štěpán Uxa

Katedra: Fyzikální ústav UK

Vedoucí disertační práce: doc. Ing. Eduard Belas, CSc., Fyzikální ústav UK

Abstrakt: Práce je zaměřena na studium vnitřního elektrického pole a teplotní závislosti absorpční hrany vzorků CdTe a CdZnTe. V první části práce je studováno elektrické pole rovinných detektorů záření pomocí metody přechodných proudů (TCT). Je představena ucelená teorie propojující TCT měření s měřeními účinnosti sběru náboje (CCE) studovaného detektoru, vedoucí ve výsledku k vyvinutí dvou nových iteračních metod pro zpracování experimentálních dat. Tyto metody mohou být použity vždy, kdy lze vnitřní elektrické pole v detektoru aproximovat lineárních profilem. V druhé části práce jsou představena vysokoteplotní měření propustnosti tenkých vzorků CdTe, z nichž je vyhodnocena teplotní závislost šířky zakázaného pásu. Je to zároveň poprvé, kdy byla taková měření provedena ve zvýšeném tlaku kadmiových par, což významně snižuje sublimaci vzorků během měření.

Klíčová slova: CdTe, metoda přechodných proudů, elektrické pole, absorpční hrana, šířka zakázaného pásu

Title: Transport and optical properties of CdTe/CdZnTe single crystals

Author: Štěpán Uxa

Department: Institute of Physics of Charles University

Supervisor: Assoc. Prof. Eduard Belas, PhD, Institute of Physics of Charles University

Abstract: The thesis is focused on a study of internal electric field and temperature dependence of the absorption edge of CdTe and CdZnTe samples. In the first part of the thesis the transient-current technique (TCT) is used for investigations of electric fields within planar radiation detectors. The original comprehensive theory that links together TCT measurements with measurements of detector's charge-collection efficiency (CCE) is presented. This approach results in the development of two new iterative methods for processing of experimental data which can be used in any situation when the internal electric field can be approximated by a linear profile. In the second part of the thesis high temperature measurements of transmittance of thin polished CdTe samples are presented, leading to the estimation of the temperature dependence of the bandgap energy from calculated spectra of absorption coefficient. This is for the first time when measurements in a Cd overpressure have been performed which significantly reduces sample sublimation.

Keywords: CdTe, transient-current technique, electric field, absorption edge, bandgap energy

Contents

Preface

With the development of semiconductor technology after the Second World War, Si and Ge became the common materials used for X-ray and γ-ray spectrometers since they offered better resolution as compared to other detectors (gas chambers, proportional counters, scintillators) available at the time. However, in the following years some disadvantages of these materials appeared, limiting their use in certain applications. These were, in the case of Si, low sensitivity of detection of radiation with energy higher than several tens of keV, and, in the case of Ge, its relatively high volume (up to 100 cm^3) necessary for efficient operation. Because of their small bandgaps (1.12 eV for Si, 0.67 eV for Ge at 300 K), both materials must have been cooled down to liquid nitrogen temperatures to avoid excessive thermal currents. In the consequent search for a new material of high detection ability that could be operated at room temperature while lower volumes of the material would be needed, Cadmium-Telluride (CdTe) has proved to be a proper candidate.

In the 1950s first detailed investigations of CdTe were made and since then numerous papers reporting various properties and applications have been published. The first comprehensive studies were published in 1955 by Kröger and de Nobel [1], and by Boltaks, Konorov, and Matveev [2], followed by the work of de Nobel [3], where basic structural, electrical, and optical properties were reported. Simultaneously with the development of CdTe, two related compounds were being examined: Cadmium-Mercury-Telluride (HgCdTe, CMT) and Cadmium-Zinc-Telluride (CdZnTe, CZT). Due to the feasibility of tuning the bandgap energy of CMT in the range of 0–1.5 eV by controlling of the Hg mole fraction, from late 1960s it played a major role in infrared (IR) detection systems covering the most important IR range from 1 to 14 μm (including two important atmospheric windows: 3–5 μm and 8–14 μm). Because of its high IR absorption coefficient, thin CMT films (thickness around 10 μm) were sufficient for efficient detection. Preparation of thin films further stimulated the development of epitaxial techniques in 1980s—LPE, MOCVD, MBE, etc. In order to reduce the amount of defects and stress between a thin film and a substrate, epitaxial films of CMT were prepared with success on CZT because of excellent matching of their lattice constants. High IR transmissivity of CZT enabled the deposition of a thin CMT film on the backside of the CZT substrate to protect the film. Developments in the crystal growth of CZT that should originally serve as a substrate for epitaxial layers later approved that CZT itself can efficiently operate as a radiation detector as well as CdTe does, and, moreover, it overcomes CdTe in particular properties, e.g., resistivity at room temperature. Both these materials have been studied intensively due to their potential applications in detecting X-ray and γ-ray radiation [4, 5].

In the field of radiation detectors, independently of which semiconductor material is employed, there are certain material properties required for the realization of high performance spectrometers that provide both good spectral resolution and high counting efficiency. Key properties can be summarized as follows [6]:

(i) High atomic number, Z, for efficient radiation–atomic interactions.

(ii) Large enough bandgap for high resistivity and low leakage current at room temperature. Low leakage currents are critical for low noise operation; high resistivity ($> 10^9\ \Omega\,\mathrm{cm}$) is achieved by using larger bandgap materials with low intrinsic carrier concentrations and by controlling the extrinsic and intrinsic defects to pin the Fermi level near the midgap. Values above about 1.5 eV are normally needed.

(iii) Small enough bandgap so that the electron–hole ionization energy is small (<5 eV). This results in the number of generated electron–hole pairs being reasonably large and the statistical variation small, ensuring higher signal-to-noise ratio.

(iv) High intrinsic mobility–lifetime product, $\mu\tau$, for efficient charge collection. Since the charge collection is determined by what fraction of the detector thickness photogenerated electrons and holes traverse during the time when charge is collected, the carrier drift length is required to be far greater than the detector thickness to ensure complete collection.

(v) High-purity, homogeneous, defect-free material with acceptable cross-sectional area and thickness. For high sensitivity and efficiency, large detector (single-crystal) volumes are required to ensure that as many incident photons as possible have the opportunity to interact in the detector volume. The requirement of homogeneity and low defect density ensures good charge transport properties and low leakage current.

(vi) Contacts that produce no defects, impurities or barriers to the charge collection process and which can be used effectively to apply a uniform electric field across the device. Related to this is the requirement for the detector to be free of polarization effects, i.e., any processes (e.g., space-charge buildup within the device) that over time change the magnitude or uniformity of the electric field within the device and thus produce temporal changes in the detector operation.

(vii) Surfaces with sufficiently high electrical resistivity, noise of which due to surface conduction is low. The surfaces should be stable over time to prevent increase in the surface leakage current and to prevent problems of incomplete charge collection and buildup of surface charges.

Among other materials meeting the above requirements, CdTe and CZT have become the forefront in applications covering X-ray and γ-ray spectrometers as they reliably produce high resolution spectra over a wide energy range [7].

1 General properties of CdTe and CZT

1.1 Basic properties

Both CdTe and ZnTe have the cubic zincblende structure [8]. This can be described as two interpenetrating face-centered cubic sub-lattices shifted from each other by a quarter of a unit cell diagonal. The Cd or Zn cation occupy one sublattice, the Te anions the other. CZT can ideally be regarded as a CdTe crystal with Zn atoms randomly substituted for a fraction x of the Cd atoms, $\mathrm{Cd}_{1-x}\mathrm{Zn}_x\mathrm{Te}$ [6]. As the lattice constants of CdTe and ZnTe are different, the substitution of Zn atoms for Cd is accompanied by a change in the average unit cell dimension. It is usually assumed that the resulting lattice constant, $a(x)$, is a linear interpolation between the two constituents. This so called Vegard's law can be written in the following way:

$$a(x) = a^{(\mathrm{CdTe})}(1-x) + a^{(\mathrm{ZnTe})}x, \tag{0.1.1}$$

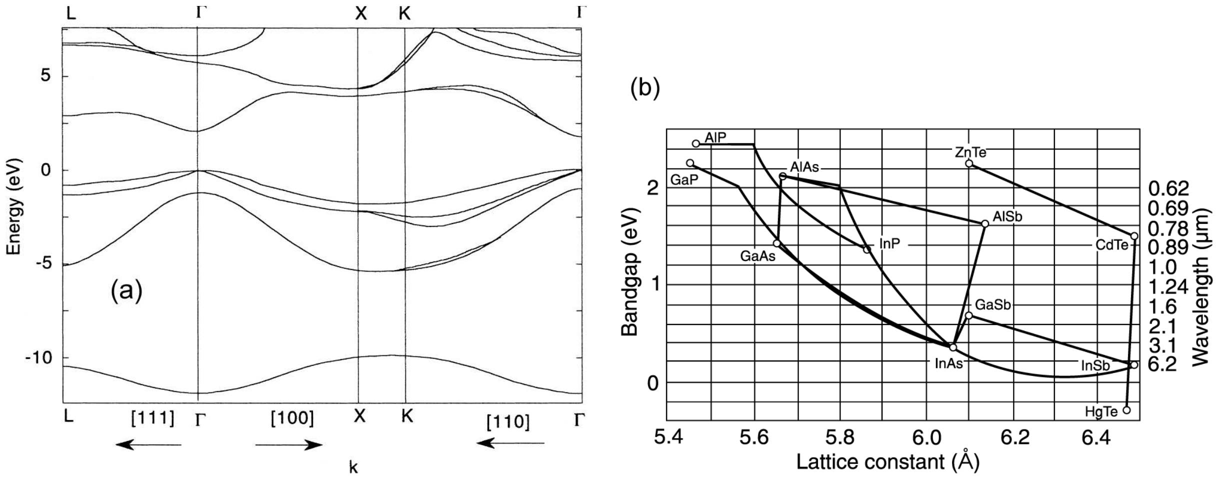

Figure 0.1.1: (a) Band structure of CdTe [6], **k** is the wave vector. (b) Comparison of bandgaps and lattice constants of a variety of II–VI and III–V compounds [11].

where $a^{(\mathrm{CdTe})} = 0.648$ nm and $a^{(\mathrm{ZnTe})} = 0.610$ nm are, respectively, the lattice constants of CdTe and ZnTe at room temperature [9]. CdTe and ZnTe are direct-bandgap semiconductors with bandgaps at room temperature of approximately 1.5 eV and 2.2 eV, respectively. Thanks to direct bandgap these compounds are attractive for optical devices. The band structure of CdTe is shown in Fig. 0.1.1a. CdTe has relatively low effective mass for electrons (approximately $0.11m_0$, m_0 being the electron rest mass), which gives it good transport properties. For holes one must remember that there are different effective masses for the separate valence bands (light holes, heavy holes, split-off band).

The band structure of CZT is more difficult as it is a ternary semiconductor. Simple approximation proposed by the virtual crystal approximation assumes that the crystal potential can be considered a linear interpolation between the two constituents (CdTe and ZnTe), implying, e.g., that the bandgap should vary linearly with x. In practice, the measured dependence of the bandgap, $E_g(x)$, as a function of composition x is always found to have some curvature. It is often expressed by equation [10]

$$E_g(x) = (1-x)E_g^{(\mathrm{CdTe})} + xE_g^{(\mathrm{ZnTe})} - bx(1-x) \qquad (0.1.2)$$

with the bowing parameter, b, which is attributed to short-range disorder. However, the published values of b vary substantially. The latter equation may be the basis for tuning the bandgap energy of CZT by controlling the fraction of Zn atoms, a bandgap engineering, analogously to the practice in technology of III–V compounds. Naturally, the bandgap is the function of temperature and external pressure. More details will be discussed in Part II of this thesis.

As mentioned in the Preface, Zn atoms are not the only ones which are added to CdTe to produce a ternary alloy. Technologies have been developed to produce CMT ($\mathrm{Hg}_{1-x}\mathrm{Cd}_x\mathrm{Te}$), a compound the bandgap of which can be tuned from 0.0 eV (HgTe) to 1.5 eV (CdTe) by controlling the amount of Cd to Hg, see Fig. 0.1.1b. Equations analogous to Eqs. (0.1.1) and (0.1.2) exist for CMT as well, which are the basis of proper lattice constant matching of CMT and CZT in the technology of IR radiation detectors based on these materials [11].

CdTe has a density of 5.85 g/cm^3 and congruent melting point of 1092 °C. High electro-optical coefficient of 6.8×10^{-12} m/V enabled the use of CdTe as an electro-optical modulator and makes it possible to investigate the internal electric field in a detector by the Pockels effect. Electron mobility of ~ 1000 cm/Vs and high intrinsic $\mu\tau$ are two prerequisites for efficient radiation detection (see requirement (iv) in the Preface). These properties are later discussed in Chapter 3 and are the key topics of Part I.

1.2 Growth methods

Based on the detail review presented in [6, 7], a short overview of growth methods used for the growth of CdTe and CZT is given. Among the others, the most important are: the Bridgman method (BM), vertical gradient freeze method (VGF), travelling heater method (THM), physical vapor growth, and vapor phase epitaxy. Numerous variations of each method have been reported. For successful use of grown crystal as a material for radiation detectors, strict electrical and structural quality requirements must be met.

Bridgman method. The basic Bridgman method involves the movement of a crucible containing the melt through a furnace designed to provide a suitable temperature profile. The furnace may be either vertical or horizontal. The crucible may be transported through the heater, or the crucible being stationary with a moving heater, or alternatively, both stationary and the temperature profile altered by a programmed temperature controller (VGF). The method is further differentiated according to growth pressure into the high-pressure Bridgman method (HPB) and low-pressure Bridgman method (LPB).

In the HPB method an over-pressure of 10–150 atm of an inert gas, typically Ar, is maintained over the melt to suppress the loss of volatile components; however, the losses of Cd are usually not eliminated, which causes the melt to become enriched with Te during the growth. This results in the presence of Te inclusions and precipitates in the crystal.

The LPB method has been successfully employed to produce spectrometer quality CZT without the use of a high gas overpressure. Both vertical and horizontal designs can be employed; however, it is believed that the horizontal one offers potential advantages over the vertical one due to the perpendicular orientation of the gravitational field relative to the growth axis [6].

Vertical gradient freeze method. Though it is a variation of the Bridgman method, a separate paragraph is devoted to VGF since this technique was used in the growth laboratory of the Institute of Physics of Charles University for the growth of some samples investigated in this thesis. Unlikely to classical vertical BM, both the crucible and heater are stationary while the necessary temperature gradient is ensured by electronically-controlled heating coils.

Travelling heater method. This is currently probably the most popular method for commercial growth of CdTe and CZT crystals. This method has evolved from the zone refining technique originally developed for purifying crystals. Starting polycrystalline material is placed into an evacuated chamber or an inert atmosphere. A moving RF heating coil is used to melt a narrow region of the crystal. Those impurities the segregation coefficient of which is lees than unity are concentrated in the melt. While the molten zone is slowly moved along the crystal, single-crystalline material is usually solidified and the impurities are transported to the one end of the crystal. This part is consequently cut off, leaving the purified grown crystal.

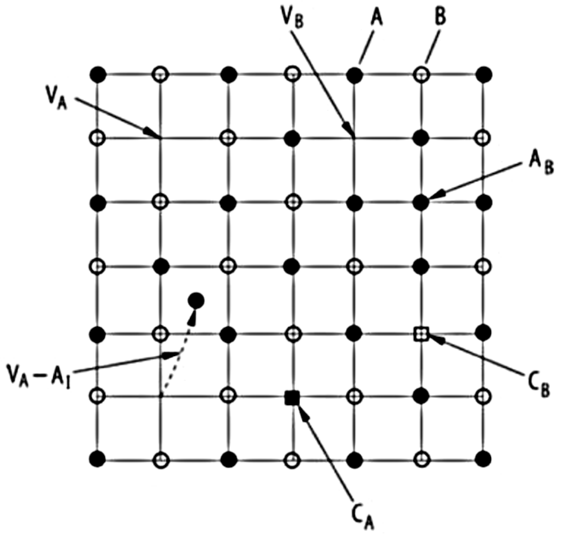

Figure 0.1.2: Native point defects in CdTe [12]. C_A and C_B are impurity atoms at places of atoms A and B; other notation is described in the text.

1.3 Defects

In an ideal crystal all atoms form perfectly periodical crystalline lattice, e.g., the zincblende structure in the case of CdTe. Unfortunately, this situation is theoretically possible only at $T = 0\,\mathrm{K}$. At non-zero temperatures, deviations from the ideal distribution of atoms occur and various defects are formed.

Point defects. In a binary compound AB several *native* defects exist (Fig. 0.1.2): vacancies V_A, V_B, interstitials A_I, B_I, antisite defects B_A, A_B, and their complexes, e.g., Frenkel defects V_A–A_I, V_B–B_I, complex of B_A–V_A, etc.

Thermodynamic calculations of defect equilibria established under specific external conditions (temperature, pressure of the gas phase of one component of AB compound) can be treated in a quasi-chemical formalism, based on the knowledge of the formation energies and structure of defects' energy levels in the bandgap. Various methods may be utilized in the investigation of both shallow and deep levels in the bandgap, including photoluminescence (PL), photo-induced current transient spectroscopy (PICTS), deep-level transient spectroscopy (DLTS), thermoelectric emission spectroscopy (TEES), Hall effect measurements, etc. However, identification of observed energy levels with particular defects does not have to be an easy task. Dominant donor-like native defects in Cd-rich CdTe crystals are singly- and doubly-ionized interstitials, $\mathrm{Cd}_\mathrm{I}^{+}$ and $\mathrm{Cd}_\mathrm{I}^{2+}$, and doubly-ionized antisites, $\mathrm{Te}_\mathrm{Cd}^{2+}$. The main acceptor-like native defects are singly- and doubly-ionized vacancies, $\mathrm{V}_\mathrm{Cd}^{-}$ and $\mathrm{V}_\mathrm{Cd}^{2-}$ [13].

Except for native defects, *extrinsic* point defects are of major importance for growth technologies and subsequent treatment of CdTe crystals and related compounds. Extrinsic defects are either undesirable impurities present in the crystal or dopants intentionally introduced into the material to modify its properties. It is desirable to reduce the concentration of impurities below the level of native point defects, i.e., under approximately 10^{15} cm^{-3} at room temperature. The most important dopants of CdTe are In and Cl. Both behave as shallow donors and together with $\mathrm{V}_\mathrm{Cd}^{2-}$ they create an acceptor-like complex defects, A-centers: $(\mathrm{In}_\mathrm{Cd}\text{–}\mathrm{V}_\mathrm{Cd})^{-}$ in the case of In, $(\mathrm{Cl}_\mathrm{Te}\text{–}\mathrm{V}_\mathrm{Cd})^{-}$ in the case of Cl.

The role of point defects is critical for the compensation of CdTe, a method for reaching of a high-resistive (semi-insulating) state with resistivity higher than $10^9\ \Omega\,\mathrm{cm}$) which is necessary for CdTe detectors to minimize dark current at room temperature. A way how to successfully accomplish this is to precisely compensate shallow charged defects while pinning the Fermi level on a deep level in the midgap. Details are to be found in literature, e.g., in [14].

Line defects. Crystallographic defect oriented along a particular line within the material is called *a dislocation*. Typically, dislocations are formed during the growth of the crystal to relax the stress induced within the material due to the solidification of the melt in a crucible, which sustains the melt in a fixed volume, unabling it to expand freely to an empty space. The presence of dislocations strongly influences material properties. Dislocations are formed randomly within the whole crystal grain; however, crystallographic structure of the material predestinates several preferred directions, which can be seen in micro-indentation experiments [15]. Two primary types of dislocations exist: *edge dislocations* and *screw dislocations*. *Mixed dislocations* are intermediate between these.

Dislocation density, the total length of dislocations in a unit volume of the material, can be revealed by measuring the edge pit density. In such an experiment, surface of the material is etched using a special etchant that leaves an observable pit in the place where the dislocation appears on a surface of the crystal. For CdTe and CZT, a Nakagawa etch, consisting of HF, H_2O_2, and water, is used. A typical observed dislocation density is of the order of 10^4 cm^{-2}.

Planar defects. The most common type of planar defects are *grain boundaries*, created in the crystal during the solidification of the melt when grains growing from different nucleation centers (of different lattice orientations) meet. The size and number of grain boundaries depend on growth conditions, purity of the material and crucible, roughness of crucible walls, vibrations, etc. CdTe crystals prepared by the Bridgman method are usually polycrystalline; however, the size of grains is large enough to make it possible to prepare monocrystalline pieces for the fabrication of radiation detectors.

A single grain can also contain planar defects of its own. A disruption of the long-range stacking sequence can produce *stacking faults* and *twin boundaries*. A change in the stacking sequence over a few atomic spacings produces a stacking fault whereas a change over many atomic spacings produces a twin region. A stacking fault is a one or two layer interruption in the stacking sequence of atomic planes. If a stacking fault does not correct itself immediately but continues over some number of atomic spacings, it produces a second stacking fault that is the twin of the first one. Adjacent atomic layers are mirrored across the twin boundary. Twin boundaries may also be found in CdTe crystals.

Planar defects are easily observable by visual inspection on roughly polished wafers (F600 abrasive, see Subsection 3.1.1 in Part I), in IR transmittance images, or by X-ray diffraction topography.

Bulk defects. Although the phase diagram of CdTe is sufficiently known nowadays [16], the complexity of the crystal growth process makes it very difficult to precisely follow the ideal crystallization conditions and maintain the stoichiometry in the whole crystal volume. As a result two different phases, solid and melt, with nonstoichiometry composition appear during the solidification and consequent cooling process, giving birth to second phase defects.

Inclusions are formed during the solidification of the melt due to thermal fluctuations on the crystallization interface, which leads to the capturing of melt droplets [17].

Depending on the excess component in a droplet, either star-shaped Cd-inclusions or triangular and hexagonal Te-inclusions may be formed. Because of their size of up to tens of micrometers and strong IR absorption, inclusions are easily investigated by means of IR microscopy.

Precipitates are formed during the cooling of the solidified crystal due to retrograde solubility of the excess component in the solid [17]. With its size of up to tens to hundreds of nanometers, they are much smaller than inclusions. Precipitates may be formed randomly within the whole volume of the crystal (homogeneous precipitation); however, precipitation takes place much easier on the crystal imperfections, e.g., along dislocations, twin or grain boundaries (heterogeneous precipitation).

Except for inclusions and precipitates, *voids* are small regions where there are no atoms, and can be thought of as clusters of vacancies.

2 Interactions of radiation with matter

To employ any material as a radiation detector, radiation must interact with the matter of the detector and efficiently lose its energy within the active volume. The knowledge of the mechanism of how the energy is deposited in the detector is very important for interpretation of measurements as well as for the construction of detectors. Generally, based on the type of interaction, ionizing radiation can be divided into three groups [18]:

(i) Charged particles: electrons (e^-), positrons (e^+), protons (p), deuterons (d), alphas (α), and heavy ions.

(ii) Photons: gammas (γ) and X-rays.

(iii) Neutrons (n).

For the purposes of this thesis, the first two groups are of interest.

A charged particle moving through the material interacts, primarily through Coulomb forces, with the negative electrons and the positive nuclei that constitute the atoms of that material. As a result of these interactions the particle loses energy continuously and finally stops after traversing a finite distance—the range, depending on the type and energy of the particle and on the material through which the particle moves.

Photons have no charge. They interact with matter in several ways, depending on the energy of the radiation and the material. Since there is a finite nonzero probability that photon may go through any thickness of any material without having an interaction, no finite range is defined for photons. Alternatively, a linear absorption coefficient (or, equivalently, an absorption depth) is defined, which relates to the distance the radiation must travel in the material for its intensity being reduced to $1/e = 0.368$ of the original value.

2.1 Charged-particle interactions

Among the others the two most important ways charged particles lose its energy when travelling through matter are (i) the Coulomb interactions with electrons and nuclei, (ii) the emission of electromagnetic radiation (bremsstrahlung).

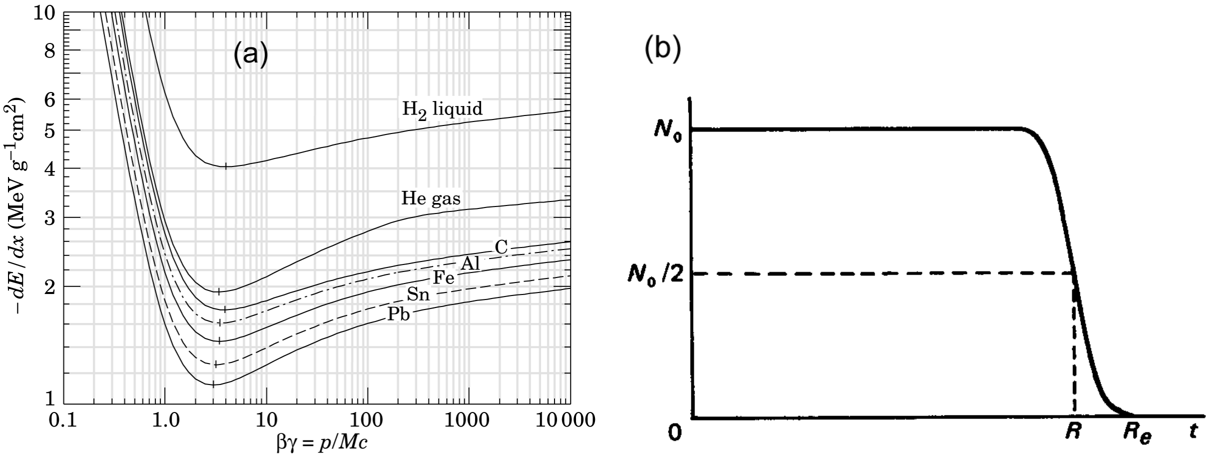

Figure 0.2.3: (a) Stopping power dE/dx as a function of particle energy for several materials [20]. Symbol definitions are explained in text. (b) Number of heavy charged particles transmitted through thickness t [18]; N_0 is the initial number of particles, R is the range.

Coulomb interactions. Because of approximately 10^4 times higher radius of an atom ($\sim 10^{-10}$ m) in comparison to the radius of a nucleus ($\sim 10^{-14}$ m), Coulomb interactions occur much more probable with atomic electrons than with nuclei [18].

Through the Coulomb interaction the moving free particle can either ionize or excite the atom with the electron of which it interacts. *Ionization* occurs when the electron obtains enough energy to leave the atom and become a free particle with kinetic energy equal to the energy transferred from the particle diminished by the ionization energy. The electron freed from the atom acts like any other moving charged particle; it may cause ionization of another atoms if its energy is high enough. It will interact with matter, lose its kinetic energy (mostly via ionization and bremsstrahlung) and finally stop.

Excitation takes place when the electron acquires enough energy to move to an empty state in another orbit of higher energy, thus producing an excited atom. Shortly after the interaction, electron moves to a lower empty energy state, accompanied by an emission of an X-ray with energy equal to the energy difference between the levels.

During its passage through material particle interacts with a huge number of electrons simultaneously. To characterize the energy losses, an average energy loss per unit distance travelled, so called stopping power, dE/dx (MeV/m), is calculated. Exact formulae for dE/dx differ depending on the type of particle and are quite complicated [18]. Nevertheless, dense materials absorb charged particles better than lighter ones. Typical dependence of dE/dx on the particle kinetic energy, T, is shown in Fig. 0.2.3a. It is worth noting that the ionization losses are minimum no matter of the density of the medium for that particle kinetic energy for which $\beta\gamma = 3$–4 [19]; γ being the relativistic factor, i.e., $\gamma = (T + Mc^2)/Mc^2$, and $\beta = v/c$, where v is the particle velocity and c is the speed of light in vacuum.

As particle loses the energy during traversing through the medium, its speed decreases until the particle completely stops. It has been experienced that for α-particles of energy less than 20 MeV, the stopping power always increases (corresponding points are on the left of curve minimum in Fig. 0.2.3a). This results in a typical curve that expresses the number of heavy-charged particles transmitted through the material, a Bragg curve, see Fig. 0.2.3b. To express the thickness of material that completely stops a particle of certain kinetic energy, the range, R, is defined. Several semiempirical formulae exist, e.g., for α-particles in air at normal temperature and pressure and 4 MeV$\leq T \leq$ 15 MeV, the following equation is valid [18]:

$$R\ (\text{mm}) = (0.05T + 2.85)T^{3/2}, \quad T \text{ in MeV}. \tag{0.2.3}$$

If the range is known for one material, it can be determined for any other by applying the Bragg-Kleeman rule [18]:

$$\frac{R_1}{R_2} = \frac{\rho_2}{\rho_1}\sqrt{\frac{A_1}{A_2}}, \tag{0.2.4}$$

where ρ_i and A_i are the density and atomic weight, respectively, of material i. Since $\sqrt{A_{\text{air}}} = 3.84$ and $\rho_{\text{air}} = 1.29$ kg/m^3 for air at normal temperature and pressure, one can immediately evaluate the range of 5.5 MeV α-particles of ^{241}Am in air, Au, and CdTe. Using Eqs. (0.2.3) and (0.2.4), $\sqrt{A_{\text{Au}}} = \sqrt{197}$ and $\rho_{\text{Au}} = 19.32 \times 10^3$ kg/m^3, and $\sqrt{A_{\text{CdTe}}} = \sqrt{240}$ and $\rho_{\text{CdTe}} = 5.85 \times 10^3$ kg/m^3, one obtains:

$$R_{\text{air}} = 40 \text{ mm} \quad \text{in air}, \tag{0.2.5}$$
$$R_{\text{Au}} = 10\ \mu\text{m} \quad \text{in Au}, \tag{0.2.6}$$
$$R_{\text{CdTe}} = 36\ \mu\text{m} \quad \text{in CdTe}. \tag{0.2.7}$$

Unlikely to heavy charged particles, the number of electrons transmitted through the material decreases gradually without any flat part typical to Bragg curve. Electrons thus dissipate the energy along their whole path in the matter.

Bremsstrahlung. Each free charged particle that (de)accelerates loses part of its kinetic energy by emitting electromagnetic radiation, so called *bremsstrahlung*. Bremsstrahlung consists of photons with energies from zero up to the kinetic energy of the particle. The intensity of emitted radiation, I_{br}, is proportional to the atomic number of the medium, Z, and the particle mass, M, according to the formula $I_{br} \sim (z^2Z^2)/M^2$ [18], if z is the number of elementary charges the particle consist of (particle charge). It is obvious that more bremsstrahlung is emitted in a medium with higher Z by a lighter particle. It is usually important for electrons only.

2.2 Interactions of photons

Photons are electromagnetic radiation covering the range from radio waves to γ-rays. For the purposes of this text the X-rays and γ-rays are of importance. The term X-rays is applied generally to photons with energy from 100 eV to 100 keV; gammas are the photons with energy greater than 100 keV. X-rays are generally produced by atomic transitions such as excitation and ionization; γ-rays are emitted in nuclear transitions. Photons are also produced as bremsstrahlung, by accelerating or decelerating charged particles. X- and γ-rays emitted by atoms and nuclei are monoenergetic, bremsstrahlung has a continuous energy spectrum. The three most important interactions of photons with matter are discussed separately as follows.

Photoelectric effect. The photoelectric effect is an interaction between a photon and a bound atomic electron. As a result, the photon disappears and one of the atomic electrons is ejected as a free electron. The kinetic energy of that electron is then $T = E - B_e$,

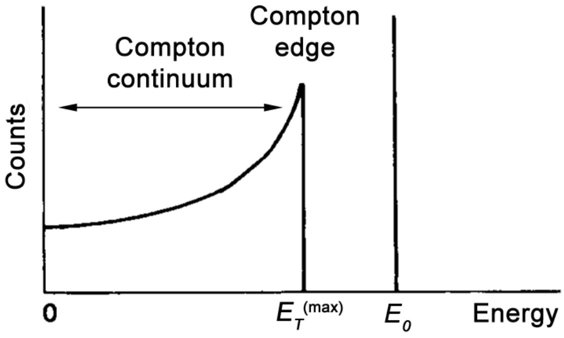

Figure 0.2.4: Typical shape of a pulse height spectrum of a monoenergetic radiation source (energy E_0) recorded by a detector in the absence of statistical effects (perfect energy resolution). According to [18].

where E is the energy of the photon and B_e is the binding energy of the electron. The probability of this interaction, evaluated through the photoelectric cross-section, σ_{ph}, strongly depends on the atomic number of the medium and the energy of incident photons:

$$\sigma_{\text{ph}} \sim \frac{Z^n}{E^m}, \qquad \text{where } n = 4\text{–}5,\ m = 3\text{–}5. \tag{0.2.8}$$

It is thus important for materials of higher Z and less energetic photons. The photoelectric cross-section plotted as a function of the photon energy (see Fig. 0.2.5 later) exhibits the characteristic absorption edges (a saw-tooth structure) at energies that coincide with binding energies of electron (sub)shells.

Compton effect. The Compton effect is a collision between a photon and a free electron. Although, under normal circumstances, all the electrons in a medium are bound, because of much greater energy of the photon in comparison to their binding energy (keV vs. eV), they may be considered free. After a Compton scattering, the direction and energy of the photon are changed as part of photon energy is transferred to the electron. These quantities are functions of the scattering angle, θ, and may be calculated on the basis of the energy and momentum conservation laws, giving [19]

$$E' = \frac{E}{1 + (E/m_0c^2)(1 - \cos\theta)}, \tag{0.2.9}$$

where E and E' are photon energies before and after scattering, m_0 is the electron rest mass, and c is the speed of light in vacuum. The scattered photon has the minimum energy when the backscattering takes place, $\theta = \pi$. This energy is non-zero and corresponds to the maximum energy, $E_T^{(\max)}$, being transferred to the electron. From Eq. (0.2.9) one obtains

$$E_T^{(\max)} = E - E'(\theta = \pi) = \frac{2E^2}{2E + m_0c^2}. \tag{0.2.10}$$

The maximum energy of the scattered photon is obtained for $\theta = 0$, which essentially means that no collision did take place. The energy given to the electron is dissipated in the material within a distance equal to the range of electrons. The scattered photon may escape, resulting in no more energy being deposited in the detector. Thus, only a fraction of the original energy of the photon is recorded by the detector in such a case. After the recording of a plenty of events (to have good statistics), a typical shape of a pulse height spectrum is formed with the so called Compton continuum and a sharp cut-off, the Compton edge, at the energy of $E_T^{(\max)}$, see Fig. 0.2.4. This is often the case of thin detectors. In thick detectors multiple subsequent Compton scattering events may take place until all of the original photon energy is deposited in the medium.

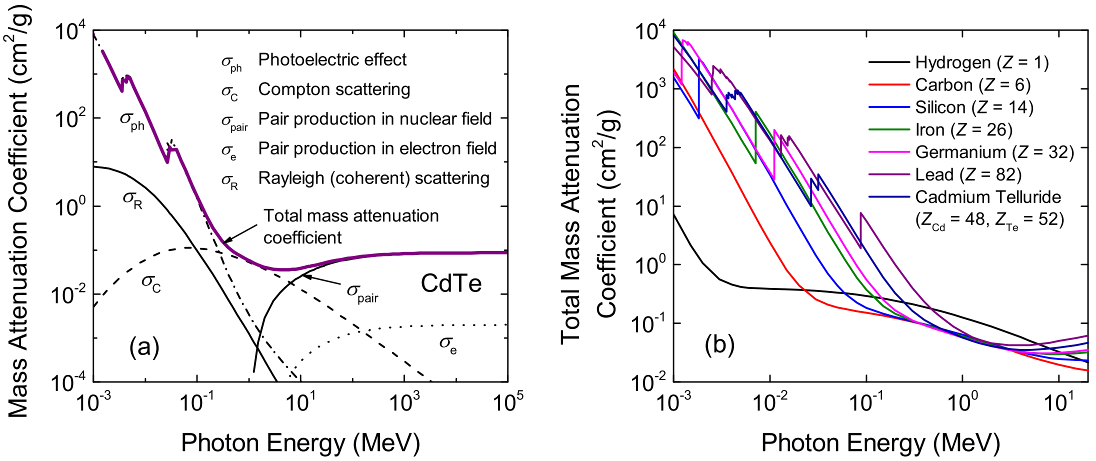

Figure 0.2.5: (a) Particular contributions to the total mass attenuation coefficient (μ_{tot}/ρ) of CdTe [21]. (b) Total mass attenuation coefficients of several materials [22].

The probability that Compton scattering will occur, the Compton cross-section, σ_{C}, is related to the atomic number of the medium and the energy of incident photons via the equation [18]:

$$\sigma_{\text{C}} \sim Zf(E), \tag{0.2.11}$$

where $f(E)$ is a function of E.

Pair production. Pair production is an interaction between a photon and a nucleus. As a result of the interaction, the photon disappears and an electron–positron pair is created. Although the nucleus does not undergo any change sequent upon this interaction, its presence is necessary for pair production to occur. The photon minimum energy necessary for the interaction to take place is equal to the rest mass of electron and positron, i.e., 2×511 keV= 1.022 MeV. Shortly after the creation of a positron, the positron annihilates, producing two annihilation gammas.

The probability for pair production to occur, the pair production cross-section, σ_{pair}, is a complicated function of E and Z, but may be written in a simplified form [18]:

$$\sigma_{\text{pair}} \sim Z^2 f(E, Z), \tag{0.2.12}$$

where $f(E, Z)$ is a function that changes slightly with Z and increases with E. Pair production can take place in the field of an electron as well, however, the probability of such an interaction is much smaller and the threshold energy twice as much as in the field of a nucleus.

Total (mass) attenuation coefficient. To express the total probability for interaction of a photon with matter, the total attenuation coefficient, μ_{tot}, is defined. It equals to the sum of all probabilities of particular photon interactions; especially, limiting further advance to the three most important interactions discussed above, one can write:

$$\mu_{\text{tot}} = \sigma_{\text{ph}} + \sigma_{\text{C}} + \sigma_{\text{pair}} \qquad (\text{cm}^{-1}). \tag{0.2.13}$$

The value of μ_{tot} is sometimes divided by the material density, ρ, to obtain the total mass attenuation coefficient, μ_{tot}/ρ, expressed in cm^2/g. For a known material the criterion for which interaction prevails is the energy of incident photons. As an example, it can be found in Fig. 0.2.5a that in CdTe it is the photoeffect for low energy photons, for energies between 0.2–5 MeV it is the Compton scattering what prevails, until, finally, above 5 MeV the pair production dominates. The energy dependence of mass attenuation coefficients for several materials including CdTe is shown in Fig. 0.2.5b.

The intensity of radiation, $I(t)$, corresponding to the number of photons that will penetrate the thickness t without having an interaction is easily calculated using μ_{tot} defined by Eq. (0.2.13), since the well-known exponential attenuation law holds:

$$I(t) = I(0)e^{-\mu_{\mathrm{tot}} t} = I(0)e^{-(\mu_{\mathrm{tot}}/\rho)w}. \tag{0.2.14}$$

Here, $I(0)$ is the initial intensity striking the target and $w = t\rho$ is the mass thickness. The mean free path, λ_{mean}, the average distance between two successive interactions, is related to the attenuation coefficient via the relation $\lambda_{\mathrm{mean}} = 1/\mu_{\mathrm{tot}}$.

3 Radiation detectors based on CdTe

In previous text general requirements for any material being utilized for detection of high energy radiation have been stated. Properties of several semiconductor materials are summarized in Table 0.3.1. Among other materials meeting these requirements, CdTe based compounds have proven in recent decades to be extra suited for application in medicine, astronomy, nuclear sciences, homeland security, military, process monitoring, remote sensing, and many other civil, industrial, and scientific applications. It is its high atomic number ($Z = 48$ for Cd, $Z = 52$ for Te) what ensures CdTe one to three orders-of-magnitude higher photoelectric absorption as compared to silicon ($Z = 14$) or germanium ($Z = 32$).[1] Direct conversion of incident radiation to measurable electric signal prefers CdTe (and other semiconductor materials) over scintillators since it offers better energy resolution.[2] Moreover, room temperature bandgap of approx. 1.5 eV enables the detectors fabricated from CdTe to operate at room temperature without cooling, which makes it possible to develop compact and portable detectors and detector-based solutions.

Mechanisms of interactions of high energy radiation/particles with the detector matter were discussed in Chapter 2. For a CdTe detector intended mainly for detection of X-rays or γ-radiation, the most important interactions are the photoelectric effect, Compton scattering, and pair productions; α-particles interact via Coulomb interaction. Through any of these interactions, the last step of energy loss mechanism is multiple ionization of the matter, which creates numbers of electron–hole pairs. These carriers are spread along the path of the particle though the matter, starting at the place of incidence and ending where the particle completely stops. The "interaction depth" (range, mean free path or whatever quantity related to the corresponding mechanism) depends on the interaction cross-section, which is, e.g., for α-particles so high as to create a localized "charge cloud" of typical dimensions of several micrometers. Dynamics of this cloud under external bias applied on the detector is highly important as it is affected by the quality of detector material and it determines detector efficiency. A well-known parameter indicating the

---

[1] From Eq. 0.2.8 the photoelectric cross-section is proportional to Z^n, $n = 4$–5, which yields $(50/14)^n = 160$–600 for silicon. Analogously for germanium.

[2] The full width at half maximum (FWHM) of a gaussian photopeak (and thus the resolution $\sim$FWHM) is proportional to $1/N$, where N is the number of "carriers" generated per 1 keV of incident radiation [18]. For semiconductors $N\sim 200$–400 electrons/keV, while for scintillators $N\sim 5$–50 photos/keV.

Table 0.3.1: Properties of semiconductor materials at room temperature [7].

Material	Ge	Si	GaAs	CdTe	CdZnTe[†]	Diamond
Atomic number	32	14	31, 33	48, 52	48, 30, 52	6
Density (g/cm^3)	5.33	2.33	5.32	6.2	≈ 6	3.51
Bandgap (eV)	0.67	1.12	1.43	1.44	1.5–2.2	5.4
Melting point (°C)	958	1412	1238	1092	1092–1295	4027
Pair production energy ϵ (eV)	2.96	3.62	4.2	4.43	4.43–5.0	13.25
Resistivity (Ω cm)	50	$< 10^4$	10^7	10^9	10^{11}	-
μ_e (cm^2/Vs)	3900	1400	8000	1100	1350	2000
μ_h (cm^2/Vs)	1900	480	400	100	120	1600
$\mu\tau_e$ (cm^2/V)	> 1	> 1	8×10^{-5}	3.3×10^{-3}	1×10^{-3}	2×10^{-5}
$\mu\tau_h$ (cm^2/V)	> 1	≈ 1	4×10^{-6}	2×10^{-4}	6×10^{-6}	$< 1.6 \times 10^{-5}$

[†] Properties depend upon the zinc content.

material's ability to perform well for spectrometer applications is the mobility–lifetime product, $\mu\tau$. While for the case of electrons in CdTe and CZT values of $\mu\tau_e \gtrsim 10^{-3}$ cm^2/V are typical, for the case of holes these values are much lower, $\mu\tau_h \sim 1$–10×10^{-5} cm^2/V. Incomplete hole collection then results in broadening of the photopeak to the low energy side and thereby decrease of the resolution of the spectrometer. Nowadays, detectors with resolution down to 1% at 662 keV are available.

Except for advantages offered by CdTe and CZT, there are several problems which limit the efficiency of detectors and which therefore should be taken into account. These are:

(i) Local distortions of the electric field within the detector bulk that could lead to space-charge buildup (polarization) and degradation of charge collection efficiency.

(ii) Grain boundaries seriously limiting efficiency of charge collection; therefore the most important property to improve detector performance is to increase the size of single crystals within the grown ingots without creating new trapping sites in single-crystal volumes [6].

(iii) Non-uniformity, which lowers the number of grown crystals that can be used for fabrication of large-area (pixelated) detectors. It is a known issue especially for CZT. Regions of different charge collection efficiency exist in such crystals, which either differentiates the response of individual pixels or causes anomalous shape of pulse height spectrum if collection is performed across non-uniform regions together.

(iv) Deep levels, which are—on the one hand—desirable to pin the Fermi level in the midgap, may act as recombination or trapping centers if their concentration is too high, consequently decreasing the lifetime of electrons and holes. If the deep-level concentration is too low, the resistivity is low and dark current too high, which lowers signal-to-noise ratio.

(v) Second phase defects larger than several micrometers that act as trapping centers for electrons and decrease the charge collection efficiency. This is very important for pixellated detectors, where Te-inclusions lower the response of pixels of higher concentration of second phase defects [23].

(vi) Similar to grain boundaries, dislocations that can affect charge collection as they accumulate high local concentrations of impurities that trap charge carriers in a manner similar to point defects, but at much higher rates due to the relatively high density of trapping centers [24].

Dislocation-related defects and Te-inclusions trap smaller fractions of the charge from the electron cloud, but collectively and over long drift distances, they cause fluctuations in the collected charge, and consequently, in the device response [24]. These problems pose a challenge for further research.

4 Aim of this thesis

In previous chapters the state-of-the-art in basic research of CdTe and CZT and related compounds has been reviewed as well as the advantages and disadvantages of utilizing these materials as room temperature radiation detectors. Important properties, technology, and mechanisms of particle interactions with detector matter have been summarized, the purpose of which was to provide in one place the basics that are necessary for further advancement.

It has already been stated in the Preface that for efficient operation the application of external voltage on detector contacts should result in a uniform (homogeneous) electric field across the device. Thus the knowledge of the internal electric field within the biased detector is of highest importance. By now, two different methods of measuring of the electric field exist: measurements utilizing the Pockels effect and the time-of-flight measurements. Transient-current technique (TCT) is one of the second kind. Though the Pockels effect measurement is only marginally mentioned in this thesis, the TCT is the main subject to detail analysis in Part I. After a TCT setup had been introduced to the laboratory of the Institute of Physics of Charles University in Prague (IoP CU) and few initial experiments had been performed, it was found that the theoretical background of the method as published in the literature by then was very simple and could not satisfy the demands. Therefore, extensive theoretical work has been done to fill these voids in knowledge by providing methods that can be generally applied on any data obtained from TCT measurements, but still limiting the analysis to a simple assumption of a constant space-charge density within the detector. These efforts led to the development of two iterative methods—the self-consistent procedure and direct-minimization procedure, the details of which are to be found in Part I. These methods were thoroughly tested and since they have proven to be very efficient, both the basic theory and applications have been published [25, 26, 27].

In Part II of this thesis high-temperature measurements of the absorption edge of CdTe are reported, from which the temperature dependence of the bandgap energy is deduced. The bandgap energy is one of major parameters characterizing any semiconductor material. Temperature dependence of the bandgap of CdTe was measured many times in the past utilizing both optical and transport measurements. Although there are no problems limiting these measurements at low temperatures, high-temperature measurements of the bandgap are much more complicated because of CdTe being a binary compound of Te and a volatile Cd. With the help of the phase diagram, these measurements must be performed under those thermodynamic conditions that prevent the decomposition of CdTe at high temperatures. Up to now there are several published results of high-temperature measurements carried out on CdTe, from those performed as early as in 1950s to those reported recently. If so, problems with the CdTe decomposition are treated differently by different authors. Results of these investigations are summarized and compared in Part II of the thesis. But above all, a unique setup capable of measuring of the high-temperature absorption edge of CdTe up to 1300 K which was built at IoP CU is described in detail therein together with a thorough study on various models being used for calculations of the temperature dependence of the absorption coefficient from measured transmittance data, terms of their use, and differences in obtained results. New procedures have been proposed for these calculations that, taking the expected theoretical temperature dependence into account, perform this task self-consistently.

The original outcomes of this work are the design and realization of two experimental arrangements for measuring (i) of the internal electric field and (ii) of the high-temperature absorption edge of CdTe and CZT samples in laboratories of IoP CU. Hand in hand with these tasks, methods for processing of measured data have been developed, tested, and demonstrated. This is what distinguishes this work from common experimental theses since in this thesis the development and introduction of new methods was emphasized rather than extensive research on a plenty of samples utilizing existing techniques. Both setups (i) and (ii) have been successfully implemented among the common characterization techniques and are prepared for further research at IoP CU.

Part I

Measurements of the internal electric field

1. Introduction

It has been known since early 1970s that the performance of radiation detectors strongly depends on the internal electric field within the detector [28]. For efficient operation (see requirement (vi) in the Preface), uniform electric field is of great demand. If it is degraded, regions with little or zero charge-collection could appear, which limits the detector efficiency [29]. The lower the electric field, the fewer photo-generated carriers are collected as they are subject to trapping. Moreover, the formation of space charge on traps in the volume of the detector entails the screening of applied bias and could give rise to an "inactive" region with zero electric field under the contact, limiting the charge collection as well.

Techniques have been developed for measuring of the internal electric fields to better understand the process of charge collection and polarization phenomena in radiation detectors. Both the linear electro-optical effect (the Pockels effect [30, 31, 32]) and the time-of-flight measurement (the transient-current technique—TCT [25, 33, 34]) were employed successfully to determine the profile of the electric field in CdTe and CZT detectors both in the dark and under high-flux irradiation. Moreover, the time-evolution of the electric field after biasing the device was also reported [35]. Recently, other researchers incorporated additional laser illumination in their investigations of polarized detectors so as to modify the space charge within them [36]. Further, in addition to the need for high crystalline quality of the detector bulk material, the contacts can also crucially affect the device performance. Consequently, to assure the best performance, the choice of material for contacts and sometimes method of deposition must be taken into account.

Because of high electro-optical coefficient of CdTe, direct mapping of the internal electric field based on the measuring of the Pockels effect[1] has been adopted by many laboratories all over the world. Though it is a powerful technique, it requires complex instrumentation and samples must undergo a special treatment to prepare an optical quality surface. On the contrary, the transient-current technique, a purely "electrical" method based on the time-of-flight measurement of drifting charge carriers, allows the characterization of the spatial distribution of the electric field without any special sample preparation process while the necessary instrumentation is reduced to a current-sensitive preamplifier and a digital storage oscilloscope.

In this part of the thesis a detailed description of the TCT experimental setup operating in the laboratory of the IoP CU is to be found as well as the complex theory of the processing of experimental data. New iterative procedures that have been developed to enable correct calculations of mobility–lifetime product and electric field in polarized detectors are introduced, deeply analyzed, and their applicability is demonstrated on several CdTe and CZT samples.

---

[1] Measurement of the light intensity passing through the sample placed between two crossed polarizers. As the registered intensity is related to the electric-field induced change of the refractive index of the sample, the internal field can be reconstructed.

2. Theory of transient-current technique

One of the original results of this thesis is the general theory covering the techniques for the calculation of the distribution of the internal electric field within planar radiation detectors, based on the simultaneous processing of electrical (analysis of current waveforms) and spectral measurements (measurements of charge-collection efficiency). The most important results have already been published [25, 26, 27]. In the following sections a thorough derivation of equations that are important for further analysis being the subject of Chapter 4 is given.

Recent measurements [25, 31, 34, 37] approved that in many situations a constant space-charge density, ρ, may be anticipated in both CdTe and CZT radiation detectors:

$$\rho = \text{const.}, \tag{I.2.1}$$

thus yielding a linear profile of the electric field. However, whereas some authors report the positive space charge [30, 31, 34], the others report the negative one [28, 38, 39], reflecting the different quality of detector material and/or prepared contacts. At this place, the assumption of the constant space-charge density is adopted and derivation of general equations for the calculation of the profile of the electric field using the transient-current technique (TCT), and for the evaluation of $\mu\tau$ from measurements of the charge-collection efficiency (CCE) is given, covering both cases of positive and negative space charges.

The whole theory deduced in this chapter is based on these assumptions:

(i) The detector is planar with the thickness L. Carrier movement is treated in one dimension with the x-axis set in such a way that $x = 0$ marks the cathode and $x = L$ represents the anode of the sample (see Fig. I.2.1). Space-charge density within the depletion layer is homogeneous.

(ii) Free carriers are created closely below the irradiated contact as it happens with α- or above bandgap energy photon irradiation, which allows one to take the movement of only one type of carriers into account.

(iii) To collect electrons the detector is irradiated from the cathode side; for the collection of holes the anode side of the sample is irradiated.

(iv) The applied bias $U > 0$ is considered overall in the thesis.

2.1 Transient-current technique

The theory deduced herein extends the approach applied in [33] by the involvement of the loss of free carriers due to trapping in deep defects. Detrapping is neglected and constant carrier mobility, μ, is assumed. The strength of the electric field, $E(x)$, at the distance x from the cathode of the sample, no matter of the polarity of space charge (i.e., valid for both positive and negative space charges), can be expressed in the form

$$E(x) = \max\left\{0; E_0 - ax\right\}, \tag{I.2.2}$$

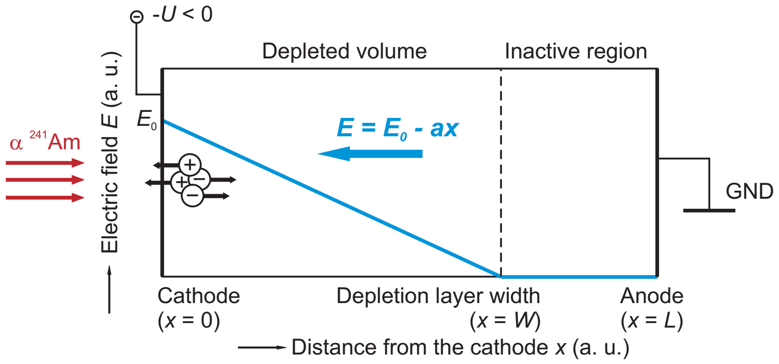

Figure I.2.1: Scheme of the profile of the electric field in a detector with positive accumulated charge under α-particle irradiation from the cathode side.

where a is the slope of the electric field linear dependence, $\max\{\,;\,\}$ is a function returning the greater of its arguments, and the constant term E_0 is expressed as follows, taking the boundary conditions for the Poisson's equation into consideration:

$$E_0 = \begin{cases} \frac{U}{\mathcal{L}} + \frac{1}{2}a\mathcal{L} & \text{for } a \geq 0, \\ \frac{U}{\mathcal{L}} + \frac{1}{2}a(2L - \mathcal{L}) & \text{for } a < 0. \end{cases} \tag{I.2.3}$$

Here, the symbol $\mathcal{L} = \min\{L; W\}$ is the depletion width of the detector volume; $\mathcal{L}$ is calculated as the less from two quantities: (i) the detector thickness, L, and (ii) the "theoretical" depletion width, W, corresponding to the field slope a, which is given by the equation [40]

$$W = \sqrt{2U/|a|}, \tag{I.2.4}$$

resulting again from the boundary conditions for the solution of the Poisson's equation with Eq. (I.2.1). In Eqs. (I.2.3) and (I.2.4), U denotes the applied bias. For better understanding of defined quantities, Fig. I.2.1 might be helpful. Two situations may occur:

(i) $W < L$: The electric field is completely screened near one electrode, where an inactive region with zero electric field appears, $\mathcal{L} = W$.

(ii) $W \geq L$: The electric field is non-zero within the entire volume of the detector, an inactive region does not exist, $\mathcal{L} = L$.

The definition of the strength of the electric field $E(x)$ given by Eq. (I.2.2) ensures that $E(x)$ is non-negative regardless of the polarity of applied bias, space-charge density within the detector volume, and the type of collected carries (electrons/holes). In addition, Eq. (I.2.2) involves the case of zero electric field in a certain part of the detector bulk (implying that the bulk is not fully depleted).[2]

When irradiating the sample from the cathode side (collection of electrons), E_0 is important since it directly represents the electric field under that contact. Denoting by E_C the electric field under the cathode, $E_C = E(0)$, it can be expressed in the form:

$$E_C = \begin{cases} 0 & \text{if } a \leq 0 \text{ and } W \leq L, \\ E_0 & \text{otherwise.} \end{cases} \tag{I.2.5}$$

---

[2] The term "dead layer" is sometimes used for the region in which $E(x) = 0$.

When collecting holes (sample irradiated from the anode side), the electric field under the anode, E_A, is calculated using

$$E_A = \begin{cases} 0 & \text{if } a \geq 0 \text{ and } W \leq L, \\ E_L & \text{otherwise,} \end{cases} \tag{I.2.6}$$

where

$$E_L = \begin{cases} \frac{U}{\mathcal{L}} - \frac{1}{2}a(2L - \mathcal{L}) & \text{for } a \geq 0, \\ \frac{U}{\mathcal{L}} - \frac{1}{2}a\mathcal{L} & \text{for } a < 0. \end{cases} \tag{I.2.7}$$

The sign convention for a is such that the density of the accumulated charge (space-charge density), ρ,

$$\rho = \varepsilon_0 \varepsilon_r a, \tag{I.2.8}$$

calculated from the electronic signal is of the same sign as a, i.e., $\rho > 0$ for the positive space charge, and $\rho < 0$ for the negative one; see Table I.2.1 and the discussion around. In the latter equation, ε_0, $\varepsilon_r = 10.3$, and e, respectively, are the vacuum- and relative-permittivities, and the electronic charge. The spatial concentration of the charged traps, N, corresponding to the space-charge density ρ is considered to be unsigned, i.e.,

$$N = |\rho|/e. \tag{I.2.9}$$

As the carriers generated under the contact of a planar detector travel to the corresponding electrode, the loss of drifting charge, Q, due to carrier trapping is given by

$$Q(t) = Q_0 e^{-t/\tau} \tag{I.2.10}$$

with the trapping time τ and the initial generated charge Q_0.

Using Eq. (I.2.2) the kinetic equation describing electron drift through the sample, $\mathrm{d}x/\mathrm{d}t = v(t) = \mu E(x)$, is easily solved as

$$x(t) = \frac{E_0}{a}\left(1 - e^{-a\mu t}\right). \tag{I.2.11}$$

On generalization of latter equation for holes, the current $i(t)$ induced by moving charge carriers generated by α-particles irradiating the appropriate electrode of a planar detector (cathode when collecting electrons, anode when collecting holes) can be written in the form

$$i(t) = \frac{Q(t)v(t)}{L} = \frac{Q_0 E_0 \mu}{L} e^{-(\pm a + \frac{1}{\mu\tau})\mu t} \propto e^{-ct}. \tag{I.2.12}$$

In this equation as well as further in the text where ± or ∓ are used, the upper signs hold for collection of electrons, the lower signs for collection of holes. With all charge carriers being created at one moment and immediately starting to drift in applied electric field, the current transient would be described by the latter equation, having infinitesimally sharp rising and trailing edges, see Fig. I.2.2a. However, because of the plasma effect that delays the charge collection, sample inhomogeneities, carrier trapping/detrapping, or distortion of the waveform due to electronics, the actual observed current transient when using an α-particle radiation source is much more similar to that shown in Fig. I.2.2b, i.e., with finite rising and trailing edges. After its rise up, the waveform is exponentially decreasing (increasing) according to Eq. (I.2.12) and then it breaks at the moment when the forefront of the charge “cloud” generated under the irradiated electrode have travelled the whole

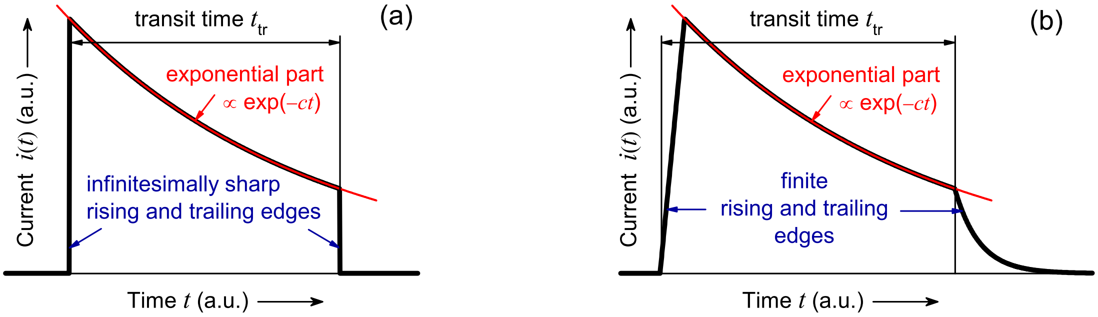

Figure I.2.2: (a) Idealized current waveform and (b) a typical current waveform recorded by a digital storage oscilloscope performing a TCT measurement using α-particles.

thickness of the sample and reaches the opposite electrode. With increasing bias the waveform shrinks and its transit time decreases since it takes less time for carriers to drift through the sample, as will be seen later.

Eq. (I.2.12) can be fitted to the experimental data and the damping parameter

$$c = \left(\pm a + \frac{1}{\mu\tau} \right) \mu \tag{I.2.13}$$

can be established. It should be noted that using a damped exponential in the form given by Eq. (I.2.12) even for the fitting of rising current waveforms is essential for correct interpretation of results of measurements.

If the depletion region spreads over the whole detector volume ($\mathcal{L} = L$), the applied bias U is related to the electric field:

$$U = E\left(\frac{L}{2}\right) L = E_0 L - \frac{1}{2} a L^2. \tag{I.2.14}$$

The arrival of drifting carriers to the opposite electrode identified by a clear drop of a current transient allows to determine the charge transit time, t_{tr}. For electrons the following equation holds:

$$x(t_{tr}) = \frac{E_0}{a}(1 - e^{-a\mu t_{tr}}) = L. \tag{I.2.15}$$

When the polarization can be neglected, i.e., for the case of $a \to 0$, the latter equation reduces to $x(t_{tr}) = E_0 \mu t_{tr} = L$. This easily originates from the first two terms of the Taylor expansion of the exponential $e^{-a\mu t_{tr}} \approx 1 - a\mu t_{tr}$ that holds for small a. Then, since $E(x) = E_0 = U/L$ from Eqs. (I.2.2) and (I.2.14) (homogeneous electric field within the detector), the last equation can be written in the form

$$\mu t_{tr} = \frac{L^2}{U}, \tag{I.2.16}$$

which is often used for the evaluation of the carrier mobility from the measurements of the transit time t_{tr}. The assumption of homogeneous electric field is crucial in this case.

When polarization occurs the experimental data $\mu\tau$, c, and t_{tr} can be combined together with Eq. (I.2.15), where E_0 and μ are eliminated with the help of Eqs. (I.2.13) and (I.2.14). After generalizing the result also for the case of hole collection, the final transcendental equation for a is obtained:

$$c t_{tr} = \left(1 \pm \frac{1}{a\mu\tau} \right) \ln \left(\frac{1 \pm \frac{aL^2}{2U}}{1 \mp \frac{aL^2}{2U}} \right). \tag{I.2.17}$$

Table I.2.1: Interpretation of the results of calculations

Solution of Eq. (I.2.17)[§]	Strength of the electric field $E(x)$	Space-charge density ρ
$a > 0$	Decreasing from C → A[†]	Positive, $\rho > 0$
$a < 0$	Decreasing from A → C[†]	Negative, $\rho < 0$

[§] In Eqs. (I.2.12)–(I.2.17) the upper sign in $\pm$ or $\mp$ terms corresponds to collection of electrons (α-source from the cathode side), the lower sign must be used for measurements collecting holes (detector irradiated from the anode side).

[†] "C" marks the cathode, "A" marks the anode of the detector.

Though the transcendental equation must be solved numerically, the field slope a and, consequently, all remaining parameters E_0 and μ may be found for each current pulse.

If the applied bias is low and the electric field is completely screened near one contact ($\mathcal{L} = W < L$), an inactive region appears under that electrode and the transit time is undefined in such a case. Eq. (I.2.17) cannot be used since $t_{tr} \to \infty$. If, however, the experimental setup allows to apply higher voltage sufficient to overcome the dead layer (see Eq. (I.2.23) later in the text), nothing prevents from using Eq. (I.2.17). Then, adopting the assumption of the bias-independent μ, the value determined from the analysis of current pulses at high biases can be inserted into Eq. (I.2.13) to calculate the profile of the electric field at low bias voltages.

To reconstruct the profile of the electric field from the solution of Eq. (I.2.17), one can use Eqs. (I.2.2) and (I.2.3). However, to successfully solve Eq. (I.2.17), the following important note must be taken into account: The shape of a recorded current transient is governed by the profile of the electric field in the direction of carrier motion, whereas the field strength $E(x)$ in Eq. (I.2.2) describes the profile from the cathode to the anode. Consequently, as holes drift from the anode towards the cathode, the signs in terms containing a in Eqs. (I.2.12)–(I.2.17) for holes are opposite to those for electrons. One must take care and precisely follow the sign convention, otherwise wrong results are obtained.

Two examples are provided for clarity: Firstly, let us assume that electron signal from TCT was recorded and, at a particular bias U_1, $a_1 = 3$ kV/cm^2 was obtained by solving Eq. (I.2.17) with upper signs (Fig. I.2.3a). From Table I.2.1, one can immediately find out that since $a_1 > 0$, the electric field is decreasing from the cathode towards the anode. To calculate its spatial distribution, $a = a_1$ should be used in Eqs. (I.2.2) and (I.2.3) (Fig. I.2.3b). The trap concentration $N_1 = 1.7 \times 10^{10}$ cm^{-3} results directly from Eq. (I.2.9). Secondly, moving the α-particle source so as to irradiate the anode of the sample, at a bias U_2 high enough to collect holes, the field slope, e.g., $a_2 = -4$ kV/cm^2 may result from Eq. (I.2.17) written with lower signs (Fig. I.2.3c). Again from Table I.2.1, $a_2 < 0$ yields that the electric field is increasing from the cathode towards the anode (Fig. I.2.3d). Trap concentration $N_2 = 2.3 \times 10^{10}$ cm^{-3} is evaluated from Eqs. (I.2.9) and (I.2.8) in this case.

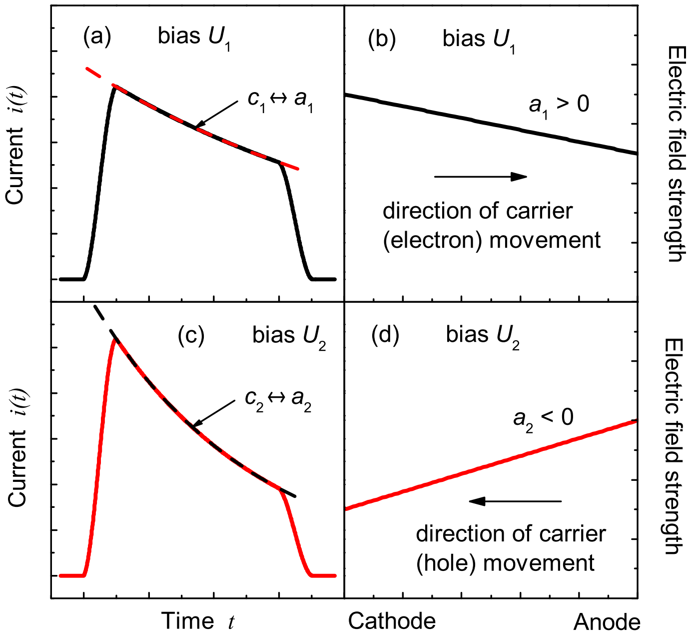

Figure I.2.3: TCT calculations and application of Table I.2.1 demonstrated on two examples from the text. Note that the electron and hole transients look the same although the slopes of the electric field profiles are opposite.

2.2 Charge-collection efficiency

As discussed above, CdTe and CZT detectors are primarily used for room-temperature detection of high energy radiation, i.e., γ-, X-ray, or α-particles from various sources. Since these materials are semiconductors, incident radiation/particle generates electron–hole pairs, which are collected by the internal electric field within the device. To evaluate the amount of collected charge, so called *charge-collection efficiency (CCE)* is used. It is defined as a dimensionless quantity

$$CCE \equiv Q/Q_0, \tag{I.2.18}$$

where Q is total charge collected on detector electrodes when irradiated by a source generating the charge Q_0 in the detector. The definition of CCE ensures that $CCE \leq 1$, if no gain is introduced during collection. The value of Q_0 is different for different detector materials since the number of generated electron–hole pairs is material dependent. Q_0 can be calculated from the electron–hole pair production energy, ϵ, the values of which for some common materials are summarized in Table 0.3.1. The following relation holds:

$$Q_0 = e\mathcal{E}_0/\epsilon, \tag{I.2.19}$$

if $\mathcal{E}_0$ is the energy of a particular peak in the pulse height spectrum of the radiation source and e is the electronic charge. Typical values of generated charge are, respectively, $Q_0^{(100\,\mathrm{keV})} \approx 4$ fC and $Q_0^{(5\,\mathrm{MeV})} \approx 200$ fC for 100 keV and 5 MeV source, and $\epsilon = 4$ eV.

There is a simple idea which shows that it is the mobility–lifetime product, $\mu\tau$, what is the important material parameter indicating of how well a material will perform for spectrometer applications. Assuming a uniform volume excitation that generates free electrons, then the generated photocurrent, I_{ph}, is expressed by [7]

$$I_{\mathrm{ph}} \propto \mu\tau U/L^2.$$

Here, L is the detector thickness and U is the applied bias. Although it is the integrated charge what is measured during the CCE measurements rather than actual current, it holds true that CCE in Eq. (I.2.18) strongly depends on $\mu\tau$ and U; CCE → 1 with increasing values of these two quantities.

For the case of homogeneous electric field within a planar detector and under the assumption of dominant effect of one type of carriers (either electrons or holes) on charge collection, Eq. (I.2.18) can be expressed in the form of well-known single-carrier Hecht equation [41]:

$$CCE_{\mathrm{Hecht}}(U) = \frac{\mu\tau U}{L^2}\left(1 - e^{-\frac{L^2}{\mu\tau U}}\right). \tag{I.2.20}$$

Charge trapping according to Eq. (I.2.10) and generation of carriers close to the contact are involved in latter equation.[3]

When the electric field is inhomogeneous, Eq. (I.2.20) cannot be used. In this case, the general expression [42]

$$CCE = \frac{1}{L}\int\limits_0^L \exp\left(-\int\limits_0^{x'} \frac{\mathrm{d}\xi}{\mu\tau E(\xi)}\right)\mathrm{d}x' \tag{I.2.21}$$

has to be employed to calculate CCE. Generally, CCE depends on the polarity of the accumulated charge and the type of collected carriers. For the case of linear electric field profile, $CCE(U,a)$ as a function of applied bias and field slope can be calculated after the substitution of Eq. (I.2.2) into Eq. (I.2.21), yielding

$$CCE(U,a) \ = \ \begin{cases} 0 & \text{for } \pm a \leq 0,\ U \leq U_{\mathrm{th}}, \\ \frac{1}{L}\frac{\mu\tau a}{\mu\tau a \pm 1}W & \text{for } \pm a > 0,\ U \leq U_{\mathrm{th}}, \\ \frac{1}{L}\frac{\mu\tau a}{\mu\tau a \pm 1}\left[\left(\frac{L}{2} \mp \frac{U}{La}\right)\left(\frac{\frac{U}{La}-\frac{L}{2}}{\frac{U}{La}+\frac{L}{2}}\right)^{\frac{1}{\mu\tau a}} + \frac{L}{2} \pm \frac{U}{La}\right] & \text{for } U > U_{\mathrm{th}}, \end{cases} \tag{I.2.22}$$

where

$$U_{\mathrm{th}} = \frac{|a|L^2}{2} \tag{I.2.23}$$

is the minimum (threshold) voltage necessary to suppress the dead layer within the device. Eq. (I.2.22) is applicable whatever the space charge and carrier type. It is, however, important to use correct signs (even in the conditional statements in Eq. (I.2.22)), depending on the carriers being collected.

Accumulated space charge could be so high as to cause the incomplete depletion of the sample. In such a situation, the depletion width calculated using Eq. (I.2.4) is less than the detector thickness and an inactive region (a dead layer) of zero charge collection appears within the bulk, $\mathcal{L} = W < L$, as illustrated in Fig. I.2.1. This inconvenience can be overcome by increased bias greater than its threshold value given by Eq. (I.2.23).

It is interesting to note that Eq. (I.2.22) diverges for $a = \mp 1/\mu\tau$, which for typical values of $\mu\tau = 10^{-3}$ cm^2/V for electrons and the detector thickness of $L = 1$ mm yields $a = \mp 1$ kV/cm^2 and $U_{\mathrm{th}} = 5$ V. These values represent practically non-polarized detector with nearly flat profile of the electric field, and, naturally, with fully-depleted volume as

---

[3] General expression for position-dependent CCE exists, which can be used to calculate $CCE(x)$ at any position x within the detector bulk. This is interesting for applications utilizing γ- or X-ray radiation; however, for α-particles it is the value of $CCE(x = 0)$ what is important since the carrier generation takes place close to the surface because of high absorption coefficient (low penetration depth) of α-particles in matter.

usual operating voltages of hundreds of volts are two orders-of-magnitude greater than the threshold voltage. It would be inconvenient to discard such cases from analysis because of problems with Eq. (I.2.22). Fortunately, it is easy to show that the limit of Eq. (I.2.22) for $a \to \mp 1/\mu\tau$ exists and that this equation can be continuously extended on all values of a. For an unpolarized detector ($a \to 0$), Eq. (I.2.22) reduces to the simple Hecht formula (I.2.20).

2.3 Relation between TCT and CCE

The TCT is based on the analysis of current transients, $i(t)$, induced by moving carriers and measured by a current-sensitive preamplifier (CSP). If one identifies the moment when generated carriers start to drift with $t = 0$, then, neglecting the plasma effect (see later Section 2.7) and carrier trapping/detrapping, the transient ends at $t = t_{tr}$, see Fig. I.2.2. The total amount of charge, Q, induced on the electrodes of the detector during the carrier movement (and calculated by the integration of $i(t)$) must be the same as that which would be directly registered, all other things being equal, by the charge-sensitive preamplifier (ChSP) placed instead of CSP. Mathematically,

$$Q = \int_0^{t_{tr}} i(t)\,\mathrm{d}t. \tag{I.2.24}$$

Substituting for $i(t)$ from Eq. (I.2.12), the latter equation can be evolved in the following way:

$$Q = \frac{Q_0 E_0 \mu}{L} \int_0^{t_{tr}} e^{-(\pm a + \frac{1}{\mu\tau})\mu t}\,\mathrm{d}t = \frac{Q_0 E_0 \mu}{L} \frac{1}{(\pm a + \frac{1}{\mu\tau})\mu} \left[1 - e^{-(\pm a + \frac{1}{\mu\tau})\mu t_{tr}}\right]. \tag{I.2.25}$$

To proceed further, little simplification has to be made. Therefore, under the assumption that the polarization of the detector is very low, $a \to 0$, which as shown in Section 2.1 implies that $E_0 = U/L$ and $\pm a \ll \frac{1}{\mu\tau}$, a can be neglected both in the exponent and denominator in Eq. (I.2.25). Thus,

$$Q = Q_0 \frac{\mu\tau U}{L^2} \left(1 - e^{-\frac{t_{tr}}{\tau}}\right). \tag{I.2.26}$$

Finally, since Eq. (I.2.16) holds in the case of little polarization, one obtains

$$\frac{Q}{Q_0} = \frac{\mu\tau U}{L^2} \left(1 - e^{-\frac{L^2}{\mu\tau U}}\right). \tag{I.2.27}$$

Taking into account the definition of CCE given by Eq. (I.2.18), one immediately realizes that the latter equation is the well-known Hecht equation, Eq. (I.2.20). Thus, there is an integral relation between TCT and CCE.

This procedure can be used to verify measured TCT and CCE data; however, practical realization is limited due to relatively high noise in numerically integrated current transients in comparison to directly measured CCE.

2.4 Iterative procedures: The conjunction of the TCT and the CCE analysis

To precisely evaluate $\mu\tau$, Eq. (I.2.22) should be used instead of Eq. (I.2.20). However, using Eq. (I.2.22) necessitates the information about the polarization state of the detector,

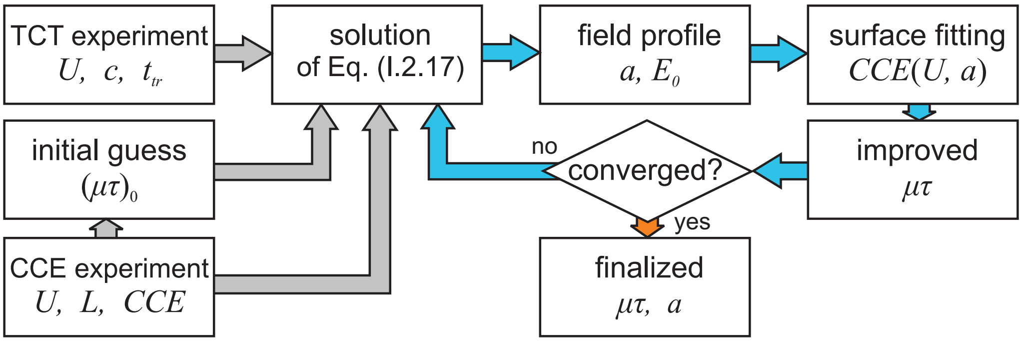

Figure I.2.4: Flow chart of the self-consistent procedure (SCP) for the evaluation of $\mu\tau$ in polarized detectors.

since a is required for the calculation. This could be achieved by TCT measurement as the solution of Eq. (I.2.17) brings values of the field slope a. The proper evaluation sequence would then be firstly calculate the field slope and then evaluate $\mu\tau$. Since it is necessary to know the value of $\mu\tau$ before calculating a, the procedure has to be done iteratively. As both the TCT and CCE measurements performed in the laboratory of IoP CU use the same radiation source (α-particles from ^{241}Am) and it could be easily arranged that the source–detector distance is the same in both experiments, the electric field profile could be measured under the same conditions as the collection of radiation spectra. Two iterative approaches for the calculation of $\mu\tau$ are described in the following sections. These methods represent one of the original results of this thesis and push the way of processing of experimental data forward as both the TCT and CCE measurements are processed simultaneously to bring results which would not be accessible by separate measurements. The interest in these methods was proven by their publication in reputable journals [26, 27].

2.4.1 Self-consistent procedure

The iterative procedure—so called the *self-consistent procedure (SCP)*, is carried out as follows (see Fig. I.2.4):

(a) From the TCT measurement the values of c and t_{tr} for different applied bias voltages U are obtained. Measured radiation spectrum (CCE) is processed to obtain the initial value of mobility–lifetime product, $(\mu\tau)_0$. This can be done by fitting $CCE(U)$ either via the Hecht equation (I.2.20) or using Eq. (I.2.22) with the bias-independent effective field slope, $a = a_{\text{eff}}$.

(b) The estimated value of mobility–lifetime product is used to solve Eq. (I.2.13), yielding the field slope a as a function of U; the electric field profiles are then easily calculated using Eqs. (I.2.2) and (I.2.3).

(c) CCE is fitted according to Eq. (I.2.22), taking into account the bias dependence of a determined in step (b). Improved value of $\mu\tau$ is obtained.

(d) The value of $\mu\tau$ from the previous step is used for the next iteration, starting at step (b). The procedure runs in a loop until it converges or required precision is achieved.

It is important to note that in step (c) the measured bias dependence of the electric field slope a is included into calculations, in contrary to the procedure presented in [29], where an "effective" bias-independent field slope a_{eff} is one of the fitting parameters. The procedure with a_{eff} is referred to as the Matz approach later in the text. This approximation is only used in step (b) to obtain the initial guess of mobility–lifetime product. In SCP, bias dependence of the profiles of the electric field is considered and, instead of a common one-dimensional curve fitting (Hecht [41], Matz and Weidner [29]), two-dimensional surface fitting of the data points $[U, a_U, CCE_U]$ is performed according to Eq. (I.2.22) in the three-dimensional space. The symbol a_U was used to denote the resulting value of the field slope corresponding to the measured damping parameter c and the transit time t_{tr} at bias U, CCE_U marks the corresponding CCE.

After each iteration, not only $\mu\tau$ and the electric field profiles are improved, the carrier mobility, μ, is amended as well due to the involvement of the refined field profile. Convergence of the method decreases with increasing $|a|$ over $1/\mu\tau$. For $|a| \gg 1/\mu\tau$, the exact value of $\mu\tau$ cannot be evaluated properly. Further discussion of this case is given in Subsection 2.4.3 later in the text.

2.4.2 Direct-minizimation procedure

Instead of using the self-consistent procedure, one can try to directly minimize the function

$$\chi^2(\mu\tau) = \sum_U \left[CCE_U - CCE(U, a_U(\mu\tau))\right]^2 \tag{I.2.28}$$

representing the sum of squares of differences between the measured values of the charge-collection efficiency CCE_U at bias U from their theoretical values calculated with the help of Eq. (I.2.22). The symbol $a_U(\mu\tau)$ denotes the solution of Eq. (I.2.17) corresponding to the experimental values c and t_{tr} measured at bias U, but calculated for the instant value of $\mu\tau$ during the computation. This *direct-minimization procedure (DMP)* is carried out in the following way (see Fig. I.2.5):

(a) From the TCT measurement the values of c and t_{tr} for different applied bias voltages U are obtained. Measured radiation spectrum (CCE) is processed to obtain the initial value of mobility–lifetime product, $(\mu\tau)_0$.

(b) The estimated value of mobility–lifetime product is used to evaluate Eq. (I.2.28), yielding the initial value of χ^2.

(c) Eq. (I.2.28) is minimized with respect to $\mu\tau$; for any instant value of $\mu\tau$ the corresponding field slope $a_U(\mu\tau)$ is calculated using Eq. (I.2.17).

(d) When the procedure converges, the $\mu\tau$ that best fits the experimental data and the profiles of the electric field are provided.

Though no analytical solution of the transcendent Eq. (I.2.17) exists, $a_U(\mu\tau)$ must be calculated numerically in step (c). The function χ^2, dependent only on the value of $\mu\tau$, is minimized using some common numerical method [43].

The main difference between the direct-minimization and the self-consistent procedures is that the DMP takes the local variations of a into account for any arbitrarily small change in $\mu\tau$, whereas in the SCP a is fixed at each step to find the improved value of $\mu\tau$. Consequently, it may happen that the SCP converges to a solution which is not a minimum of χ^2. The comparison of these two methods and their applications are reported in Section 2.5 as well as in Chapter 4.

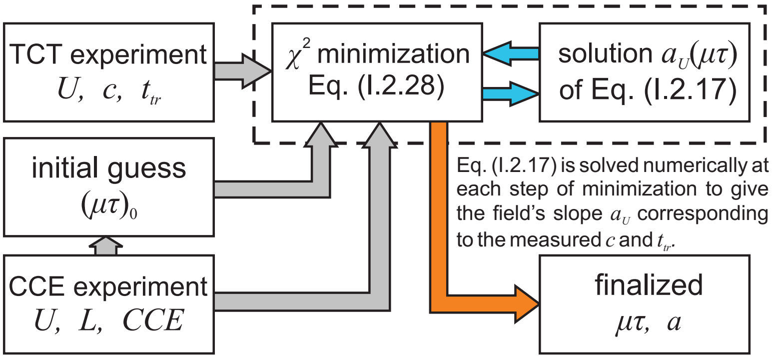

Figure I.2.5: Flow chart of the direct-minimization procedure (DMP) for the evaluation of $\mu\tau$ in polarized detectors.

2.4.3 Strongly-polarized detectors

For strongly-polarized detectors, i.e., those for which $|a| \gg 1/\mu\tau$ holds, the fundamental equations can be further simplified. Consequently, Eq. (I.2.13) reduces to

$$c = \pm a\mu \qquad \text{if } |a| \gg 1/\mu\tau. \tag{I.2.29}$$

It is reasonable to suppose that for voltages U in the order of hundreds of volts the applied bias is less that the threshold value, $U < U_{\mathrm{th}}$. Thus, the inactive region occupies the significant portion of the detector volume, the current pulse is pure exponential according to Eq. (I.2.12) with no break corresponding to the transit time, and only the first two cases in Eq. (I.2.22) come into question. For $a \leq 0$ for electrons or $a \geq 0$ for holes, no further information can be brought out from radiation pulse height spectra since $CCE \equiv 0$ in this case. If, however, $a > 0$ for electrons or $a < 0$ for holes, the CCE simplifies to W/L and using Eq. (I.2.4), it can be written in the form

$$CCE(U, c) = \frac{W}{L} = \frac{1}{L}\sqrt{\frac{2\mu U}{c}} \qquad \text{if } |a| \gg 1/\mu\tau. \tag{I.2.30}$$

The mobility–lifetime product cannot be determined for strongly-polarized detectors because there is no $\mu\tau$ in Eq. (I.2.30). Nevertheless, at least the estimate of carrier mobility, μ, can be calculated by fitting Eq. (I.2.30) to experimental data; with no need for self-consistent procedure or χ^2 minimization.

2.5 Iterative procedures in detail: Simulated experimental data

Simulations were performed to assess the benefits of the two iterative methods on artificial data. Eq. (I.2.22) was used to generate CCEs for three “fictional” detectors D1, D2, and D3, each of thickness $L = 1.5$ mm, mobility $\mu_0 = 1000$ cm^2/Vs, and mobility–lifetime product $\mu\tau_0 = 1{\times}10^{-3}$ cm^2/V. The polarization states of these detectors are assumed to be as follows: the detector D1 is attributed to be almost unpolarized, having $a_0 = 5$ kV/cm^2 not varying with applied bias; the more polarized detector D2 with the constant field slope of $a_0 = 25$ kV/cm^2 is not fully depleted until the bias of 300 V is applied; and, finally, the strongly-polarized detector D3, the entire volume of which is depleted just above 700 V, has a varying from 30 kV/cm^2 at 100 V to 70 kV/cm^2 at 800 V.

Table I.2.2: Results of $\mu\tau$ calculations on simulated data

Sample	$\mu\tau$ (10^{-3} cm^2/V)			
	Hecht	Matz	our approach	
			SCP	DMP
D1	1.14	1.00	1.00	1.00
D2	0.17	1.00	1.00	1.00
D3	0.12	0.09	0.92	0.93

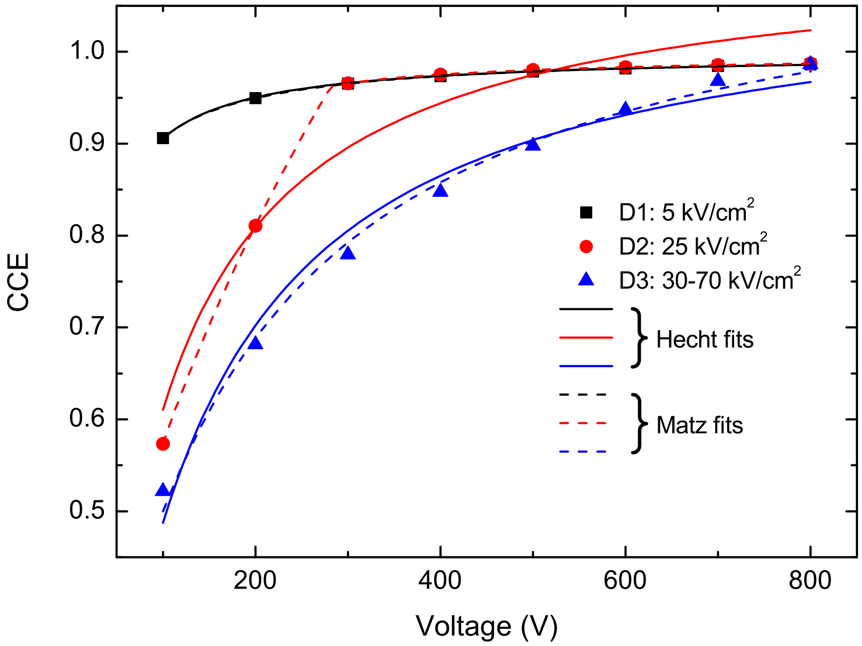

Figure I.2.6: Fits of simulated CCEs of "fictional" detectors D1, D2, and D3. Solid lines show the fits according to the Hecht equation, dashed lines refer to the Matz fits. Although they give physically wrong results, the fits of D3 describe the simulated data well.

These data were analyzed utilizing various procedures to calculate the mobility–lifetime product of a particular detector, the value of which was then compared with the initial value $\mu\tau_0$. The values of $\mu\tau$ were obtained by four methods:

(i) fitting of CCE via the Hecht equation (I.2.20);

(ii) fitting of CCE according to Matz and Weidner [29] using Eq. (I.2.22) with $a = a_{\text{eff}}$;

(iii) the self-consistent procedure (SCP) according to Subsection 2.4.1;

(iv) the direct-minimization procedure (DMP) according to Subsection 2.4.2.

The results of (i) and (ii) applied on D1, D2, and D3 detectors are depicted in Fig. I.2.6, those of (iii) and (iv) are shown in Fig. I.2.7. Overall summary is given in Table I.2.2.

For the detector D1 the calculated value of $\mu\tau = 1.14 \times 10^{-3}$ cm^2/V is 14% higher than the original true value $\mu\tau_0$; for the D2 and D3 detectors $\mu\tau$s are one order-of-magnitude

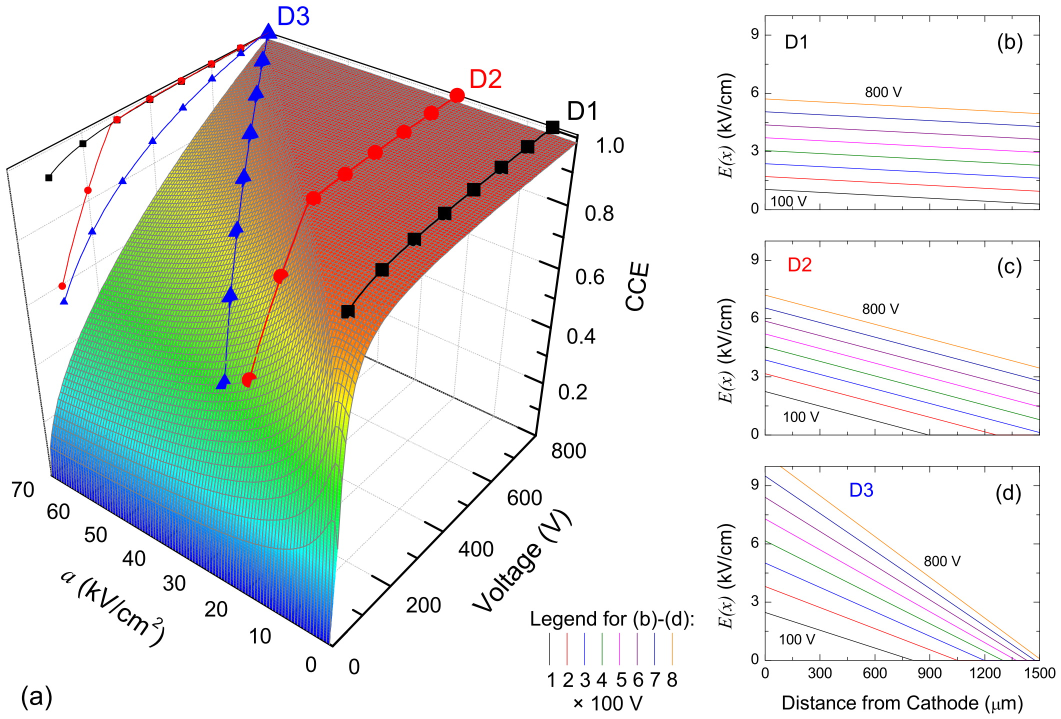

Figure I.2.7: (a) Two-dimensional surface fits of simulated CCEs of "fictional" detectors D1, D2, and D3, and (b)–(d) the reconstructed profiles of the electric fields in these detectors.

less than $\mu\tau_0$. It is clearly demonstrated that the fitting of CCE according to the Hecht equation yields sufficient results only when the detector polarization is low enough to be neglected; the systematic error of the method increases with increasing polarization.

More interesting are the results of the Matz fits. For the D1 and D2 detectors this method gives absolutely exact results and, additionally, recovers the original polarization of the detectors, i.e., $a_0 = 5$ kV/cm^2 for D1 and $a_0 = 25$ kV/cm^2 for D2. This is not very surprising, since the constant field slope is the assumption of this method and the "experimental" data for D1 and D2 were simulated with $a = a_{\text{eff}}$. However, when the slope of the electric field varies with bias, which is the case of the detector D3, the evaluation of $\mu\tau$ from CCE measurements fails, giving almost the same wrong value as the Hecht analysis. It is, however, worth noting that the "goodness of fit" (measured, e.g., through the coefficient of determination,[4] R^2) is high, $R^2 \to 1$, as seen in Fig. I.2.6 for both the Hecht and Matz fitting procedures applied on D3. Therefore, care should be generally taken during the interpretation of the results of CCE analysis, since $R^2 \to 1$ need not be a good criterion for the assessment of the correctness of the fitting method (and validity of obtained results). There is, however, no way how to examine the results based on the CCE measurements only without the additional information about the field profile. If the polarization cannot be neglected ($U < U_{\text{th}}$ in some part of applied bias range) and the field slope varies with applied bias, $\mu\tau$ can be seriously underestimated even by the Matz approach.

---

[4] R^2 indicates how well data points fit a curve. In most cases R^2 is defined as $1 - S_{\text{res}}/S_{\text{tot}}$, where S_{res} and S_{tot} are, respectively, the residual and the total sum of squares.

Both the SCP (0.92×10^{-3} cm^2/V) and DMP (0.93×10^{-3} cm^2/V) converge after several iterations close to $\mu\tau_0 = 1 \times 10^{-3}$ cm^2/V. Though the original value is not restored, the results are much better than those obtained by the first two methods, giving the error less than 10%. The reason for why even the advanced methods did not converge exactly to the original value lies in the relation between a and $\mu\tau$. As mentioned in Section 2.4, the convergence of the methods decreases with increasing $|a|$ over $1/\mu\tau$. For the detector D3, a could be as high as 70 kV/cm^2 while $1/\mu\tau_0 = 1$ kV/cm^2. Even is such a disadvantageous situation the procedures converge quite well and yield more precise results than any other procedure. In addition, the mobility is recovered excellently to $\mu = 1001$ cm^2/Vs.

All above observations can be easily explained with the help of Fig. I.2.7. The fitting procedure according to Hecht tries to fit the three-dimensional data $[U, a_U, CCE_U]$ forming a curve in space by a function given by Eq. (I.2.20), which, however, lies in the plane $a = 0$. The fitting procedure according to Matz and Weidner does the same using Eq. (I.2.22) with a constant a, trying to find the optimum value a_{eff} for which the projections of $[U, a_U, CCE_U]$ on the plane $a = a_{\text{eff}}$ are best fitted. This could only be sufficiently done if a_U does not change significantly with U. On the contrary, both iterative methods do not project the actual three-dimensional data on a plane but rather try to find such a surface described by Eq. (I.2.22) that satisfies the corresponding convergence criterion. This is the only suitable way how to acquire correct results on detectors with extended polarization.

2.6 The conjunction of the Pockels effect and the CCE analysis

Iterative self-consistent and direct-minimization procedures presented in previous sections are specific procedures applied to calculations utilizing the TCT since Eqs. (I.2.17) and (I.2.22) have to be solved simultaneously. After each iteration (change in instant value of $\mu\tau$), the consecutive value of a_U changes as the procedure advances since it is c_U (the damping parameter corresponding to bias U) rather than a_U that is measured directly in the experiment. If, however, a_U were directly measurable, Eq. (I.2.22) could be downright used to perform the surface fitting and obtain $\mu\tau$. That is exactly what the Pockels effect experiment offers. In conjunction with CCE measurements, the correct value of $\mu\tau$ can be calculated taking the polarization of the detector into account. However, problems could arise ensuring both measurement being made under same conditions.

It is advisable to perform further investigations in the field of detector polarization utilizing presented methods. Discarding the polarization could lead to significant error in the evaluation of $\mu\tau$.

2.7 Plasma effect

In contrast to fast rising edge of the current waveform depicted in Fig. I.2.2, experimental observations show that the transient rise time, $t^{(\text{rise})}$, could be much longer and it could take even more than 10 ns for the pulse to reach its maximum. In addition, $t^{(\text{rise})}$ is observed to decrease with increasing bias applied on a detector. Such behaviour can be attributed to the plasma effect [44, 45, 46, 47]. Assuming that a $\sim$5 MeV α-particle is completely absorbed 10–20 μm[5] under the irradiated contact and that the energy for

---

[5] Combined effect of α-particle penetrating metal contact and detector bulk.

creating an electron–hole pair is 4.4 eV in CdTe (see Table 0.3.1), then approximately 10^6 electron–hole pairs are created along the path of an α-particle, thereby forming a charge cloud. These carriers are subject to electric field in a detector; however, it takes some time for the electric field to erode the cloud since the electrons and holes are electrostatically attracted to one another and the applied field is screened within the cloud.

Away from complex numerical simulations, the plasma effect can be phenomenologically understood on a very simple basis. The charge motion in a detector of linear electric field profile is described by Eq. (I.2.11), implying that the induced current recorded on the detector electrodes is exponentially decreasing with time according to Eq. (I.2.12). Supposing that any carrier escaping from the cloud starts to drift towards the corresponding electrode immediately after its emission from the cloud while its motion is governed by Eq. (I.2.11) except that the movement is delayed by time t' the carrier spent in the cloud, its contribution $\Delta i(t,t')$ to the total current measured at time t is

$$\Delta i(t,t') = i_0 e^{-c(t-t')} \chi_{\langle 0,t_{tr}\rangle}(t-t'), \tag{I.2.31}$$

where t_{tr} denotes again the transit time and $\chi_{\langle a,b\rangle}(t)$ is the normalized boxcar function, which is zero for all values of t except those from a single interval $\langle a,b\rangle$, i.e.,

$$\chi_{\langle a,b\rangle}(t) = \begin{cases} 1 & \text{if } t \geq a \text{ and } t \leq b, \\ 0 & \text{otherwise.} \end{cases}$$

If all carriers are emitted from the cloud with a constant rate and brought under the effect of inner electric field within the time t_p needed for the plasma cloud to erode, then the total current $i(t)$ is calculated as

$$i(t) = \int_0^{t_p} \Delta i(t,t')\,\mathrm{d}t'. \tag{I.2.32}$$

Otherwise, if the emission rate is time-dependent a phenomenological function $n(t)$, an emission rate of charge carriers from the plasma cloud which represents the number of carriers per unit time emitted from the cloud, can be defined so that Eq. (I.2.32) can be written in the form

$$i(t) = \int_0^{t_p} n(t')\Delta i(t,t')\,\mathrm{d}t'. \tag{I.2.33}$$

It can be assumed that the plasma cloud totally erodes before first carries reach the opposite contact, i.e., $t_p < t_{tr}$. Then, it follows straightforwards from Eqs. (I.2.31) and (I.2.33) that the recorded current transient stays exponential in the interval $\langle t_p, t_{tr}\rangle$ no matter of plasma erosion mechanism determining the character of $n(t)$. That is because when all carriers are already in motion, the contribution of any of them to measured current $i(t)$ is exponential according to Eq. (I.2.31) and does not change the shape of $i(t)$. Consequently, although the true shape of the current transient for $t < t_p$ need not be available by the TCT experiment due to the plasma effect distortion, the transient exponential damping parameter c is not affected by plasma effect for $t > t_p$ and the electric field, even under the irradiated electrode, can be calculated (the profile close to the irradiated contact can be extrapolated from the field behaviour in the rest of the detector). Typical current waveforms calculated for three different emission rates are shown in Fig. I.2.8.

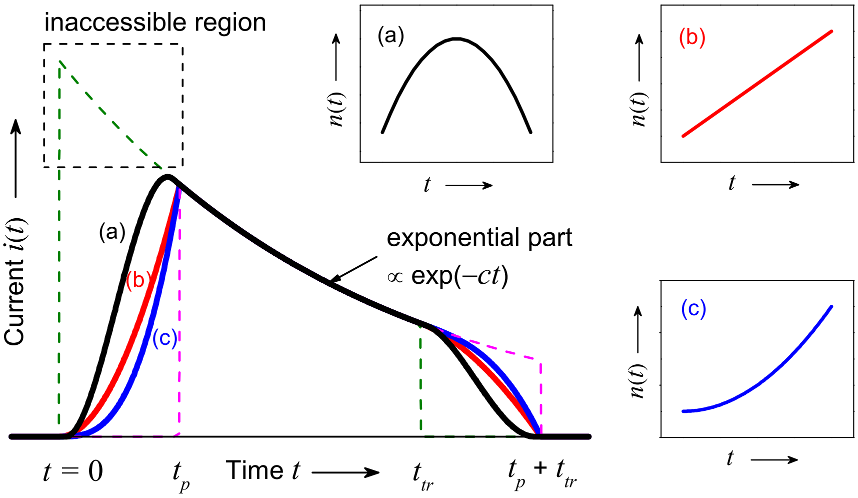

Figure I.2.8: Typical current waveforms distorted due to the plasma effect. All waveforms have been normalized to demonstrate the same exponential behaviour in the middle part of the pulse. Solid lines show curves corresponding to (a) gaussian, (b) linear, and (c) quadratic carrier emission rate $n(t)$ depicted in the insets; dashed green and magenta lines show the first (beginning at $t = 0$) and the last (beginning at $t = t_p$) normalized pulse. The exponential-shaped transient for $t < t_p$ (marked as "inaccessible region") cannot be recorded correctly because of the plasma-effect distortion.

In addition, $n(t)$ can be calculated from current waveforms. To do so, Eq. (I.2.33) should be rewritten as follows:

$$i(t) = \int_0^{t_p} n(t')\Delta i(t,t')\,\mathrm{d}t' = \int_{-\infty}^{\infty} n(t')\Delta i(t,t')\,\mathrm{d}t' = (n * \Delta i)(t), \tag{I.2.34}$$

where, after the third equal sign, the convolution of carrier emission rate $n(t)$ and single-carrier current contribution $\Delta i(t)$ is identified. The extension of integration limits from $\langle t_p, t_{tr}\rangle$ over the whole real line was possible due to the presence of the boxcar function in Eq. (I.2.31). The convolution operator "$*$" acting on functions f and g is defined as usual:

$$(f * g)(x) = \int_{-\infty}^{\infty} f(y)g(x-y)\,\mathrm{d}y.$$

Looking directly for the solution $n(t)$ of the integral equation (I.2.33) for the measured current waveform $i(t)$ would be pretty complicated. However, one can use the advantage of the well-known convolution theorem of the Fourier transform instead:

$$\mathcal{FT}\{f * g\} = \mathcal{FT}\{f\}\,\mathcal{FT}\{g\}, \tag{I.2.35}$$

where the symbol $\mathcal{FT}$ was used for Fourier transform operator. Then, the application of Eq. (I.2.35) on Eq. (I.2.34) yields

$$\mathcal{FT}\{i\} = \mathcal{FT}\{n\}\,\mathcal{FT}\{\Delta i\},$$

from which after simple math

$$n(t) = \mathcal{FT}^{-1}\left\{\frac{\mathcal{FT}\{i\}}{\mathcal{FT}\{\Delta i\}}\right\}. \tag{I.2.36}$$

Here, the symbol $\mathcal{FT}^{-1}$ marks the inverse Fourier transform. For fast numerical processing, one can utilize some of common codes for the discrete Fourier transform [43]. Emission rates of real CdTe and CZT detectors calculated using Eq. (I.2.36) are shown in Chapter 4.

3. Experimental techniques

In Table I.3.1 the overview of samples studied in Part I of this thesis is given. Only the properties concerning the origin of samples are summarized therein, another properties are shown in detail in corresponding sections, references of which are to be found in the last column of the table. Some of the samples were grown in the growth laboratory of the Institute of Physics of Charles University in Prague (IoP CU), the others were either bought as commercially available detectors or the material for their fabrication was obtained thanks to cooperation between IoP CU and other laboratories interested in the same research area.

3.1 Sample preparation

Investigation of detector properties always starts with the preparation of suitable samples for measurements.

3.1.1 Primary treatment

At first planparallel wafers are cut from a grown crystal perpendicularly to growth axis using a diamond-wire saw Model 6234 from Well Diamond Wire Saws, Inc. The slices with the thickness of approx. 2–3 mm are then polished by a boron-carbide (B_4C) abra-

Table I.3.1: Samples studied in Part I of this thesis.

Sample	Material	Growth technique	Origin (Vendor)	Section in the thesis
AC211	CdTe:Cl	THM§	Acrorad Co. Ltd.	4.1.3
AC31C1	CdTe:Cl	THM	Acrorad Co. Ltd.	4.1
B39KB3	CdTe:In	VGF†	IoP CU[1]	4.1, 4.2
BNL2E2	$Cd_{0.85}Zn_{0.15}Te$	HPBM‡	Brookhaven NL[2]	4.3
BNL2E5	$Cd_{0.85}Zn_{0.15}Te$	HPBM	Brookhaven NL	4.1.3
BNL2E9	$Cd_{0.85}Zn_{0.15}Te$	HPBM	Brookhaven NL	4.1
BNL2G1F3	$Cd_{0.85}Zn_{0.15}Te$	HPBM	Brookhaven NL	4.3
E46D3I	$Cd_{0.96}Zn_{0.04}Te$	VGF	IoP CU	4.2
E67A1C	$Cd_{0.9}Zn_{0.1}Te$	VGF	IoP CU	4.2
E67A1G	$Cd_{0.9}Zn_{0.1}Te$	VGF	IoP CU	4.1.3

§ Travelling Heater Method
† Vertical Gradient Freeze method
‡ High-pressure Bridgman method
[1] Institute of Physics of Charles University in Prague
[2] Brookhaven National Laboratory

sive F600 to reveal grain boundaries within the wafer. This is important since only the monocrystalline pieces of the wafer are suitable for further investigations. The wafer is consequently cut on a steal-wire saw to supply planparallel samples with dimensions usually around $5 \times 5 \times 2$ mm^3 which should contain no grain boundaries or twins.

After the cutting, samples are polished by a B_4C abrasive F1000 to remove the damaged surface layer and to prepare the sample surface for the following chemical–mechanical treatment. This is accomplished by chemical polishing of the sample in a 3% bromine–ethylene glycol solution on a silk cloth, 1 minute for each side. Consequently, the sample is etched in a 3% bromine–methanol solution for 1 minute and then thoroughly rinsed in methanol and then acetone or isopropyl alcohol. This process removes the remains of abrasives and provides the mirror-like surface. For electrical measurements, contacts have to be prepared in the next step.

3.1.2 Deposition of metal contacts

To enable the piece of CdTe/CZT operate as a radiation detector and to allow the realization of various measurements of electrical properties (some of them are discussed in Chapter 4), electrical contacts are prepared on the chemically–mechanically treated surface. Various metals can be utilized (Au, Pt, In, Al, etc.); however, the choice of the metal must be done carefully with respect to the quality of detector material as well as the intended application. In the laboratory of IoP CU, gold contacts are mostly prepared from a 1% $AuCl_3$ solution in water. In addition, Au, In or other metals can be vacuum-evaporated from a resistive heating boat.

No matter of deposition technique, detectors are prepared in a planar geometry, i.e., two contacts are produced on the opposite faces of the sample. Before contacting, sample faces that are not designated for deposition are covered by a resist, whereas those that are to be deposited are left unmasked. After baking of the resist, the contact is deposited either chemically from the solution or by evaporation. At the end of deposition process, the resist is removed in acetone, leaving the unmasked face(s) contacted. If both contacts were not prepared at once, the whole process can be repeated; otherwise the detector is ready for being bonded and wired.

This proceeds by bonding the detector onto a small printed-circuit board (PCB) holder[6] by a conducting graphite (or silver) paste, which tightly fixes the detector in place but can be easily rinsed in acetone when needed. The bonded face serves as one electrode (cathode/anode depending on the polarity of applied bias), the opposite face (anode/cathode) is connected to the PCB using a 50 μm Ag wire. In the geometry that enables α-particle irradiation from both faces, the detector is fixed on the PCB holder by its uncontacted wall-side. This removes the need for unbonding, turning the detector around, and bonding it again. In such a geometry both the anode and cathode are connected by Ag wires to the PCB. When fixed to the PCB holder, the detector is ready for measurements.

---

[6] A piece of custom-made PCB with a large gold electrode and three small gold pads for wiring. Four pins in the corners enable easy fitting of the board with the sample to various experimental setups used in the laboratory without the need for unbonding the detector.

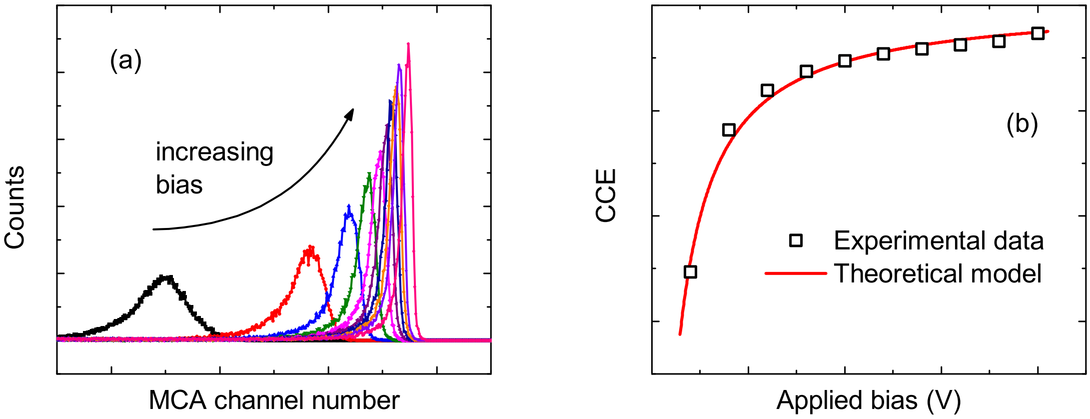

Figure I.3.1: (a) Typical shape of the pulse height spectrum of a CdTe detector for various voltages. (b) Charge-collection efficiency (CCE) evaluated from the measured pulse height spectrum is fitted according to a theoretical model to obtain $\mu\tau$ of the detector.

3.2 Radiation spectra measurements

Measurements of the charge-collection efficiency (CCE) provide important information about the quality of the detector through the evaluation of the mobility–lifetime product ($\mu\tau$) deduced from the measured bias dependence of CCE, see Fig. I.3.1. According to Eq. (I.2.18) one must calculate the amount of charge, Q, collected by the detector biased to a particular voltage when irradiated by a radiation source of known energy, $\mathcal{E}_0$. For CCE measurements presented in this thesis, a 5.49 MeV ^{241}Am α-particle source was used.

The experimental setup based on a common arrangement for radiation spectra measurements [18] is shown in Fig. I.3.2. The detector connected to a charge-sensitive preamplifier (ChSP) is biased to the desired DC voltage by an Iseg SHQ 122M through a series load resistor within the ChSP housing. To minimize energy losses of α-particles irradiating the detector, both the detector and the radiation source are placed in a vacuum chamber while simultaneously keeping the source–detector distance as short as possible. The signal induced on detector electrodes by drifting carriers is fed via a blocking capacitor (to remove the high-voltage DC part of the signal) to the input field-effect transistor (FET) of the Amptek A250 preamplifier. After the pre-amplification it is then shaped and additionally amplified by an Ortec 671 shaping amplifier, the purpose of which is to modify the transients to a form easily registered by a multichannel analyzer (MCA). Shaping of the transient on particular stages along the signal path is depicted at the top of Fig. I.3.2. A digital storage oscilloscope (DSO) is used for real-time checking of the shaped signal during the measurement. Finally, an Ortec Easy-MCA multichannel analyzer supplies the pulse height spectrum recorded and analyzed by a PC. Shielded coaxical cables terminated by either BNC connectors (for signal path) or SHV connectors (for HV supply) were used to interconnect particular instruments.

To calculate CCE as a dimensionless quantity from the pulse height spectrum, i.e., from the distribution of recorded transients according to their height with channel numbers on the horizontal axis, one must find the relationship between a particular MCA channel and a certain energy. This could be achieved in two ways: (i) by performing a pulser calibration; (ii) by using a silicon detector.

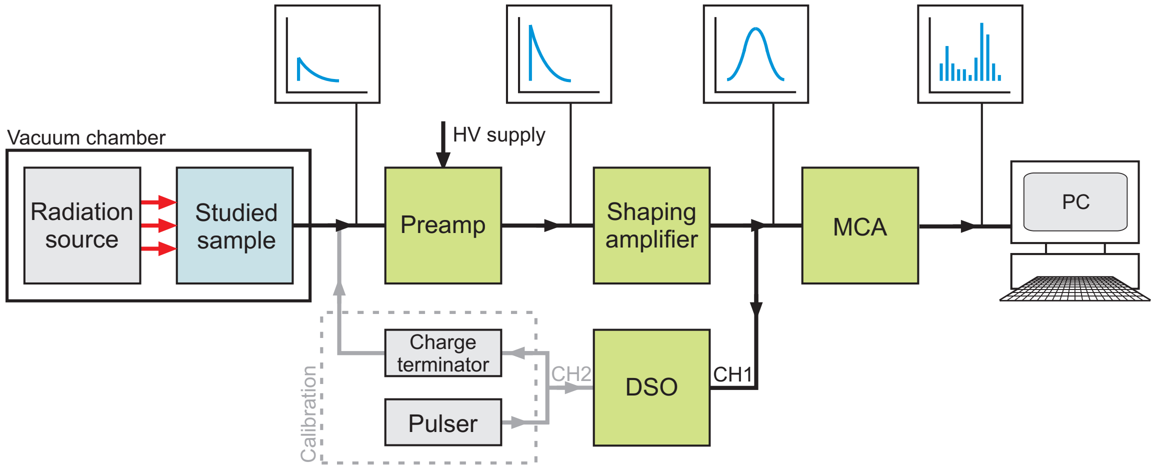

Figure I.3.2: Experimental arrangement for CCE measurements.

3.2.1 Pulser calibration

The most reliable method of performing a calibration is to use a charge terminator (CHT), i.e., a special capacitor of known capacitance in a shielding metal housing. CHT is placed between the pulser and the preamplifier input in place of the detector. In Fig. I.3.2 instruments and cabling for this type of calibration are in grey color and marked by a dashed rectangle. The calibration proceeds in following steps:

(i) The attenuated output from a precision pulser is connected to the CHT via one channel of the digital storage oscilloscope (DSO) (CH2 in Fig. I.3.2) with its termination set to 1 MΩ. This simulates pulses coming from a real detector. The output from the CHT is connected to the detector input of the preamplifier. Cables should be kept as short as possible.

(ii) The output of the shaping amplifier is connected to the second channel of the DSO (CH1 in Fig. I.3.2), the trigger of which is set to this channel. Averaging is enabled to improve noise on very small pulser signals. This ensures that both the sourcing and processed pulses are triggered and displayed clearly by adjusting the trigger level.

(iii) Pulse height spectra on MCA are acquired for several different pulser signals. The amplitudes are chosen so as to cover the whole MCA channel range. For each amplitude, the peak-to-peak height of the pulser signal (in millivolts), V_p, is measured on CH2 of the DSO and the corresponding MCA peak centroid[7] (in channel numbers), is measured on CH1.

Then, the energy of each pulse, $\mathcal{E}_p$, is calculated from the capacitance of the CHT, C_p:

$$\mathcal{E}_p \text{ (keV)} = \frac{\epsilon V_p C_p}{1.602 \times 10^{-19} \text{ C}} = 6.242 \times V_p \text{ (mV)} \times C_p \text{ (pF)} \times \epsilon \text{ (eV)}, \qquad \text{(I.3.1)}$$

where the electron–hole pair production energy, ϵ, for CdTe/CZT is to be found in Table 0.3.1. Consequently, one is able to find the dependence between channel numbers

---

[7] The channel number corresponding to the maximum of the peak in the pulse height spectrum. Usually, this quantity is fitted from the measured data using a gaussian fit.

measured on MCA and the energy, $\mathcal{E}$, corresponding to a charge collected by a studied detector. Usually, such a dependence is considered to be linear in full MCA channel range:

$$\mathcal{E}\ (\text{keV}) \ = \ m \ \times \ \text{channel number} \ + \ p, \tag{I.3.2}$$

where the constants m and p are determined from the linear fit. Finally, Eq. (I.2.18) can be rewritten in the form

$$CCE = \frac{\mathcal{E}}{\mathcal{E}_0} \tag{I.3.3}$$

with $\mathcal{E}_0 = 5490$ keV for α-particles from ^{241}Am source and $\mathcal{E}$ calculated from Eq. (I.3.2), enabling direct evaluation of CCE from the measured peak centroid.

3.2.2 Calibration using a silicon detector

As an additional check to the pulser calibration, the studied detector can be replaced by a precharacterised silicon detector while keeping all other electronics and readout system the same. Then, using various radiation sources that produce radiation/particles in the desired energy range, each recorded pulse height spectrum provides one additional point to the calibration line according to Eq. (I.3.2). The data points obtained by this procedure should lie on the line of the pulser calibration with calculated m and p.

The above calibration is valid for particular settings of the experiment and should be renewed every time anything is changed, e.g., shaping time or shaping type (gaussian, triangular) of a shaped pulse, MCA channel range, etc.

3.2.3 Rough estimate of $\mu\tau$

Except for the exact methods of calculation of CCE described in two previous sections, one can sometimes skip the time-consuming calibration of the experimental setup to quickly obtain an estimate of CCE on a set of detectors where the precise value of $\mu\tau$ is not required on behalf of mutual comparison of quality of several detectors. In such a situation, “CCE” can be measured directly in channel numbers (peak centroids corresponding to a particular photopeak) rather than normalizing this value to the channel corresponding to the energy $\mathcal{E}_0$ of used radiation source. For the evaluation of $\mu\tau$, an additional fitting parameter, C_0, must then be introduced to the chosen model. E.g., for the calculation utilizing the Hecht equation, Eq. (I.2.20), the fitting formula reads

$$CCE^{'}_{\text{Hecht}}(U) = C_0 \frac{\mu\tau U}{L^2}\left(1 - e^{-\frac{L^2}{\mu\tau U}}\right),$$

where the prime symbol was used to distinguish this equation from the original dimensionless Eq. (I.2.20). C_0 now represents the channel corresponding to the maximum collected charge. Though this value is not interesting while proceeding with this simplified procedure, it should be close to the channel number calculated from Eq. (I.3.2) for $\mathcal{E} = \mathcal{E}_0$ if the calibration were known.

3.3 Transient-current technique

TCT measurements were performed in the experimental setup schematically shown in Fig. I.3.3, the detail is depicted in Fig. I.3.4. The arrangement originates from the setup

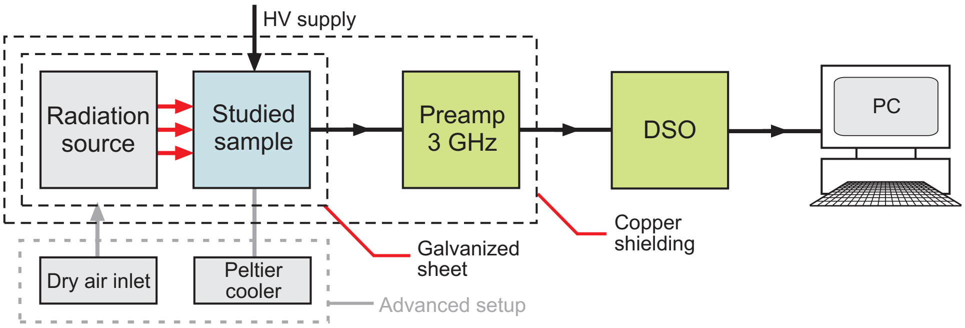

Figure I.3.3: Experimental arrangement for TCT measurements.

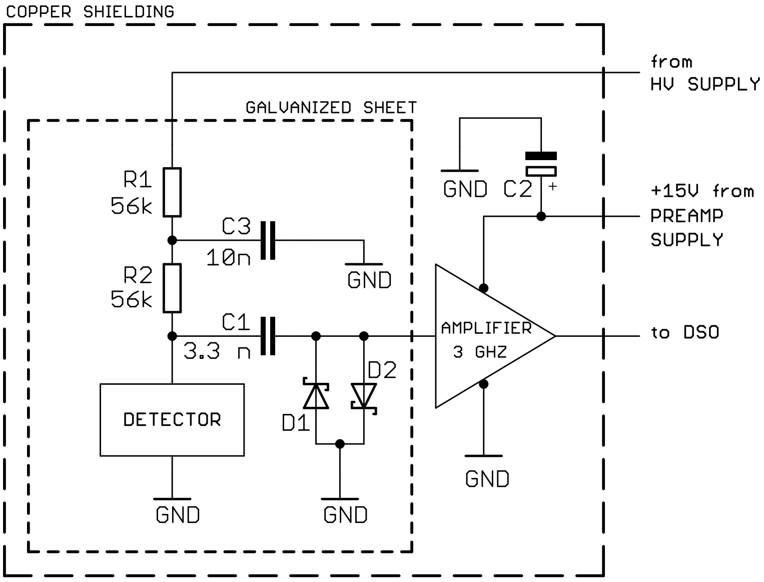

Figure I.3.4: Detailed view of the TCT experiment. All electronic parts including the current-sensitive preamplifier are placed inside a shielding box to protect them from disturbing electromagnetic interference.

presented in [33], however, several improvements were introduced to make it most suitable for measurements carried out in our laboratory.

CdTe/CZT samples are graphite-bonded onto a prefabricated PCB holder as described in Subsection 3.1.2, which is then placed inside a metal shielding box (galvanized sheet), and biased by an Iseg SHQ 122M high-voltage supply. Samples are irradiated in air by a 5.5 MeV ^{241}Am α-particle source at a distance of 3–5 mm. Because of lack of vacuum conditions in our TCT setup, the limited range of α-particles in air causes their energy loss. It was examined that this energy loss of approximately 0.5 MeV measured using a conventional charge-sensitive preamplifier corresponds well to values measured in [48]. As the signal-to-noise ratio of the TCT signal is sufficient, the lower energy of incident particles due to ionization losses does not affect calculated field slope since it is the transient damping parameter rather than height of the transient that is significant for calculations.

Carriers generated in the detector bulk are collected by the applied bias and a current signal, induced on the electrodes due to drift of carriers throughout the sample, is amplified by a 3 GHz Miteq AM-1607-3000R amplifier. Preamplifier supply voltage of +15 V is stabilized by a blocking tantalum capacitor C2; a ferrite bead around the supply cable reduces the effects of electromagnetic interference. Two anti-parallel Schottky diodes D1, D2 (type 1N5711) were placed at the input of the preamplifier to protect it from large pulses that occur accidentally and could damage the input stage. It was proven that these diodes do not distort the signal. Values of other electronic components were not modified with respect to original values [33] and are figured in detail in Fig. I.3.4. The effect of different choice of values of these components on a current transient is discussed in Subsection 4.1.3.

Current signal is converted into a voltage pulse on a precise 50 Ω termination resistor at the input of either a 350 MHz LeCroy WaveSurfer 434 DSO or a 4 GHz LeCroy WaveRunner 640 Zi DSO. As it is clear from Eq. (I.2.12) that the damping parameter c of measured transient can be extracted without the need for estimation of a pulse height (amplitude), there are situations where the knowledge of the "absolute" transient height is necessary (e.g., the evaluation of plasma erosion time according to Section 2.7 or estimation of CCE from a current transient). In this case, one need to know the gain of the preamplifier, G. The current I is then calculated from the voltage U using the formula

$$I\ (\mu\mathrm{A}) = \frac{10^3}{50\ \Omega \times G} \times U\ (\mathrm{mV}) = \frac{U\ (\mathrm{mV})}{\mathcal{Z}}, \tag{I.3.4}$$

where 50 Ω in the denominator is the input impedance of the DSO. On the right-hand side of the latter equation, $\mathcal{Z}$ is the overall voltage-to-current conversion factor, in literature [33] referred to as the transimpedance. For $G = 130$ estimated in our early TCT experiments $\mathcal{Z} = 6.5\ \mathrm{mV}/\mu\mathrm{A}$.

All electronic components as well as the current-sensitive preamplifier are placed within a copper shielding box while keeping the cable length of signal path as short as possible. Shielded coaxial cables were used. Double shielding (galvanized sheet and copper box) approved to be necessary to protect the electronic parts from electromagnetic interference (EMI) while simultaneously increasing the signal-to-noise ratio. Careful shielding together with the introduction of a 4 GHz DSO instead of former one with a bandwidth of 350 MHz made it possible to increase the sensitivity of the method and, on particular detectors, to extend the lower limit of measurable signal down to only several tens of volts applied on a detector. Moreover, short transients of thin samples as well as fast rising edges, theoretically down to 1/(4 GHz) = 0.25 ns, could be easily measured due to extended bandwidth of the DSO.

Sample capacitance, estimated to be in the order of several picofarads,[8] i.e., three orders-of-magnitude lower than the capacitance of the coupling capacitor C1 = 3.3 nF, is insufficient to affect the measurement. To avoid the distortion of the current transients by electronic artifacts inadvertently triggering the DSO (e.g., short pulses of a few nanoseconds probably arising from the preamplifier feedback or mobile-phone-induced EMI), advanced triggering options of the DSO together with computer-aided signal acquisition were adopted.

Advanced TCT setup incorporated also the Peltier cooler to stabilize the sample temperature during measurements to 295 K. In that case, marked in Fig. I.3.3 by a grey rectangle, temperature variations did not exceed 1 K. To prevent water vapour from air condensating on the detector and electronics within the shielding box when lowering the

---

[8] Typical dimensions of studied samples are $5 \times 5\ \mathrm{mm}^2$ of faces area and 1.5 mm in thickness, which with the relative dielectric constant of 10.3 yields the capacitance of 1.5 pF.

temperature down to 0 °C, the box is equipped with dry air/water-free gas inlet for purging the cooled chamber. However, there are no measurements of temperature dependence of electric field profile presented within this thesis.

An additional note concerning the excitation source used in TCT experiment is worth mentioning. In contrast to the setup implemented in the laboratory of IoP CU where α-particles are used to generate electron–hole pairs within the detector bulk, at Hokkaido Institute of Technology a nitrogen laser (λ = 337 nm) running at a repetition rate of 8 Hz is used as the excitation source [34]. Incorporation of the above bandgap radiation ensures high absorption coefficient of laser light in CdTe, implying the charge carriers being generated near the surface of the irradiated electrodes. Similarly to TCT, this so called *time-of-flight (TOF) measurement* enables one to calculate the electric field profile in a studied sample from current waveforms recorded by a DSO. As the diameter of the laser beam can be suitably adjusted to be comparable to sample dimensions, concentration of generated carriers—though their number can be several orders-of-magnitude higher than in the case of TCT—is less as compared to the carrier concentration in the charge cloud in the case of α-irradiation. This successfully removes the problem with the plasma effect deteriorating rising edges of current transients. However, in contrast to TCT where maximum energy of an α-particle is absorbed at finite distance of ~10–20 μm from sample surface (because of Bragg curve, see Fig. 0.2.3b), photons interact differently with the matter (see Section 2) and electron–hole pairs are generated with the highest rate at the surface of the sample and then the rate exponentially decreases towards the bulk. Therefore, the surface recombination must be taken into account in TOF calculations, which makes them more complex than TCT ones. Additionally, experimental setup involving a laser source is more complicated than the simple arrangement presented in Section 3.3.

4. Results and Discussion

Since the penetration depth of α-particles in CdTe is of the order of tens of micrometers, electron–hole pairs are generated close to the irradiated electrode. By changing the polarity of the applied bias, this feature allows to study either electron or hole signal using the theoretical results of Chapter 2. As the hole mobility is much lower than that of electrons, the hole-induced signal is weak. It would require the use of a second amplifier connected to the output of the amplifier in Fig. I.3.3 to sufficiently increase the signal to provide a satisfactory signal-to-noise ratio. Only the electron-induced measurements (detector irradiated from the cathode side) are presented in this chapter.

4.1 Basic demonstration of TCT

Before proceeding with deeper study of TCT which resulted in the development of SCP and DMP procedures, the reader is introduced to the basics of TCT analysis though the study of typical current waveforms representing the detector response to α-irradiation. Most of this results were published in [25]. For now, iterative treatment is neglected.

4.1.1 Calculation of mobility, space-charge density, and depletion width

Bias dependence of current pulses measured on BNL2E9, B39KB3, and AC31C1 detectors are, respectively, shown in Figs. I.4.1a, I.4.2a, and I.4.3a. These detectors were fabricated by a common process described in Section 3.1; Table I.4.1 summarizes same of their properties interesting for this analysis. To lower the noise of input data, all measurements were integrated over 500 events during the acquisition on LeCroy WaveSurfer 434 DSO. No time evolution of the current waveforms was observed, i.e., all waveforms were proven to remain in a steady state during measurements. Thus, any probable charging of the detector bulk (polarization) must have occurred just after applying the bias on the detector. Time resolved measurements of such detector polarization on a scale of several seconds after biasing were not available since it takes time of approximately 1 minute to safely bias the detector and set up the DSO.[9]

In all detectors the maximum of current signal appeared shortly after triggering the pulse. The pulse rise time was several nanoseconds long and shortened with increasing bias. The rise time of current transients in AC31C1 (Fig. I.4.3a) was very short. Estimated values of about 3 ns represent the oscilloscope limit given by its bandwidth of 350 MHz. Shorter waveforms could not be recorded correctly.[10] The fast rising edge of the pulse followed by the "dib" at $t \approx 5$ ns, which was seemingly bias-independent, was likely to be a triggering effect or the result of signal back-scattering in cables.

It is the characteristics of TCT that the current waveform of a charge carrier drifting in a decreasing electric field decreases (as shown in Chapter 2 the decrease is exponential if the field profile is linear) and breaks at the time when the forefront of the carrier "cloud" reaches the opposite electrode ($t = t_{tr}$, Eq. (I.2.15)), which is evidenced as a "break"

---

[9] Detectors are biased either in a linear staircase sweep regime with 1 or 2 steps of several volts per second through a computer program or manually by increasing bias from zero to the desired value to prevent the preamplifier from being damaged by applying high voltage at one moment.

[10] A 4 GHz oscilloscope WaveRunner 640 Zi was not available at the time of these measurements.

Table I.4.1: Sample properties

Sample	Material	Contacts	Thickness L (mm)	$\mu\tau$ (cm^2/V)	μ (cm^2/Vs)
BNL2E9	$Cd_{0.85}Zn_{0.15}Te$	Au/Au	1.1	2×10^{-3}	979†
B39KB3	CdTe:In	Au/Au	1.7	2×10^{-4}	918†
AC31C1	CdTe:Cl	Au/Au	1.8	3×10^{-4}	900§

§ From rise time of a charge signal via charge-sensitive preamplifier.

† From TCT measurements via current-sensitive preamplifier.

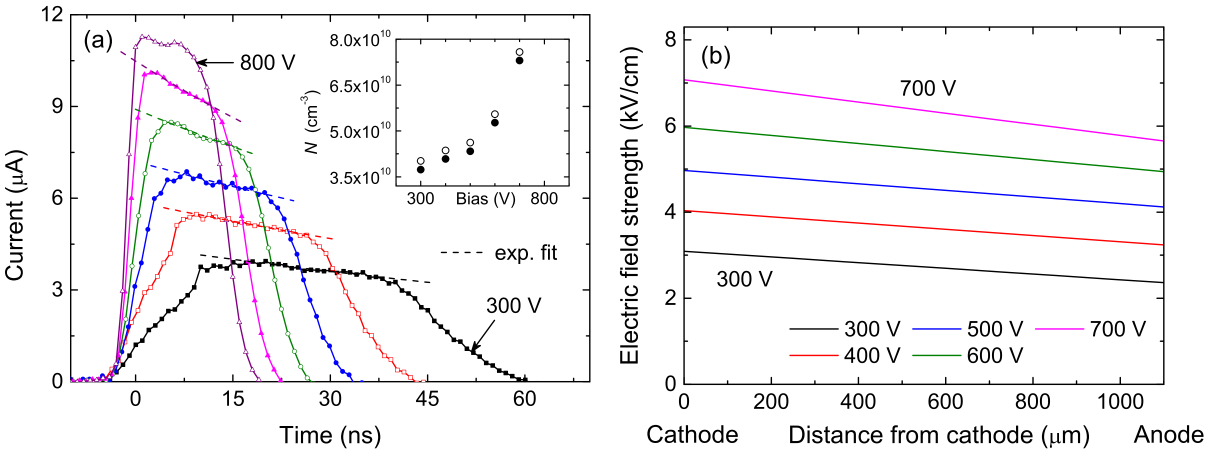

Figure I.4.1: (a) Current transients in BNL2E9 recorded for different applied biases. The inset shows the bias dependence of the space-charge density N both considering trapping (solid symbols) and neglecting it (open symbols). (b) Calculated strength of the electric field in BNL2E9 detector as a function of the distance from cathode for different applied biases.

(a "shoulder") in the current pulse (a transition between exponential part and a trailing edge). This situation is recognized readily in Figs. I.4.1a and I.4.2a, but does not pertain to Fig. I.4.3a. With increasing bias the pulses shrink and their transit times t_{tr} decrease since it then takes less time for electrons to drift through the sample.

Fitting the experimental data according to Eq. (I.2.12) brings the values of parameter c. Since the estimation of t_{tr} is easy and can be done directly from Figs. I.4.1a and I.4.2a, the electron mobility, μ, is obtained by solving Eq. (I.2.17) with upper signs using values of $\mu\tau$ and L shown in Table I.4.1. Values of $\mu\tau$ products were determined from measured CCE spectra via the Hecht equation. For precise calculations of $\mu\tau$ in the case of inhomogeneous electric field (but still based on CCE measurements only, i.e., without any further information from TCT or Pockels measurements), the advanced approaches can be used [49, 50]. For precise calculations utilizing TCT measurements, iterative procedures are necessary. This will be discussed later in a separate section.

For different biases the calculated electron mobilities according to Eq. (I.2.13) are slightly different. The average values are $\mu = (979 \pm 19)$ cm^2/Vs and $\mu = (918 \pm 11)$ cm^2/Vs, respectively, for BNL2E9 and B39KB3. Low statistical uncertainty proves

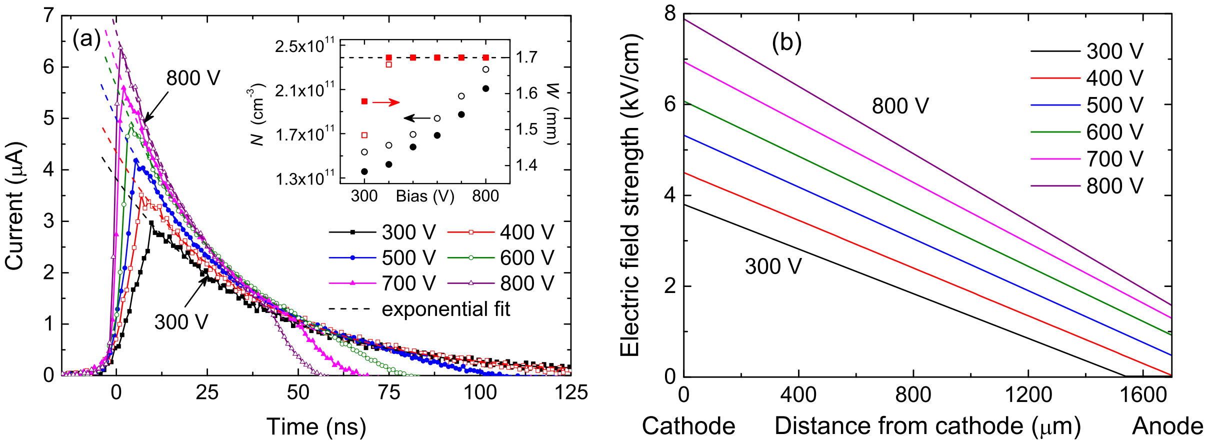

Figure I.4.2: (a) Current transients in B39KB3 recorded for different applied biases. The inset shows the bias dependence of the space-charge density N and the corresponding values of the depletion width W calculated from Eq. (I.2.4) both considering trapping (solid symbols) and neglecting it (open symbols). Dashed line in the inset marks the thickness of the detector (1.7 mm). (b) Calculated strength of the electric field in B39KB3 detector as a function of the distance from cathode for different applied bias voltages.

that the mobility can be considered field-independent. It is worth noting that commonly used formula $\mu = L^2/(t_{tr}U)$ (Eq. (I.2.16)) cannot be utilized here as it is valid only for a uniform electric field. If used, the mobility of B39KB3 neglecting the field profile would be estimated to be as low as 723 cm^2/Vs. The mobility of AC31C1 could not be evaluated by TCT as there was no apparent break in recorded current transients, see Fig. I.4.3a. For further calculations the value of $\mu = 900$ cm^2/Vs, determined via a charge-sensitive preamplifier from measurements of the rise time of a charge signal induced by α-particles irradiating the detector [51], is used.

The exponential decrease in current signal after the initial rise-up can be explained in terms of a positive space charge within the detector. Having determined the values of parameter c, the slope a of the electric field is calculated from Eq. (I.2.13); furthermore, the space-charge density and depletion width can be estimated using Eqs. (I.2.4) and (I.2.8). A space-charge density of the order of 10^{10} cm^{-3} was found for BNL2E9 and 10^{11}–10^{12} cm^{-3} for B39KB3 and AC31C1, varying with applied bias in all detectors. These values agree with observations of several authors [30, 31, 34, 52]. For BNL2E9 and B39KB3 the space-charge density rises with increasing bias. The bias dependencies are plotted in the insets of Figs. I.4.1a, I.4.2a, and I.4.3a both considering trapping and neglecting it ($\tau \to \infty$). The trapping times were calculated from the values of $\mu\tau$ and the estimated values of μ, giving $\tau = 2$ μs, 220 ns, and 330 ns for BNL2E9, B39KB3, and AC31C1, respectively. It is clear that trapping has the largest effect on B39KB3 transients, for which there may be a difference as high as 13% between the value calculated in the absence of trapping and that evaluated when trapping is considered. For BNL2E9 and AC31C1, respectively, this difference does not exceed 7% and 3%. Though all studied samples have gold contacts, which are typically characterized as ohmic, the positive charging of the detector bulk implies that band bending at the contacts occurs, forming electron-blocking cathode and hole-injecting anode.

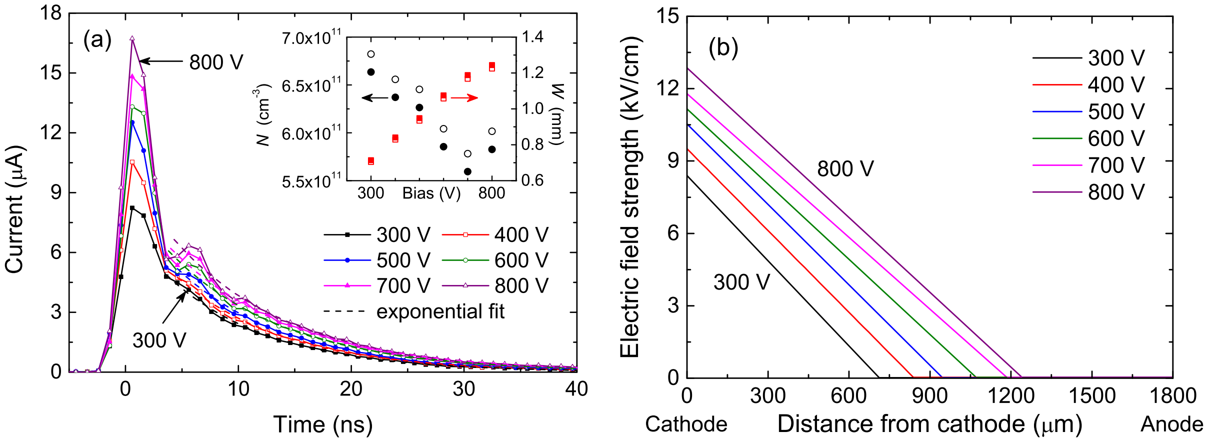

Figure I.4.3: (a) Current transients in AC31C1 recorded for different applied biases. The inset shows the bias dependence of the space-charge density N and the corresponding values of the depletion width W calculated from Eq. (I.2.4) both considering trapping (solid symbols) and neglecting it (open symbols). (b) Calculated strength of the electric field in AC31C1 detector as a function of the distance from cathode for different applied bias voltages.

4.1.2 Calculation of electric field profile

The profiles of the electric field of BNL2E9 and B39KB3 detectors were calculated from parameters a and E_0 determined from the analysis of the current transients. The results are shown in Figs. I.4.1b and I.4.2b. The absence of transient breaks in Fig. I.4.3b does not allow to directly evaluate the electric field in AC31C1 since the transit time is undefined in this case even for high biases. Nevertheless, since the electron mobility of 900 cm^2/Vs was determined from the rise time of charge signal measured with the help of a charge-sensitive preamplifier, the electric field could still be calculated, yielding the profile depicted in Fig. I.4.3b. The electric fields of all detectors show maxima at the cathode and then linearly decrease towards the anode. Such behaviour is consistent with the positive charging of studied samples as already outlined above.

With increasing bias the evaluated space-charge density increases in BNL2E9 and B39KB3, but slightly decreases in AC31C1. The reason for this difference could originate from larger E_0 for strongly polarized AC31C1 and reduction of the Schottky barrier at the cathode due to the Schottky effect [40]. Conversely, the increasing N in BNL2E9 and B39KB3 results from enhanced electron depletion and hole injection with rising bias.

As discussed above the space-charge density is one order-of-magnitude less in BNL2E9 than in B39KB9 and the entire volume of the detector is depleted even at a minimum bias of 300 V (see Fig. I.4.1). In contrast to B39KB3, Fig. I.4.1b demonstrates that the strength of the electric field in BNL2E9 is nearly constant. Average values of the field strength agree well with the theoretical field strengths, $E^{(\text{theor})}$, calculated under the assumption of a homogeneous field throughout the sample. Moreover, using the formula $E^{(\text{theor})} = U/L$, for, e.g., 300 V the value $E^{(\text{theor})} = 2.7$ kV/cm is obtained, while $E_0 = 3.1$ kV/cm is the field strength under the cathode at 300 V. The missing profile for 800 V reflects the large uncertainty of the exponential fit in Fig. I.4.1a.

For biases larger than 500 V, a break in the current pulses recorded on B39KB3 becomes clearly visible, see Fig. I.4.2b. For lower biases the break vanishes since an inactive region with zero electric field appears under the anode and hence one could not evaluate the transit time. It should be noted that the formation of the inactive region is confirmed independently both by the disappearance of the break in current waveforms and by the fits of the transients' damped parts according to Eq. (I.2.12), which are purely exponential below 500 V. The presence of an inactive region then seriously limits the detector spectroscopic performance. It is illustrated with the help of Eq. (I.2.4) and the inset in Fig. I.4.2a that the depletion layer can extend to the entire volume of the detector by increasing bias voltage. For measurements carried out at 300 V and 400 V, the depletion width W is less than the detector thickness. Therefore, generated charge is not collected by the whole volume of the detector. As the bias is increased above 500 V, the calculated values of W reach the value of detector thickness and its total volume becomes active. For higher bias voltages the detector is already operating under complete depletion.

The excellent applicability of the theoretical model to experimental data proves the correctness of the assumption of a constant space-charge density (and thus a linear electric field) in studied samples.

4.1.3 Deeper analysis of current waveforms

It is apparent that rise times of the current waveforms of BNL2E9 and B39KB3 detectors are much longer than those of AC31C1. Such behaviour is attributed to the plasma effect, refer to Section 2.7. Around 10^6 electron–hole pairs are created along the path of an α-particle in the detector (10–20 μm because of low range of α-particles in matter), thereby forming a charge cloud. These carriers are subject to electric field in a detector. To roughly describe their motion, an estimate of the distance l_{diff} (l_{drift}) that carriers travel by diffusion (drift) in $\Delta t = 14$ ns, which is the rise time for the 300 V current waveform in Fig. I.4.1a, is calculated at first. For diffusion one obtains $l_{\text{diff}} = \sqrt{\mu k_B T \Delta t / e} \approx 6$ μm at room temperature $T = 300$ K, whereas for drift $l_{\text{drift}} = \mu U \Delta t / L \approx 380$ μm, if k_B is the Boltzmann constant. As $l_{\text{drift}} \gg l_{\text{diff}}$, drift dominates over diffusion in a direction perpendicular to the detector contacts. Therefore, it is the electric field in a sample rather than diffusion that is responsible for the initial acceleration of carriers and the erosion of the charge cloud.

The screening of externally applied bias within the charge cloud can be estimated in the following way: the electric field $\overline{\mathcal{E}}$ created by 10^6 electrons and holes in two parallel planes separated by 10 μm from one another, i.e., approximately half the penetration depth of α-particles in CdTe, is calculated from the Coulomb's law, giving $\overline{\mathcal{E}} \approx 14$ kV/cm. As the electric field under the cathode of BNL2E9 for bias of 300 V is $E_0 \approx 3$ kV/cm (see Fig. I.4.1b) and since $\overline{\mathcal{E}} > E_0$, it is obvious that the plasma effect can be strong enough to delay signal formation and extend the transient rise time to observed values.

When the bias is increased the estimated value of $\overline{\mathcal{E}}$ remains valid, but the electric field E_0 increases. Thus, for higher bias voltages the plasma effect becomes less important and can be suppressed overall as clearly demonstrated in Figs. I.4.1a and I.4.2a by shortening of pulse rise times. The absence of the plasma effect in Fig. I.4.3a is easily explained after realizing that in the range of bias voltages applied on AC31C1, only about a half of the detector volume is depleted. Therefore, the electric field under the cathode is higher than in other two samples (compare Figs. I.4.1b, I.4.2b to Fig. I.4.3b) and current waveforms, even those at 300 V, are already unaffected by the plasma effect.

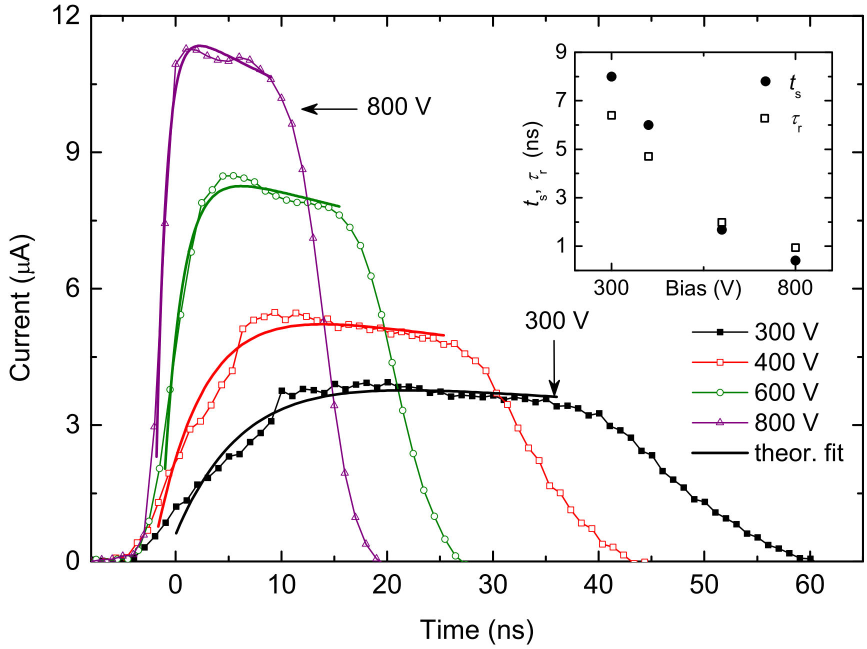

Figure I.4.4: Reconstruction of current waveforms measured in BNL2E9 detector according to the plasma-effect model in [33]. The inset shows the bias dependence of fitting parameters t_s and τ_r introduced in the model.

In [33] a simple model of the plasma effect was used to reconstruct the current waveforms $i(t)$:

$$\begin{aligned} i(t) &= Q_0 \left(1 - \mathrm{e}^{-t/\tau_r}\right) \frac{\mu}{L} \big((E_0 - a x(t)\big), && \text{(I.4.1)} \\ x(t) &= \left[\frac{E_0}{a} + \left(x_0 - \frac{E_0}{a}\right) \mathrm{e}^{-a\mu(t-t_s)}\right] \left(1 - \mathrm{e}^{-t/\tau_r}\right), && \text{(I.4.2)} \end{aligned}$$

where a and E_0 are the field slope and electric field strength under the cathode, x_0 is the absorption depth of α-particles in CdTe/CZT, and τ_r and t_s are parameters describing the plasma effect: $\tau_r \sim$ reduced signal charge and charge carrier velocity, and $t_s \sim$ delayed signal formation. Eqs. (I.4.1) and (I.4.2) were used to simulate the current pulses recorded in BNL2E9 detector, see Fig. I.4.4. It shows that the rising parts of the waveforms measured for higher bias voltages are reconstructed sufficiently; however, for low applied biases when the plasma effect most affects the carrier movement, the applicability of the model decreases.

The reconstruction of current transients according to phenomenological model presented in Section 2.7 was more successful than the application of Eqs. (I.4.1)–(I.4.2), see Fig. I.4.5. For the modelling procedure the data points from the beginning of the pulse to its maximum were considered for the analysis of the plasma effect, the data points from the exponentially decreasing (middle) part were used for the estimation of the field slope. The whole shape of the waveform including its trailing edge may then be unambiguously calculated according to Eq. (I.2.34). Both the rising edges and exponential parts of current waveforms for both low and high applied biases are modelled well; however, slight differences appear on trailing edges of the waveforms. Since the model differs from the experimental data more at low biases for which the transients are much shorter than at higher bias, fast rising edges of short waveforms might be affected by the electronics. This

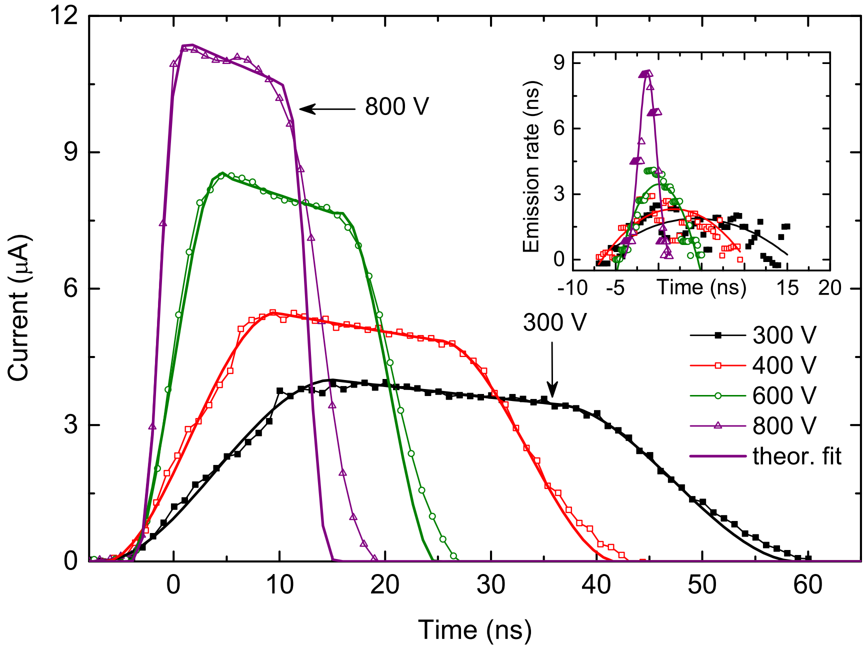

Figure I.4.5: Reconstruction of current waveforms measured in BNL2E9 detector according to phenomenological model presented in Section 2.7. The inset shows calculated emission rates for different bias voltages (symbols show experimental data, lines mark parabolic/Gaussian interpolation of those).

distortion is, however, unintentionally involved into calculation as the whole rising edge is processed to obtain the carrier emission rate $n(t)$. Thus the calculated rates depicted in the inset of Fig. I.4.5, specially at 800 V and 600 V, need not to be an actual feature of the detector but the combined result of the plasma effect and the electronic distortion. To dispose of this problem correctly, a response function of the electronic circuit should be considered. Nevertheless, these calculation are not included in this thesis, but should be a challenge for future work.

In the inset of Fig. I.4.5 the calculated emission rates of charge carriers from the plasma cloud are shown. Though the data are quite noisy, the analysis reveals that the emission rate rises from zero to its maximum and then decreases again toward the zero; the maximum emission is identified with the inflection point in the transient rising edge. In all four current waveforms analyzed in Fig. I.4.5, the emission rate can be approximated by a parabolic or Gaussian function shown by solid curve in the inset.

Although this model can be successfully applied to the data measured on B39KB3 and AC31C1 detectors as well, its predictions around the trailing edges (for $t > t_{tr}$) deviate from experimental data. There might be, away from the distortion of fast edges due to electronics, another reason for this behaviour. The plasma effect is not only responsible for the long rise times of current waveforms for low bias voltages, but it also prolongs the pulse trailing edges. It follows directly from the general theory presented in Section 2.7 that if no other effects but the delayed carrier emission were present, the transient rise and fall times would be equal. It is, however, not seen in Fig. I.4.5. E.g., for 300 V where the electronics distortion of the rising edge is believed to be negligible, the electrons that start drifting close to the cathode at $t \approx -5$ ns reach the anode at $t \approx 40$ ns. The signal is completely built at $t \approx 10$ ns, signalizing that even the most delayed electrons are already in motion (thus $t_p \approx 15$ ns). The last of them should arrive at the anode at $t \approx 15$ ns

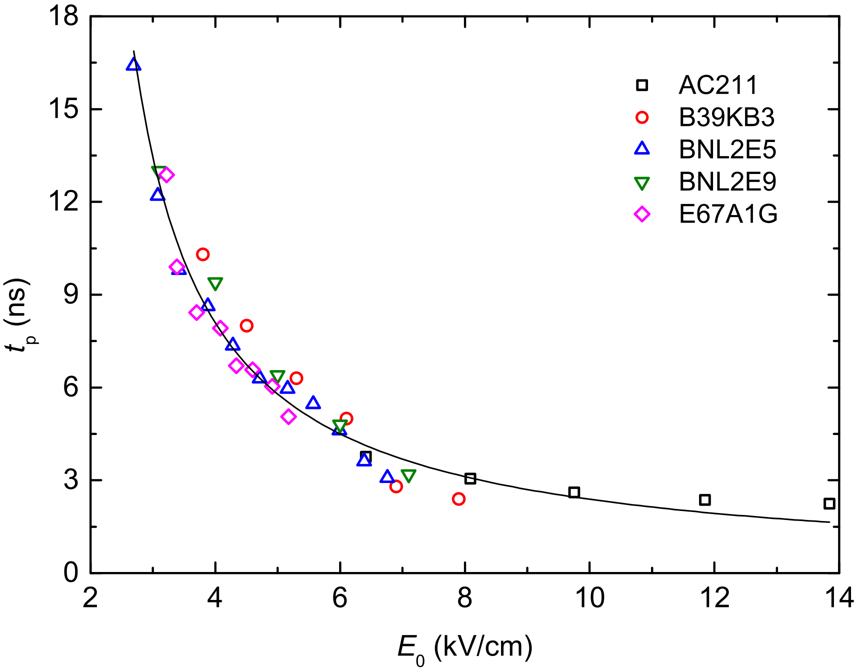

Figure I.4.6: Plasma erosion time t_p of BNL2E9, B39KB3, and several other CdTe/CZT detectors as a function of the electric field E_C under the cathode. Following [46] the solid line shows the inversely proportional fit of the experimental data to E_C.

+ 40 ns = 55 ns and the pulse should come to an end. In reality, the pulse terminates not until $t \approx 60$ ns, implying that the pulse fall time is approximately 5 ns slower. One can follow the same analysis of waveforms recorded for different biases. If the difference Δt between the pulse fall time and rise time were bias-independent, the observed effect could be assigned to the detrapping of carriers. On the contrary, if the difference decreased with increasing bias, inhomogeneities in the sample would be responsible. Such an analysis had been tried on BNL2E9 and B39KB3 samples but no unambiguous relation between Δt and the applied bias was found. The reason for the slower fall time of recorded waveforms thus cannot be recognized readily. This result once again pointed out on the possible effect of the electronics on the shape of a current transient. Consequent preliminary experiments with different values of circuit components at the input of the Miteq AM-1607 preamplifier, i.e., capacitance of C1 and resistances of R1 and R2 (see Fig. I.3.4), showed up that component values affect the difference Δt. Fine-tuning of the most-suitable values of these components was not performed, however, it would be an interesting topic for a separate study. Although the shape of a current transient can be slightly modified by a different choice of values of C1, R1, and R2, corresponding changes are small and important only for a deeper analysis of the transient. The effect on quantities important for the reconstruction of field profiles, i.e., c and t_{tr}, is negligible and within the error of calculations.

Additionally, a short comment concerning the field reconstruction process is provided. The electric field profiles are calculated from parameters a and E_0 determined from fits of the exponential parts of current transients instead of performing a direct "transformation" of current waveforms into profiles of the electric field according to [33]. Consequently, distortion of calculated field profiles under the contact due to the plasma effect is removed, as explained in Section 2.7 and clearly demonstrated in Figs. I.4.1b–I.4.3b.

The decreasing impact of the plasma effect on current transients with increasing bias can be demonstrated by the relationship between the plasma erosion time t_p and electric field E_C under the cathode (Eq. (I.2.5)). In [46] t_p is defined as the time needed to bring all carriers under the influence of the applied bias. If one identifies t_p with 10–90% rise time of current transients, the dependence of t_p on E_C can be plotted as seen in Fig. I.4.6 for several detectors. Though t_p should approach zero for large electric fields, values lower than 2–3 ns cannot be observed because of limited bandwidth of the DSO. As values representing measurements on different materials follow the same curve, one can deduce that for CdTe/CZT detectors—under the experimental setup described in Chapter 3—the plasma effect depends on the electric field under the irradiated electrode rather than on the material being irradiated. This finding can be used for quick estimation of the strength of the electric field under the contact just by a comparison of t_p measured on a studied sample with those in Fig. I.4.6. For different source–detector distance the energy of the incident α-particles should be evaluated using published stopping powers [48] at first. Then, assuming that t_p scales with the cube root of the energy of the incident α-particles [46], the data in Fig. I.4.6 could be recalculated to allow a new estimation of t_p. The dependence $t_p(E_C)$ determined experimentally is completed in Fig. I.4.6 by the fit $t_p \propto 1/E_C$ proposed in [46]. The fit describes the data relatively well although the drawbacks of the fit are apparent. Thus, improving the theory of plasma erosion, implying a refined relation for $t_p(E_C)$, is advisable.

4.2 Advanced TCT techniques: Iterative procedures

In the previous section the fundamentals of TCT technique have been demonstrated. In this section the advanced iterative procedures introduced in Section 2.4 are applied on real experimental data acquired on CdTe and CZT detectors. It is extensively illustrated that these procedures represent the state-of-the-art of TCT calculations in comparison to other simple methods commonly used.

To demonstrate the applicability of SCP and DMP methods for the evaluation of $\mu\tau$ on real experimental data, the same analysis as earlier performed in Section 2.5 on artificial D1, D2, and D3 detectors was carried out on the measurements acquired on three CdTe and CZT planar detectors, see Table I.4.2. These detectors were fabricated by a common process described in Section 3.1. Only the electron signal was used, i.e., samples were irradiated from the cathode side. The collected α-particle spectra are shown in Fig. I.4.7. The decreasing height and FWHM of photopeaks in Fig. I.4.7c were the results of increasing tendency of E46D3I to polarize with increasing bias; the ongoing polarization after the biasing limited the analysis to 600 V and the collection of spectra to 10 seconds only. Different $\mu\tau$-products of detectors in Fig. I.4.7 are expectable because of diverse CCEs. First of all, measurements performed on E67A1C and B39KB3 are discussed. The results of Hecht and Matz approaches are depicted in Fig. I.4.8, those of SCP and DMP are presented in Fig. I.4.9. Summary is given in Table I.4.3.

In Fig. I.4.8 the curves representing the Hecht and Matz fits of the CCE of E67A1C are identical and match well with the measured data. While the Hecht analysis yields $\mu\tau = 1.72 \times 10^{-3}$ cm^2/V, the one according to Matz and Weidner brings either the same value as Hecht or $\mu\tau = 1.55 \times 10^{-3}$ cm^2/V, depending on the initial guess. Although it was not explicitly mentioned above, introducing a new parameter to the model (e.g., a_{eff} in the case of Matz) brings the necessity to provide an initial value of this parameter to start the fitting procedure. Any additional parameter increases the complexity of the

Table I.4.2: Sample properties

Sample	Material	Contacts	Dimensions[†] (mm × mm × mm)
E67A1C	$Cd_{0.9}Zn_{0.1}Te$:In	Au/Au	4.8 × 5.5 × 0.91
B39KB3	CdTe:In	Au/Au	4.6 × 4.6 × 1.65
E46D3I	$Cd_{0.96}Zn_{0.04}Te$	Au/Au	5.5 × 6.0 × 2.48

[†] Width × depth × thickness L

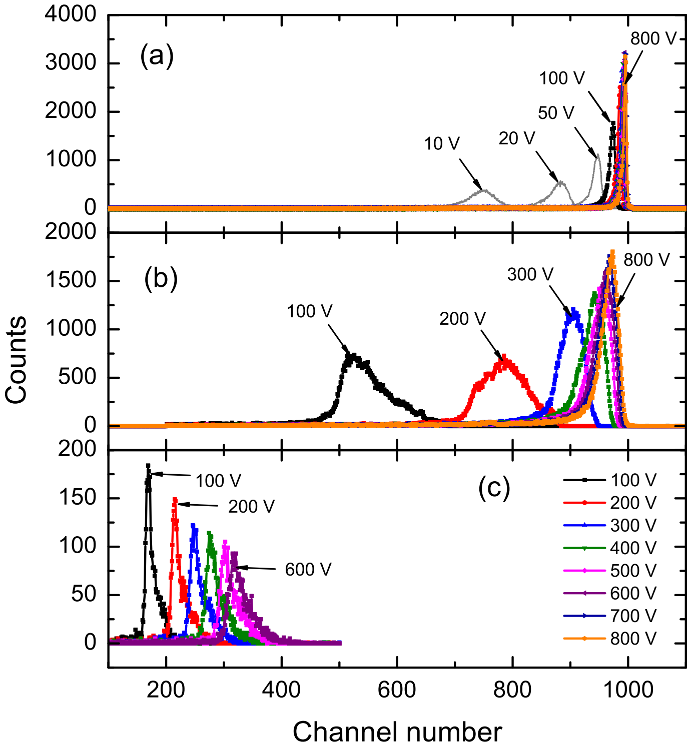

Figure I.4.7: ^{241}Am α-spectra taken by (a) E67A1C, (b) B39KB3, and (c) E46D3I detectors. Note the different scale of vertical axes, resulting from different collection times (300 seconds in (a) and (b), 10 seconds in (c) in order to prevent the recorded spectrum from being distorted by evolving polarization) and collection efficiency.

problem as it becomes multivariate. During the fitting the procedure may converge to different solutions depending on the initial guesses. Applied to our situation, the Matz fit converges to either the Hecht solution with no space charge within the detector ($a_{\text{eff}} = 0$), or to the solution $\mu\tau = 1.55 \times 10^{-3}$ cm^2/V with $a_{\text{eff}} = 4.9$ kV/cm^2. Both values of $\mu\tau$ are similar and one cannot decide which one is correct. Anyway, the polarization is small in either case.

However, in the case of SCP and DMP different results are obtained. Though the mobility–lifetime product is amended just a little, the slopes of the profiles of the electric field show major dependence on the applied bias and—for high biases—are much greater than a_{eff} yielded from Matz approach, see Fig. I.4.9a. At 800 V a reaches 100 kV/cm^2, which implies that the concentration of charge traps is as high as 6×10^{11} cm^{-3}. This information could not be obtained unless using the SCP or DMP methods.

In B39KB3 detector the Hecht equation does not describe the measured experimental data well. By contrast, they are excellently approximated using the Matz fitting procedure, yielding $\mu\tau = 0.66 \times 10^{-3}$ cm^2/V and $a_{\text{eff}} = 16$ kV/cm^2. These results are

Table I.4.3: Results of $\mu\tau$ calculations on real samples

Sample	$\mu\tau$ (10^{-3} cm^2/V)			
	Hecht	Matz	our approach	
			SCP	DMP
E67A1C	1.72	1.72/1.55	1.62	1.62
B39KB3	0.27	0.66	1.23	0.80
E46D3I	0.31	not available, μ only		

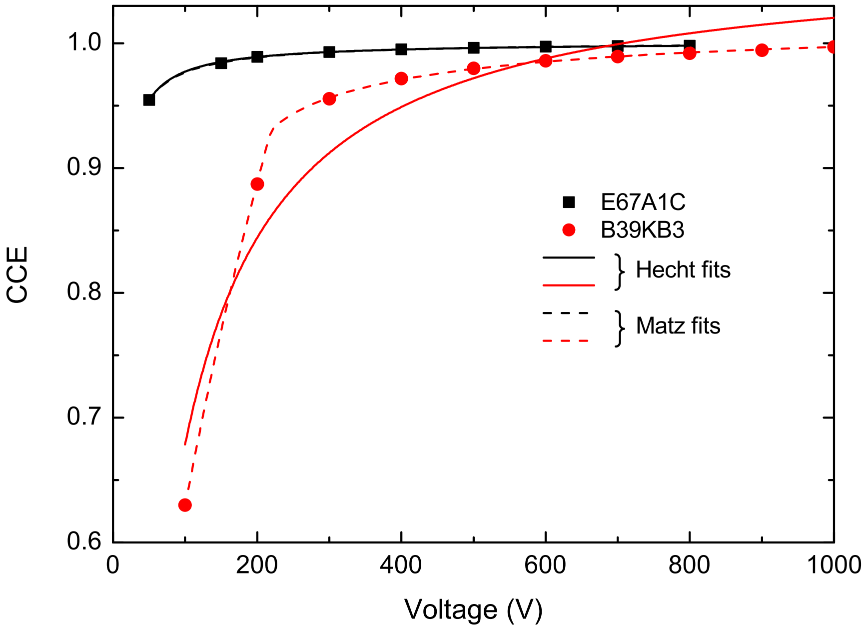

Figure I.4.8: Fits of measured CCEs of E67A1C and B39KB3 detectors. Solid lines show the fits according to the Hecht equation, dashed lines refer to the Matz fits. The Hecht equation fails to describe the data for B39KB3 well.

confirmed by utilizing both the SCP and DMP: the mobility–lifetime product is refined to 1.23×10^{-3} cm^2/V and 0.80×10^{-3} cm^2/V, while the field slopes are nearly constant with the average of 16.5 kV/cm^2. The discrepancy in obtained values of $\mu\tau$ is the direct consequence of the different computation routines (the reader is advised to compare the flow charts of these methods in Figs. I.2.4 and I.2.5); different treatments imply different results when convergence criterions are fulfilled.

Both iterative procedures provide more information about studied samples than the Hecht or Matz approaches. The SCP is easier to incorporate to user routines as it is simple and illustrative. On the other hand, DMP is more complex but it requires the numerical solution of a transcendental equation as part of the fitting procedure. As the requirement for the best match between the experimental data and theory is its prerequisite through the minimization of χ^2, it should be the preferred procedure to implement. Last but not least, the assumption of sample homogeneity has to be satisfied for these methods to give meaningful results. Several CCE and TCT measurements on E67A1C and B39KB3 detectors with a small orifice placed in between the sample and α-source have proven

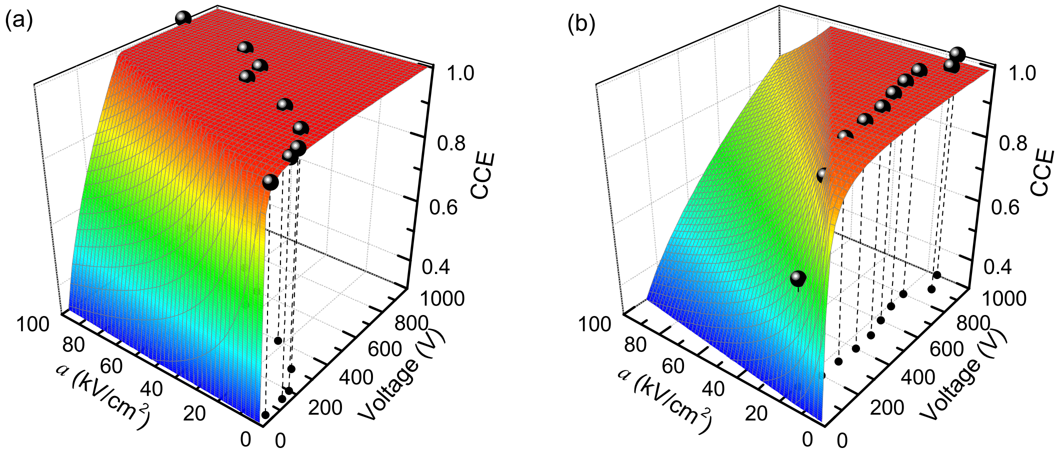

Figure I.4.9: Two-dimensional surface fits of CCEs of (a) E67A1C and (b) B39KB3 detectors calculated using DMP. Dashed lines show the projections of the three-dimensional data $[U, a_U, CCE_U]$ to the ground plane, where the bias dependence of the slope of the electric field profile can be found. TCT waveforms are not shown.

that such an assumption is valid as different parts of a particular sample, except for the locations near the edges, showed comparable charge collection.

Finally, the measurement performed on E46D3I detector is reported. During the measurements of CCE this detector proved to be strongly polarized because of low charge collection and weak TCT signal. In Table I.4.3 the value $\mu\tau = 0.31 \times 10^{-3}$ cm^2/V was shown as the result of the Hecht analysis; however, the result is likely to be distorted due to strong polarization. Supposing that $|a| \gg 1/\mu\tau$, Eq. (I.2.30) can be used to directly fit the CCE as a function of damping parameters c and applied bias U. If the assumption is correct, $CCE(c, U) \propto \sqrt{U/c}$ should be observed. This was indeed confirmed, see Fig. I.4.10.

Strongly-polarized detectors usually do not show a good charge collection. To calculate CCE correctly as a ratio of charge collected at a particular bias to the maximum collected charge, nearly saturated collection should be achieved, i.e., the bias must be increased until most of the generated charge is collected. In the case of E46D3I this would require the application of voltage far above a thousand of volts. It was observed that at higher bias the polarization of this sample evolves so quickly that it is impossible to measure the radiation spectrum in a (quasi-) steady-state for at least few seconds necessary for the determination of the peak centroid. Unfortunately, since the voltage must be applied in a sweep rather than by a step change in the present experimental setup, the measurements above 800 V could not be realized because the charge signal was already too weak before the sample was biased and prepared for measurement. Consequently, the MCA channel Q_m corresponding to the maximum collected charge could not be determined. This is why the “CCE” is plotted in channel numbers in Fig. I.4.10 rather than normalized to Q_m as usual.

From Subsection 2.4.3 it is known that $\mu\tau$ cannot be evaluated using Eq. (I.2.30); nevertheless, at least the carrier mobility, μ, can be obtained. Without the normalization the right-hand side of Eq. (I.2.30) must be multiplied by Q_m to fit the available measurements. Although Q_m could not be measured directly, it has been experienced that—for various another detectors—Q_m usually lies between channel numbers 1000 and 1200 in our setup,

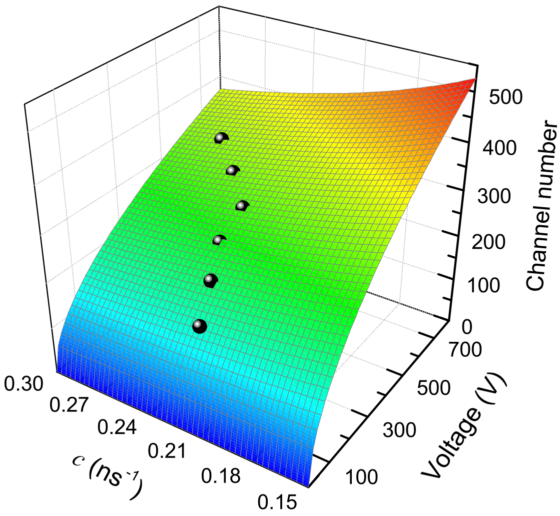

Figure I.4.10: “CCE” fit of the strongly-polarized detector E46D3I. Because of problems with the estimation of a channel number corresponding to the maximum collected charge, the vertical axis is plotted in channel numbers of a MCA instead of being normalized to 1. TCT waveforms are not shown.

yielding the electron mobility between 1600 and 1100 cm^2/Vs in E46D3I. Though it is just an estimate, the mobility is good regardless of high polarization.

4.3 Application example: Effect of contacts on electric field

Since both the basic and advanced concepts of utilizing TCT method for the calculation of electric field profiles were already extensively discussed in previous sections, the attention is now focused on an exemplary application.

In addition to the need for high crystalline quality of the detector bulk material, the electrical contacts can also crucially affect the device performance. To assure that a detector performs the best in its applications, the choice of material for contacts and sometimes method of deposition must be taken into account. It is generally accepted that ohmic contacts effectively suppress polarization, while Schottky contacts enhance it [37, 53]. In this section the TCT measurements taken on both ohmic- and Schottky-type CZT detectors are presented. It is argued that the proper choice of metals for detector contacts helps to reduce problems with polarization and that experimental results reported here could lead to conclusions different from those now widely accepted. Most of these findings have already been published in [27].

Studied samples were fabricated by a common process described in Section 3.1. At first Au contacts were deposited on both faces from an aqueous solution of 1% $AuCl_3$, creating “ohmic-type” detectors; these samples are marked by the suffix “-O” in Table I.4.4. After all measurements had been completed, Au contacts were removed and new contacts were deposited on the same samples: Au was prepared on one face of the detector using the same method, while indium was evaporated onto the other side. These “Schottky-type” samples are identified by the suffix “-S” in Table I.4.4. Bulk resistivity of bare samples was estimated using SemiMap Contactless Resistivity Mapping system, COREMA [54].

Successful preparation process of sample contacts was checked by comparing current–voltage (I–V) characteristics of both ohmic- and Schottky-type detectors. The linearity of I–V curves of BNL2E2-O and BNL2G1F3-O was proved, i.e, the slope of I–V curves was constant over the whole measured bias range no matter of bias polarity. In Schottky-type samples the different slopes of I–V characteristics for $U > 0$ and $U < 0$ demonstrated

Table I.4.4: Sample properties

Sample	Contacts	Thickness L (mm)	$\mu\tau$ (cm^2/V)	Bulk resistivity ($\Omega\,$cm)
BNL2E2-O	Au/Au	1.65	1.4×10^{-3}	4.6×10^{9}
BNL2E2-S	Au/In	1.58	1.8×10^{-3}	4.6×10^{9}
BNL2G1F3-O	Au/Au	1.92	2.0×10^{-3}	1.3×10^{10}
BNL2G1F3-S	Au/In	1.85	2.5×10^{-3}	1.3×10^{10}

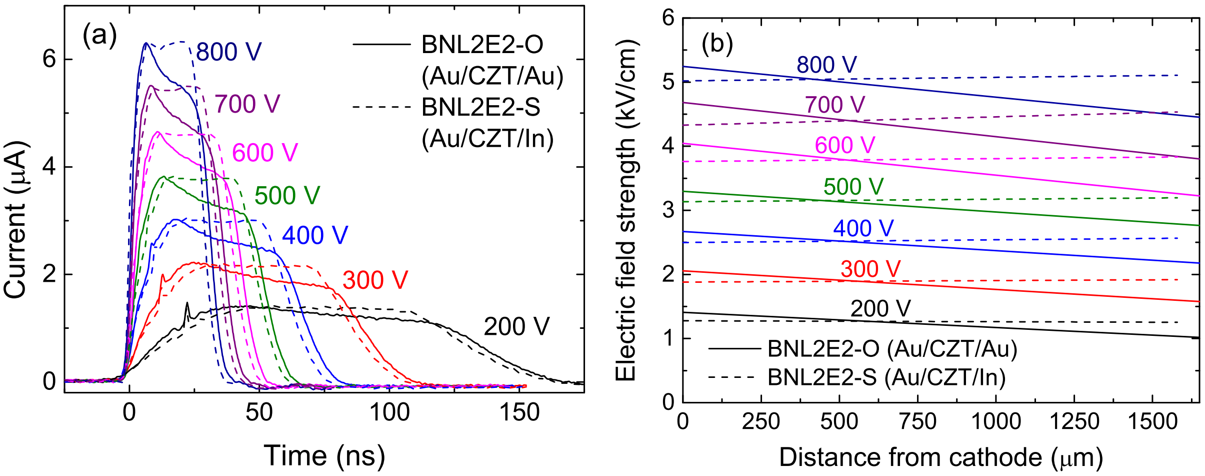

Figure I.4.11: (a) TCT waveforms measured on BNL2E2 detectors at various bias voltages. In BNL2E2-O the exponentially decreasing parts of the pulses reveal the positive space charge within the detector. (b) Electric field profiles calculated for BNL2E2 detectors for various bias voltages.

a (slightly) rectifying shape of I–V curves which is typical for samples with Au and In contacts. E.g., on applying 600 V of bias voltage on the Au cathode, the current measured in BNL2E2-O/-S and BNL2G1F3-O/-S detectors was, respectively, 19 nA/14 nA and 18 nA/12 nA.

Fig. I.4.11a depicts the TCT waveforms measured on BNL2E2 for different bias voltages ranging from 200 V to 800 V; Fig. I.4.12a shows the results for BNL2G1F3. The lack of time evolution for the waveforms observed at a fixed bias implies that the measurements were acquired under steady-state conditions. All waveforms were averaged over 500 transients during computer-aided acquisition. To explain the basic characteristics of the current waveforms in Figs. I.4.11a and I.4.12a and to better clarify evaluation of the profiles of the electric fields, a few comments on the general shape of a waveform are offered at first. The start and end points of a fitting curve are chosen so as to best fit the current transient to assumed exponential function and to cover as many data points as possible to reduce the calculation error. Since according to Eq. (I.2.16) the transit time, t_{tr}, scales directly as a square of the sample thickness, L, and inversely with the applied bias, U, t_{tr} recorded at a fixed bias on Schottky-type samples was slightly shorter (by about 7–9%) than that measured on the ohmic ones because the thickness of Schottky-type samples was reduced by etching (see Table I.4.4). The extended rise time of current transient

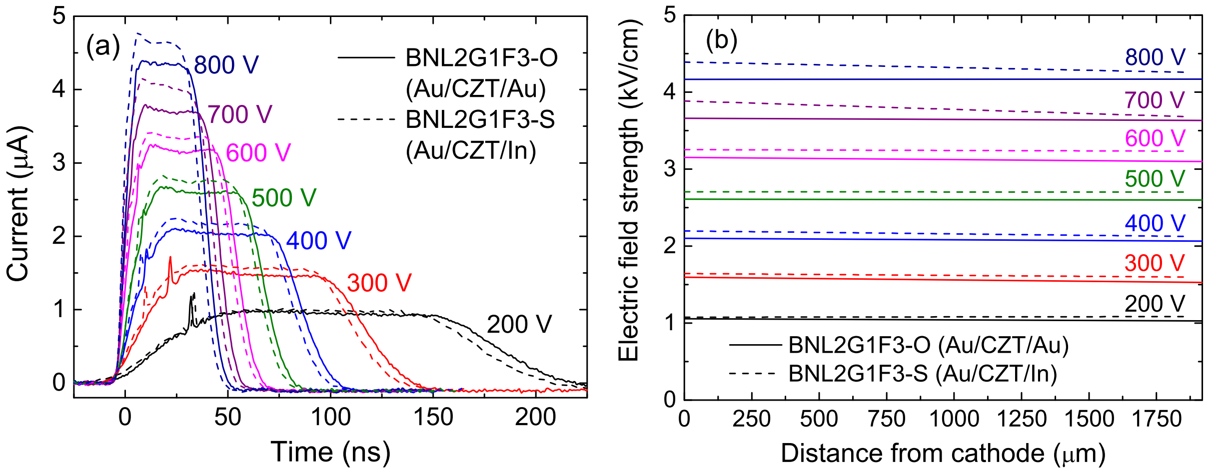

Figure I.4.12: (a) TCT waveforms measured on BNL2G1F3 detectors at various bias voltages. In both ohmic- and Schottky-type detectors the nearly flat transients reveal low polarization of samples. (b) Electric field profiles calculated for BNL2G1F3 detectors for various bias voltages.

that is apparent especially at lower biases is related to the erosion of the electron–hole plasma formed due to relatively large energy of the incident α-particles. As demonstrated in Section 4.2 the plasma effect does not disturb the evaluation of the electric field profile that is deduced from analysis of the middle part of the waveform.

Under the assumption of a homogeneous space-charge density within the detector bulk, the current transient $i(t)$ is given by Eq. (I.2.12). In high quality samples such as those used in this research, μ is large (calculations gave μ around 1100 cm^2/Vs in all samples) and $\tau \approx 1000$ ns does not markedly influence the damping of $i(t)$ of polarized samples having $a \geq 1$ kV/cm^2. In contrast, in those samples with nearly flat profile of the electric field ($a \ll 1$ kV/cm^2), it is τ what governs the damping of current transients.

The profiles of the electric fields calculated from the current transients shown in Figs. I.4.11a and I.4.12a are displayed in Figs. I.4.11b and I.4.12b. In BNL2E2-O sample the electric field decreases from the cathode to the anode, reflecting a positive space charge in the sample. Quantitatively, the calculations yield a space-charge density of 2×10^{10} cm^{-3}. In the Schottky-type BNL2E2-S the evaluated space-charge density of -3×10^9 cm^{-3} is of opposite sign to that of BNL2E2-O. The reason underlying this difference in space-charge density is discussed later in the text. Experience shows that the overall error in calculated values of space-charge density (including noise in the experimental data, fitting of current transients, and further mathematical processing) could be as high as 1–3×10^9 cm^{-3}, so making the TCT method unreliable for measuring a degree of space charge less than about 10^9 cm^{-3} and a comparably low degree of polarization in detectors associated with such small space charge. Therefore, the calculated value of -3×10^9 cm^{-3} should be (regardless of sign) considered as the upper limit for the actual space-charge density within the BNL2E2-S sample with a nearly homogeneous electric field. Very low polarization effects were observed in BNL2G1F3 samples when changing the contact metals. The electric field is homogeneous in both BNL2G1F3-O and BNL2G1F3-S detectors; in both the space-charge density was estimated to be $\lesssim 10^9$ cm^{-3}.

It is also notable that long-term storage (for periods of months to years) of detectors in air without any surface passivation may, in some cases, increase the surface leakage current and/or induce changes in the electric field profile, both degrading the detector per-

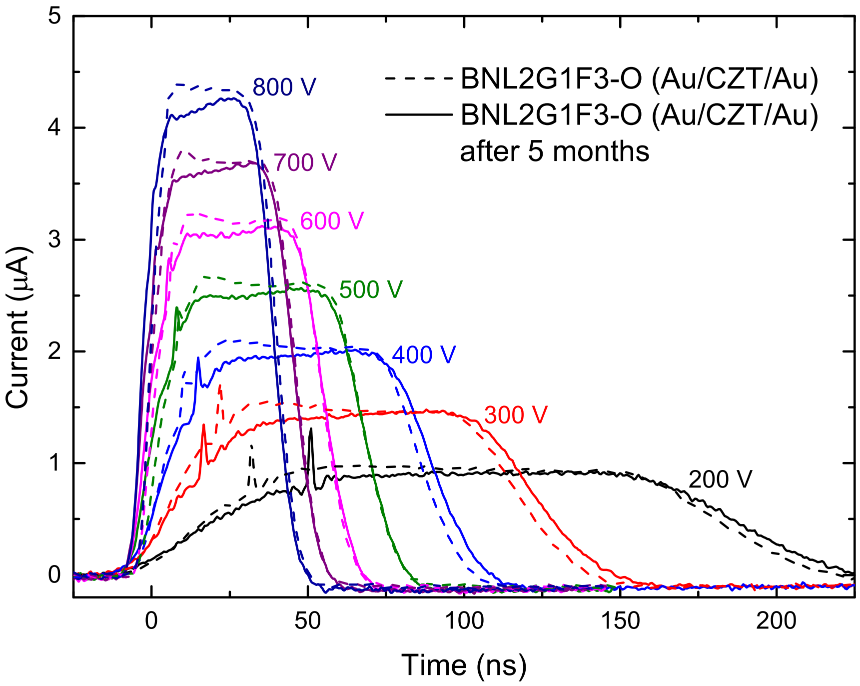

Figure I.4.13: TCT waveforms measured on BNL2G1F3-O detector at various bias voltages five months after preparing the contacts. The exponential part of the pulse changed from originally decreasing to increasing after storage.

formance. This behaviour was observed in BNL2G1F3 sample as illustrated in Fig. I.4.13. Five months after the preparation of contacts a reversal in the sign of the space-charge density was recorded, giving a negative space charge with the density of -8×10^9 cm^{-3} in BNL2G1F3-O, and, simultaneously, a significant increase of current was observed in I–V characteristics (from 3 nA to $\sim$10 μA at $\sim$100 V).

One key result is the finding that the ohmic Au/CZT/Au sample BNL2E2-O polarizes, i.e., a space charge is formed within the detector bulk, but the Schottky-type Au/CZT/In BNL2E2-S does not, that is, there is no space charge or, more likely, the space charge is below the detection limit of TCT. Nevertheless, the electric field is homogeneous in either case. Observed modifications in the detector polarization state while changing the contact metal of the anode only support the interpretation that a deep hole trap, probably a deep acceptor, is responsible. Its binding energy, E_T, is localized below the equilibrium Fermi energy, E_F, as schematically depicted in Fig. I.4.14. The occupancy of the hole trap is ruled by the exchange of holes with the valence band, such that their injection or depletion may induce significant space-charge formation on that level, regardless of the type of material conductivity. The only criterion for charging of the level is the shift of the hole quasi-Fermi energy in the proximity of E_T. The electron/hole trap does not unambiguously imply the donor/acceptor-like character of the defect [55].

Moreover, it can be deduced that E_T is close to E_F in BNL2E2-O, so that the shift of hole quasi-Fermi energy in a biased sample markedly influences its occupancy. Assuming that bands are bent upwards at Au contacts as sketched in Fig. I.4.14a, the injection of holes increases the positive charge on this trap level. Conversely, using a hole blocking In anode results in depletion of the positive charge, detrapping of residual holes on that level, and causes the formation of a negative space charge in the detector. Because $E_T < E_F$

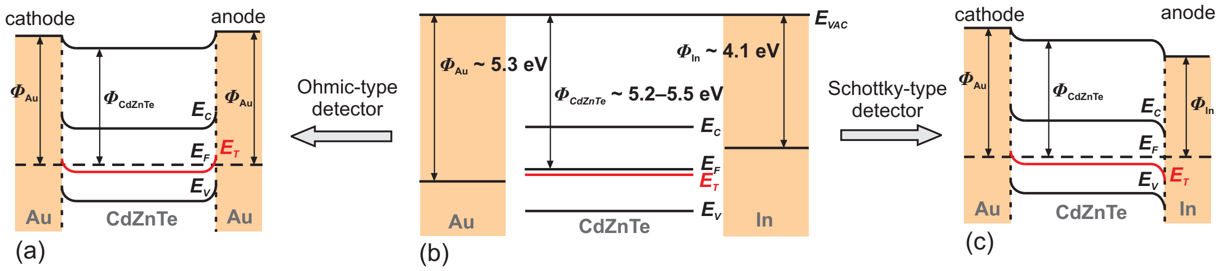

Figure I.4.14: Band structure of (a) an ohmic-type and (c) Schottky-type detectors, and (b) energy level diagram of CdZnTe. The work functions were taken from [56].

the positive charge in the Au/CZT/Au sample is significantly larger than the negative charge in the Au/CZT/In sample, what was confirmed by the experimental results giving 2×10^{10} cm^{-3} in BNL2E2-O in contrast to $\lesssim 10^9$ cm^{-3} in BNL2E2-S.

These findings contradict the conventional model of polarization of semiconductor radiation detectors [28, 38, 55], which predicts the tendency of Schottky-type detectors to polarize more easily than ohmic ones. In the conventional model a greater negative space charge is apparent in Schottky-type detectors due to thermally-activated detrapping of holes from the hole trap situated above E_F; in ohmic-type detectors the hole quasi-Fermi energy remains far from E_T and there is no clearly observable space charge. Generally, when the cathode is left unchanged (Au) and the anode metal is changed, then the relation between E_T and E_F determines the preferred contact material for the anode as follows:

(i) $E_T < E_F$ is optimal for the Schottky contact, but improper for the ohmic one (observed situation);

(ii) $E_T > E_F$ is optimal for the ohmic contact, improper for the Schottky one.

Keeping these findings in mind may help to choose the preferred contact materials.

No significant effects on the profiles of the electric fields were seen in BNL2G1F3 in both the Au/CZT/Au and Au/CZT/In contact configurations. Therefore, one can deduce that there are no apparent trap levels in this sample near E_F that could be recharged due to quasi-Fermi level shift, i.e., the band bending does not affect trap occupancy. As the bulk resistivity of BNL2G1F3 is approximately three times greater than that of BNL2E2 (see Table I.4.4), its E_F is shifted $\sim$28 meV closer to E_T. If a hole-trap level in BNL2G1F3 existed with a similar density as in BNL2E2, space-charge formation would have been observed. Because no apparent waveform distortion is seen in BNL2G1F3, it could be deduced that the density of hole traps is much smaller. As E_T remains well below E_F even in BNL2G1F3 then because the space-charge density is not greater than 10^9 cm^{-3}, the hole-trap density in this sample must be at least 60 times smaller than in the BNL2E2 sample.

To support previous considerations, the existing code for the parallel solution of drift-diffusion and Poisson's equation in semi-insulating CdTe and CZT [57] was utilized to calculate the charging of CZT detector under standard working conditions. The parameters selected for the simulation were chosen as to match material characteristics of the BNL2E2 sample and to fit the evaluated space charge and current through the detector. The following values were used: $E_g = 1.58$ eV [58, 59], $E_F = E_c - 0.73$ eV $= E_v + 0.85$ eV, $E_T = E_v + 0.72$ eV, trap density $N_T = 1.3 \times 10^{12}$ cm^{-3}, temperature $T = 295$ K, and sample thickness $L = 1.6$ mm. It is notable that the trap characteristics was chosen rather

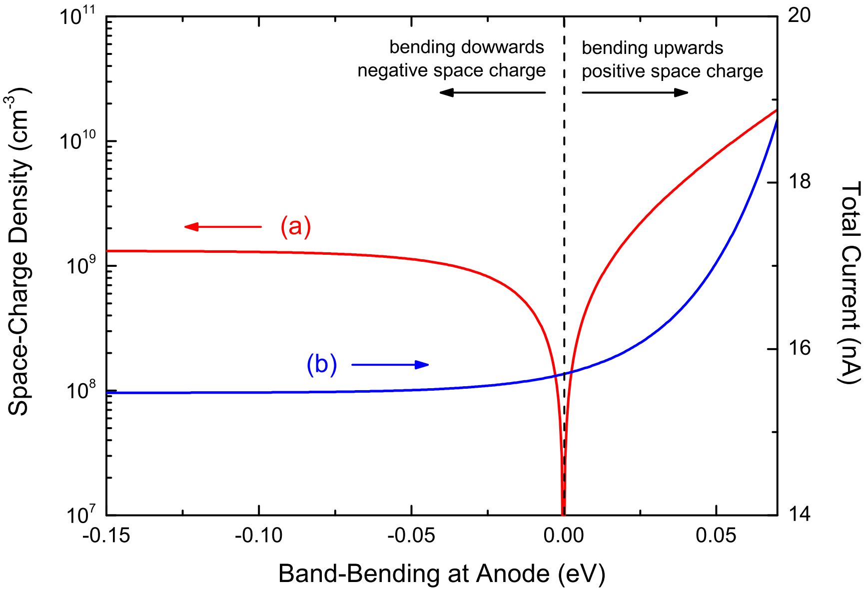

Figure I.4.15: Numerical simulation of (a) the average space-charge density and (b) the total current at 600 V as functions of band bending at the anode calculated for the parameters given in the text. The total current through the sample with dimensions equal to BNL2E2 was calculated rather than the current density to enable direct comparison of calculated and experimental values.

arbitrarily since measurements taken at a fixed temperature do not allow to establish E_T and N_T uniquely. The hole-capture cross section at the trap level does not need to be adjusted in the steady-state experiment when neglecting electron trapping.

Fig. I.4.15a represents the computed dependence of the average space-charge density on the band bending at the anode; it confirms excellently the observations made on BNL2E2 detectors. The calculations for bands being bent downwards at the anode (Schottky contact) yield that the space-charge density saturates at $\sim 10^9$ cm^{-3}. This value agrees well with the measured profiles of the electric field in BNL2E2-S (see Fig. I.4.11b and the discussion thereof). In contrast, for bands bending upwards at the anode (ohmic contact), the space-charge density strongly depends on the band bending, reaching the value of 2×10^{10} cm^{-3} for the bending of 70 meV attributed to the Au contact. Calculated values of the space-charge density are both qualitatively and quantitatively confirmed by the results of TCT measurements, showing that BNL2E2-O becomes polarized more than BNL2E2-S.

The dependence of the total current through the sample on the band bending at the anode at 600 V (Fig. I.4.15b) demonstrates why Schottky In contacts are not as promising on n-type detectors as on p-type ones. Due to the weakly blocking Au cathode, the n-type Au/CZT/In detector shows no significant suppression of the dark current in comparison to the same material with ohmic contacts. Simultaneously, the eventual appearance of a hole-trap level above E_F would entail significant space-charge formation and polarization of the detector. In the present situation at 600 V, the calculations demonstrated that the current through the sample changes very slowly with band bending; it differs only by 3 nA with a bending change of ±70 meV (see Fig. I.4.15b). This difference also agrees well with the measured results.

One could also speculate about an explanation of well-known different tendencies of Schottky CdTe and CZT detectors to polarize when CdTe-S does so much more quickly and extensively than CZT-S. Adding zinc to CdTe both increases the E_g and shifts E_F further from E_v, i.e., above the principal hole-trap level in semi-insulating material. Consequently, such a level is filled with electrons and does not emit holes in hole-depleted Schottky CZT detectors, while simultaneously suppressing the space-charge formation caused by this level. In [60] a similar model of trap elimination by Fermi-level engineering was discussed.

Regardless of polarization caused by biasing the sample, the degradation of the detector performance over time could be caused by long-term processes at the metal–semiconductor interface as well as on the detector surface, even when no bias is applied to the sample. Since the work functions of Au, Φ_{Au}, and CZT, Φ_{CZT}, are very similar (see Fig. I.4.14b) and, particularly in CZT, depend on many different factors mostly associated with the surface and interface [61], a situation could arise when $\Phi_{\mathrm{Au}} < \Phi_{\mathrm{CZT}}$, resulting in bands being bent downwards at this contact. This injecting contact would then cause a rapid increase in forward current and, in addition, could be the reason for the observed sign reversal of the space charge as shown in Fig. I.4.13.

4.4 Summary

General theory for processing of TCT and CCE measurements on planar radiation detectors, involving single-carrier collection of either electrons or holes regardless of the polarization of the detector and the bias polarity, was reported. A thorough analysis of various methods used for the evaluation of the mobility–lifetime product was given. The results obtained by utilizing the well-know Hecht equation, the Matz approach with an effective space-charge density, and two newly developed methods—the self-consistent procedure and the direct-minimization procedure which combine the CCE and TCT measurements in one complex calculation—were mutually compared. It was shown both on the simulated data and real CdTe and CZT detectors that when the polarization of a detector is not negligible, the standard simple methods (Hecht, Matz) can yield incorrect values of $\mu\tau$, although the fits may describe the measured bias dependence of CCE well. In these situations the information about the actual profiles of the electric field in the detector, obtained either from the TCT or Pockels effect measurements, must be included into calculations. This task was successfully completed by utilizing the reported procedures. Developed methods were demonstrated with success on the study of effect of different contact metals on the internal electric field within detectors.

Part II

High-temperature measurements of the absorption edge

1. Introduction

The bandgap energy, E_g, is one of the most important parameters characterizing a semiconductor and predestinating its possible applications. General requirements for E_g of a material that should operate as a room temperature radiation detector were summarized in points (ii) and (iii) in Preface. In addition, at high temperatures E_g critically affects the intrinsic carrier density and native defect structure and it is therefore important for reliable modeling of the defect structure [62]. Detailed acquirement of the high-temperature bandgap energy edge is also necessary for *in-situ* monitoring of CdTe vapour-phase growth using optical methods [63]. The temperature dependence of E_g was widely studied at low temperatures 4–300 K [3, 58, 64, 65, 66, 67, 68, 69]. The absorption coefficient of 22000 cm^{-1} at E_g was determined at 4 K from measurements on a few micrometers thick samples [70]. The list of earlier experiments may be found in [8]. Optical properties of CdTe thin films were investigated also in [71, 72, 73] in the temperature range 90–500 K, where the dependence of the bandgap energy of CdTe thin films on the thickness of the film was reported as well.

Temperature dependence of the absorption edge of CdTe was studied as early as in 1959 by de Nobel [3], where the spectral transmission of a 0.2 mm thick bulk CdTe wafer was measured at 77 K and in the temperature range 300–983 K in vacuum. The upper temperature limit could not be exceeded due to the decomposition of CdTe. The bandgap energy was approximated by the energy corresponding to a zero transmission deduced from the spectral transmission curve. High-temperature absorption edge of CdTe in temperature interval of 827–1104 K was measured by Mullins *et al.* [63] from the incandescent spectra of a CdTe wafer under Ar overpressure and by Su [74] who measured transmission spectra of a sublimated 1.5 mm thick CdTe sample under the congruent sublimation condition. The bandgap energy was established from the derivative of the absorption coefficient with respect to energy between 304 K and 1067 K. High-temperature energy bandgap was evaluated also from the high-temperature Hall effect measurement in the temperature interval of 700–1100 K [62]. These methods have yielded different results, the comparison of which is to be found in Chapter 4. At temperatures above 800 K the difference in $E_g(T)$ could be as high as 0.2 eV! The question then naturally arises of which values of $E_g(T)$ should be taken for calculations considering samples studied at IoP CU. To remove this uncertainty the experimental setup for high-temperature measurements of the absorption edge has been built in the laboratory of IoP CU.

Analytical models suitable for the fitting of $E_g(T)$ are mostly based on the Varshni equation [75]:

$$E_g(T) = E_g(0) - \frac{\gamma T^2}{T+\beta}, \tag{II.1.1}$$

where $E_g(0)$ represents the bandgap energy at 0 K and β is approximated by the Debye temperature, which is assumed to be 160 K for CdTe [74] for the purpose of later analyses. Another approach originating from the model of Pässler [76] uses the formula

$$E_g(T) = E_g(0) - \frac{\kappa\theta_p}{2}\left[\sqrt[p]{1+\left(\frac{2T}{\theta_p}\right)^p} - 1\right], \tag{II.1.2}$$

where θ_p approximately equals to the average phonon temperature and p corresponds to the material-specific degree of phonon dispersion. The parameter $\kappa = S(\infty)$ represents the $T \to \infty$ limiting magnitude of the slope $S(T) = \mathrm{d}E_g/\mathrm{d}T$, supposing that $S(T)$ is the entropy related to the temperature dependence of the bandgap $E_g(T)$ [77, 78]. Temperature dependence of E_g is the result of a cumulative effect of electron–phonon interaction and thermal lattice expansion. The absorption edge is spread with increasing temperature because of phonon population increase, charging of impurities and defects, and population of electron and hole states in the conduction and valence bands. In spite of multiple effects affecting bandgap renormalization, it was shown in [79] that a linear dependence of the bandgap

$$E_g(T) = E_g(0) - \gamma T \tag{II.1.3}$$

may be expected well above the Debye temperature. The latter equation then represents the high-temperature limit of the Varshni formula, easily derivable from Eq. (II.1.1) for $T \gg \beta$. A linear dependence from Eq. (II.1.3) may be alternatively expressed in the form

$$E_g(T) = E_g(T_0) - \gamma'(T - T_0) \tag{II.1.4}$$

with a reference temperature T_0. In order to easily deduct the room temperature bandgap energy from the latter equation, T_0 is preferably set to 300 K.

In this part of the thesis the measurements of the infrared transmission of CdTe samples under nearly saturated Cd overpressure in the temperature interval 295–1223 K are reported. The optical absorption coefficient is calculated from the transmittance spectra and the high temperature bandgap energy is evaluated by the extrapolation of the Urbach absorption tail from a spectrum of the absorption coefficient. It is for the first time when the high-temperature absorption edge of CdTe is measured under defined Cd overpressure, so allowing to reach pretty high temperatures without principal sample sublimation and serious surface degradation.

2. Processing of experimental data

2.1 Calculation of transmittance spectra

Spectral dependence of the transmittance $T(\lambda)$ on the wavelength λ of a studied thin sample can be calculated from simple equations describing the reflection and refraction of light propagating through homogeneous, isotropic, non-magnetic media. Such a medium is described by its complex refractive index

$$\hat{n}(\lambda) = n(\lambda) + \mathrm{i}\kappa(\lambda), \tag{II.2.1}$$

where $n(\lambda)$ and $\kappa(\lambda)$ are, respectively, the real and imaginary component of the index of refraction, $\hat{n}$. The imaginary part, $\kappa(\lambda)$, can be directly related to the absorption coefficient, $\alpha(\lambda)$, via the equation

$$\alpha(\lambda) = \frac{4\pi}{\lambda}\kappa(\lambda). \tag{II.2.2}$$

At normal incidence the reflectance $R(\lambda)$ of a single boundary between two media is given by

$$R(\lambda) = \left|\frac{\hat{n}_1(\lambda) - \hat{n}_2(\lambda)}{\hat{n}_1(\lambda) + \hat{n}_2(\lambda)}\right|^2, \tag{II.2.3}$$

where $\hat{n}_1(\lambda)$ and $\hat{n}_2(\lambda)$ are complex refractive indices of the media. Specially, for one of the media being the air (vacuum), by setting $\hat{n}_1(\lambda) \equiv 1$ and substituting Eq. (II.2.1) for $\hat{n}_2(\lambda)$, Eq. (II.2.3) can be evolved into the form

$$R(\lambda) = \frac{\big(n(\lambda) - 1\big)^2 + \kappa^2(\lambda)}{\big(n(\lambda) + 1\big)^2 + \kappa^2(\lambda)}, \tag{II.2.4}$$

if $n(\lambda)$ and $\kappa(\lambda)$ are components of the complex refractive index of the non-trivial medium. Assuming that the studied sample is surrounded by air from both sides, the equation for total transmittance of the sample, $T(\lambda)$, is calculated by taking into account multiple internal reflections on air–sample boundary and neglecting the interference effects, yielding

$$T(\lambda) = \frac{\big(1 - R(\lambda)\big)^2 \mathcal{T}(\lambda)}{1 - R^2(\lambda)\mathcal{T}^2(\lambda)}. \tag{II.2.5}$$

In latter equation $\mathcal{T}(\lambda)$ marks that fraction of light which is absorbed during one pass through the sample. This quantity is calculated using the Lambert-Beer's law

$$\mathcal{T}(\lambda) = e^{-\alpha(\lambda)L} = e^{-4\pi\kappa(\lambda)L/\lambda}, \tag{II.2.6}$$

where $\alpha(\lambda)$ was substituted from Eq. (II.2.2) and L is the thickness of the sample. The assumption of multiple internal reflections is justifiable since, e.g., for the sub-bandgap irradiation ($\alpha(\lambda) \approx 0$) a single surface of a CdTe sample with the refractive index $n(\lambda) \doteq 2.8$ reflects around 23% of incident light, which therefore cannot be neglected.

As discussed in [63], for a relatively thick sample (measurements discussed later in Chapter 4 were performed on samples having $L \sim 0.5$ mm), achievable values of absorption coefficient $\alpha(\lambda)$ are not much above 100 cm^{-1}. From Eq. (II.2.2) the corresponding values of $\kappa(\lambda)$ are less than 0.02. For this reason $\kappa(\lambda)$ can be neglected in Eq. (II.2.4), from which one obtains the well-known equation for the reflectance of a boundary between a non-absorbing medium and air:

$$R(\lambda) = \left(\frac{n(\lambda) - 1}{n(\lambda) + 1}\right)^2. \tag{II.2.7}$$

Finally, by substituting Eq. (II.2.6) into Eq. (II.2.5) the relation between $T(\lambda)$ and $\alpha(\lambda)$ can be written in the form

$$T(\lambda) = \frac{\big(1 - R(\lambda)\big)^2 e^{-\alpha(\lambda)L}}{1 - R^2(\lambda)e^{-2\alpha(\lambda)L}}. \tag{II.2.8}$$

2.2 Calculation of absorption spectra

The latter equation can be solved for $\alpha(\lambda)$ to explicitly write the absorption coefficient as a function of the transmittance:

$$\alpha = -\frac{1}{L} \ln \left\{ \sqrt{\frac{1}{4T^2}\left(\frac{1-R}{R}\right)^4 + \frac{1}{R^2}} - \frac{1}{2T}\left(\frac{1-R}{R}\right)^2 \right\}. \tag{II.2.9}$$

Wavelength dependence of $\alpha(\lambda)$, $T(\lambda)$, and $R(\lambda)$ is omitted to simplify the result. To evaluate the spectral dependence of the absorption coefficient $\alpha(\lambda)$ using Eq. (II.2.9), the dispersion curve $n(\lambda)$ for the calculation of the single-boundary reflectance $R(\lambda)$ and the transmittance spectrum $T(\lambda)$ must be known either from literature or experiment.

2.2.1 Dispersion relation of CdTe

For the dispersion relation $n(\lambda)$ of CdTe, two models are adopted in this thesis:

(i) Expression (II.2.10) of Pikhtin and Yas'kov [80].

(ii) Expression (II.2.11) of Hlídek *et al.* [81].

Pikhtin and Yas'kov approximated the dispersion curve of a semiconductor with a sphalerite structure by the formula

$$n^2(\hbar\omega) - 1 = \frac{A}{\pi} \ln \left(\frac{E_1^2 - (\hbar\omega)^2}{E_0^2 - (\hbar\omega)^2} \right) + \frac{G_1}{E_1^2 - (\hbar\omega)^2} + \frac{G_2}{E_2^2 - (\hbar\omega)^2} + \frac{G_{TO}}{E_{TO}^2 - (\hbar\omega)^2}, \tag{II.2.10}$$

where the energies E_i have a clear physical meaning: E_0, E_1, E_2, and E_{TO} are, respectively, the fundamental bandgap energy, the energy gaps at the L and X points of the Brillouin zone, and the energy of the transverse optical phonon; G_1, G_2 are the dispersion parameters related to the effective masses and oscillator strengths at those critical points, and G_{TO} is the dispersion parameter of the transverse optical phonon [80]. Numerical values of above constants at room temperature for the case of CdTe are summarized in Table II.2.1.

Hlídek *et al.* approximated their measurements of refractive index of CdTe in the temperature range from 10 K to 295 K by the four-oscillator model

$$n^2(\hbar\omega, T) - 1 = a + \sum_{i=1}^{4} \frac{g_i(T)}{E_i^2(T) - (\hbar\omega)^2}, \tag{II.2.11}$$

Table II.2.1: Numerical values of parameters in oscillator model given by Eq. (II.2.10) according to Pikhtin and Yas'kov [80] at $T = 293\,\mathrm{K}$.

A	E_0 (eV)	E_1 (eV)	G_1 (eV^2)	E_2 (eV)	G_2 (eV^2)	E_{TO} (eV)	G_{TO} (eV^2)
0.572	1.50	3.2	28.5519	5.5	94.3804	17.40	9.02×10^{-4}

Table II.2.2: Numerical values of parameters in four-oscillator model given by Eq. (II.2.11) according to Hlídek *et al.* [81].

Parameter	Value at $T = 293\,\mathrm{K}$
$a = 3.153$	3.153
$E_1(T) = 1.5976 - \frac{6.09\times10^{-4}T^2}{T+255}$ (eV)	1.5022
$g_1(T) = \left(0.0369 - \frac{9.26\times10^{-5}T^2}{T+22.4}\right) \times \left(1 - \frac{0.0946}{1+e^{20-555/T}}\right)$ (eV^2)	0.0117
$E_2(T) = 1.7102 - \frac{5.04\times10^{-4}T^2}{T+208}$ (eV)	1.6238
$g_2(T) = 0.3454\ \mathrm{eV}^2$	0.3454
$E_3(T) = 3.2668 - \frac{2.794\times10^{-4}T^2}{T+112.5}$ (eV)	3.2076
$g_3(T) = 39.966\ \mathrm{eV}^2$	39.966
$E_4(T) = 0.018$ eV	0.018
$g_4(T) = 9.02\times10^{-4}\ \mathrm{eV}^2$	9.02×10^{-4}

which was fitted to the experimental data. In the latter equation the term $i = 1$ denotes the contribution of optical transitions near the bandgap, terms with $i = 2$ and $i = 3$ approximate the effect of all higher transitions, and term $i = 4$ represents lattice vibrations [81]. In contrast to Pikhtin and Yas'kov, the refractive index as well as the most of model parameters are considered to be temperature-dependent. Evaluated temperature dependencies of these parameters together with their values at room temperature are shown in Table II.2.2.

In Fig. II.2.1 the comparison of the dispersion models of Pikhtin and Yas'kov and Hlídek *et al.* at room temperature is to be found. Calculations approved that the difference between the refractive indices of both dispersion models is negligible in the spectral region interesting for reported measurements. As a result the spectra of the absorption coefficient are almost unaffected by the choice of the dispersion model. The model of Pikhtin and Yas'kov is used for further analysis.

2.2.2 Experimental transmittance

In order to evaluate the sample transmittance $T(\lambda)$ at an arbitrary temperature from the range 300–1300 K, two measurements are performed:

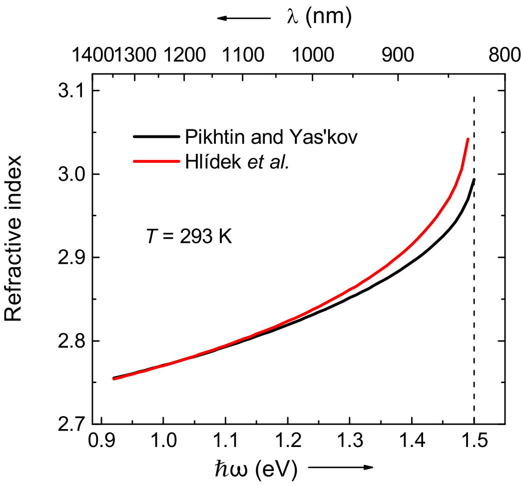

Figure II.2.1: Dispersion models of CdTe at room temperature according to Pikhtin and Yas'kov [80] and Hlídek *et al.* [81].

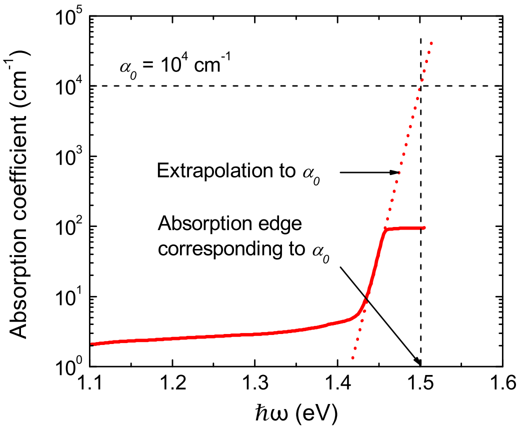

Figure II.2.2: Typical spectrum of the absorption coefficient. Extrapolation to a given value of α_0 gives an estimate of the absorption edge.

(i) Intensity of light passing through the studied sample, $I_s(\lambda)$, is measured in the range from 800 nm to 1400 nm, which covers the region where the absorption edge of CdTe is expected in the above temperature range.

(ii) Intensity of light in the same experimental arrangement but with the sample removed (a reference spectrum), $I_r(\lambda)$, is measured in the same spectral region.

Then, the transmittance $T(\lambda)$ is calculated as a ratio of these two quantities:

$$T(\lambda) = \frac{I_s(\lambda)}{I_r(\lambda)}. \tag{II.2.12}$$

This calculation is repeated for different temperatures to obtain experimental data for analysis of temperature dependence.

Having both $n(\lambda)$ and $T(\lambda)$ available, one can use Eq. (II.2.9) to calculate the spectrum of absorption coefficient $\alpha(\lambda)$, a typical shape of which is shown in Fig. II.2.2. The absorption coefficient of CdTe as well as of other semiconductors is below the bandgap energy expected to exhibit an exponential absorption tail described by the Urbach rule [82, 83]

$$\alpha(\hbar\omega) = \alpha_0 e^{\frac{\hbar\omega - E_{\alpha_0}}{E_U}}, \tag{II.2.13}$$

where E_{α_0} is the energy at a chosen value α_0 of the absorption coefficient and E_U describes the spreading of the band tail below the fundamental bandgap due to disorder. Consequently, the exponential tail makes it impossible to observe the interband absorption $\alpha(\hbar\omega) \sim \sqrt{\hbar\omega - E_g}$ directly. By extrapolating the linear part of a semi-logarithmic plot of the energy spectrum of the absorption coefficient, E_{α_0} can be addressed by fixing the value of α_0 as schematically depicted in Fig. II.2.2. In this thesis the results of different choices of α_0 are discussed later in Chapter 4.

Two important notes are worth mentioning. Firstly, by assuming that the fitted value of E_{α_0} is so close to the fundamental bandgap that it can be identified with a particular parameter in dispersion relation discussed above (e.g., with E_0 in the dispersion curve

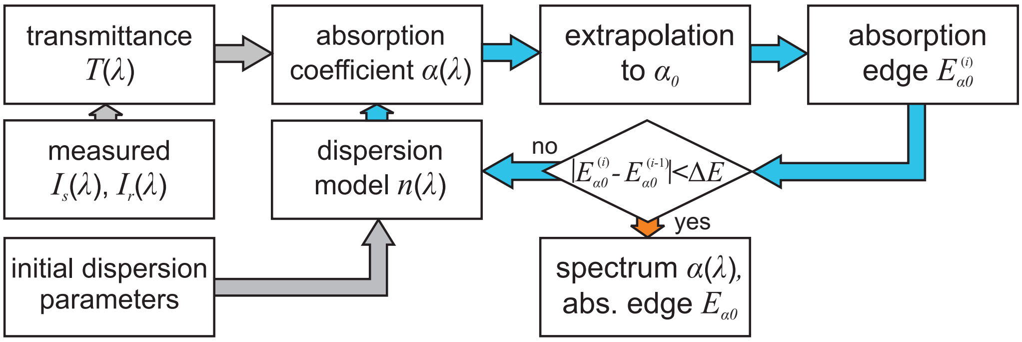

Figure II.2.3: Flow chart of the procedure for the calculation of absorption spectra and the evaluation of the energy of absorption edge.

according to Eq. (II.2.10), or with E_1 in Eq. (II.2.11)), then any change of this parameter in $n(\lambda)$ also changes the resulting $\alpha(\lambda)$ calculated using Eq. (II.2.9), i.e., the spectrum from which the energy E_{α_0} was estimated. The consequences are discussed in the following Subsection 2.2.3. Secondly, the evaluation of absorption coefficient via Eq. (II.2.9) relies on the correct estimation of transmittance spectrum according to Eq. (II.2.12). If, e.g., an unintentional difference occurs in experimental setups between measurements with and without a sample or transmittance $T(\lambda)$ is evaluated incorrectly, errors are consequently passed on an estimate of the bandgap energy. This is discussed separately in Section 2.3.

2.2.3 Evaluation of absorption coefficient: a self-consistent treatment

The above note about the mutual relationship between the dispersion curve $n(\lambda)$ that is used to calculate the absorption coefficient $\alpha(\lambda)$, from which, however, the fundamental bandgap energy entering the expression for $n(\lambda)$ is obtained, states the requirement for the calculation being done self-consistently. The procedure proceeds as follows:

(i) From the measured spectra of $I_s(\lambda)$ and $I_r(\lambda)$, the transmittance spectrum $T(\lambda)$ is calculated using Eq. (II.2.12).

(ii) The spectrum of absorption coefficient $\alpha(\lambda)$ is calculated with the help of Eq. (II.2.9) using the dispersion model according to Eq. (II.2.10) with the initial set of parameters shown in Table II.2.1.

(iii) The absorption coefficient is plotted in a semi-logarithmic scale as a function of energy, $\alpha(\hbar\omega)$, and a linear part of the spectrum (in a semi-logarithmic scale, i.e., the exponential part in a linear scale) in the region of approx. 10–100 cm^{-1} is fitted according to the Urbach rule described by Eq. (II.2.13).

(iv) Fitted curve is extrapolated to the chosen value of α_0, yielding the corresponding energy of the absorption edge, $E_{\alpha_0}^{(1)}$, on a horizontal axis.

(v) The dispersion model parameter E_0 representing the fundamental bandgap is adjusted to the estimated energy of the absorption edge, $E_{\alpha_0}^{(1)}$.

(vi) Procedure repeats starting at step (ii) with a new set of dispersion parameters until the absorption edge energy estimated at the end of the ith cycle, $E_{\alpha_0}^{(i)}$, differs for less than a chosen convergence criterion from its value from the previous step, $E_{\alpha_0}^{(i-1)}$. The difference $|E_{\alpha_0}^{(i)} - E_{\alpha_0}^{(i-1)}| < \Delta E = 10^{-5}$ eV is used in this thesis.

When the procedure converges, the energy of the absorption edge, E_{α_0}, corresponding to the chosen α_0 is obtained. The flow chart of this procedure is schematically shown in Fig. II.2.3.

2.3 Analysis of calculation errors

Eq. (II.2.12) is of fundamental importance as it provides the relation between experimental data $I_s(\lambda)$ and $I_r(\lambda)$ and theoretical model presented in Sections 2.1 and 2.2. In this section it is demonstrated how an experimental error in measured transmittance affects the overall uncertainty of calculated values of absorption edge and Urbach parameter.

To do so a dimensionless parameter, $\xi \sim 1$, is defined to characterize the error in experimental transmittance. $T(\lambda)$ is then substituted by $\xi T(\lambda)$ in Eq. (II.2.9) to express an incorrect value. To make further manipulations easier, the latter equation is rewritten as follows:

$$\alpha = -\frac{1}{L} \ln \left(\sqrt{Q^2 + \mathcal{R}^2} - Q \right), \tag{II.2.14}$$

where $\mathcal{R} = 1/R$ and Q stands for

$$Q = \frac{(\mathcal{R} - 1)^2}{2T}.$$

Wavelength dependencies are omitted. The substitution $T \leftrightarrow \xi T$ leads to Q being replaced by Q/ξ and Eq. (II.2.14) transforms into

$$\alpha = -\frac{1}{L} \ln \left(\sqrt{\frac{Q^2}{\xi^2} + \mathcal{R}^2} - \frac{Q}{\xi} \right) = -\frac{1}{L} \ln \left\{ \frac{1}{\xi} \left(\sqrt{Q^2 + \xi^2 \mathcal{R}^2} - Q \right) \right\}. \tag{II.2.15}$$

In the vicinity of the absorption edge the transmittance $T \to 0$, which implies $Q \gg 1$ and thus $Q \gg \xi \mathcal{R}$. The square root in Eq. (II.2.15) can then be approximately expressed as

$$\sqrt{Q^2 + \xi^2 \mathcal{R}^2} = Q \sqrt{1 + \frac{\xi^2 \mathcal{R}^2}{Q^2}} \approx Q \left(1 + \frac{\xi^2 \mathcal{R}^2}{2Q^2} \right) = Q + \frac{\xi^2 \mathcal{R}^2}{2Q},$$

resulting in the equation for the absorption coefficient in the limit of low transmittance:

$$\alpha^{(T \to 0)} = -\frac{1}{L} \ln \left(\frac{\mathcal{R}^2}{2Q} \right) - \frac{1}{L} \ln \xi. \tag{II.2.16}$$

If one expresses ξ in the form $\xi = 1 \pm \varepsilon$, the latter equation gives

$$\Delta\alpha = -\frac{1}{L} \ln \xi = -\frac{1}{L} \ln(1 \pm \varepsilon) \approx \mp \frac{\varepsilon}{L} \tag{II.2.17}$$

for the absolute error (regardless of sign) of absorption coefficient calculated from transmittance spectra with the relative uncertainty ε. Eq. (II.2.17) can then be used for the construction of error bands (see Fig. II.2.4) in a spectrum of absorption coefficient to estimate the accuracy of the results.

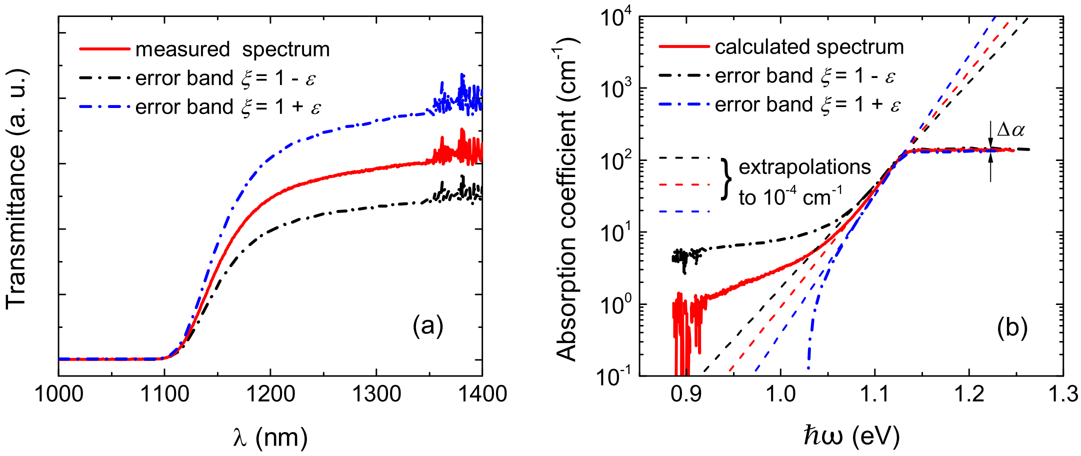

Figure II.2.4: Uncertainty in measured transmittance spectrum (a, linear scale) is passed on the calculated spectrum of absorption coefficient (b, logarithmic scale).

To assess the corresponding effect on the calculated values of the fundamental bandgap, detail analysis of steps (iii) and (iv) of the self-consistent treatment in Subsection 2.2.3 is necessary. Let us assume that two spectra of absorption coefficient, $\alpha^{(1)}(\hbar\omega)$ and $\alpha^{(2)}(\hbar\omega) = \alpha^{(1)}(\hbar\omega) + \Delta\alpha$, where $\Delta\alpha = (-\ln\xi)/L$, are given. One can interpret these as a calculated spectrum and one of its error bands (depending on the sign of $\pm/\mp$ marks in Eq. (II.2.17)). The exponential parts of the spectra are then fitted according to Eq. (II.2.13). To take benefit from well-known equations for a linear regression, the logarithm of the Urbach rule is taken:

$$\ln\alpha(\hbar\omega) = \ln\alpha_0 + \frac{\hbar\omega}{E_U} - \frac{E_{\alpha_0}}{E_U},$$

and a new notation is introduced:

$$\ln\left(\frac{\alpha(\hbar\omega)}{\alpha_0}\right) = \frac{\hbar\omega}{E_U} - \frac{E_{\alpha_0}}{E_U} = m\hbar\omega + b, \tag{II.2.18}$$

where

$$m = \frac{1}{E_U}, \qquad b = -\frac{E_{\alpha_0}}{E_U} = -mE_{\alpha_0}. \tag{II.2.19}$$

The equations determining the best-fit values of coefficients m and b, neglecting measurement uncertainties, are then [43]:

$$\begin{aligned} m &= \frac{N\sum E_i y_i - \left(\sum E_i\right)\left(\sum y_i\right)}{N\sum E_i^2 - \left(\sum E_i\right)^2}, && \text{(II.2.20)} \\ b &= \frac{\sum y_i - m\sum E_i}{N}, && \text{(II.2.21)} \end{aligned}$$

where N is the number of data points, $E_i = (\hbar\omega)_i$ is the energy of a particular data point, and

$$y_i = \ln\left(\frac{\alpha(E_i)}{\alpha_0}\right) \tag{II.2.22}$$

is the logarithm of the absorption coefficient at energy E_i normalized to α_0. Two pairs of parameters, $(m^{(1)}, b^{(1)})$ and $(m^{(2)}, b^{(2)})$, can then be calculated by inserting $\alpha^{(1)}(\hbar\omega)$

and $\alpha^{(2)}(\hbar\omega)$ into Eqs. (II.2.20) and (II.2.21). If $(m^{(1)}, b^{(1)})$ is the pair corresponding to $\alpha^{(1)}(\hbar\omega)$, one proceeds further by looking for its relation to $(m^{(2)}, b^{(2)})$. At first, Eq. (II.2.22) is written for the spectrum $\alpha^{(2)}$ in the form:

$$\begin{aligned} y^{(2)} = \ln\left(\frac{\alpha^{(2)}}{\alpha_0}\right) &= \ln\left(\frac{\alpha^{(1)}+\Delta\alpha}{\alpha_0}\right) = \ln\left\{\frac{\alpha^{(1)}}{\alpha_0}\left(1+\frac{\Delta\alpha}{\alpha^{(1)}}\right)\right\} \\ &= \ln\left(\frac{\alpha^{(1)}}{\alpha_0}\right) + \ln\left(1+\frac{\Delta\alpha}{\alpha^{(1)}}\right) = y^{(1)} + \Delta y, \end{aligned} \tag{II.2.23}$$

where

$$\Delta y = \ln\left(1+\frac{\Delta\alpha}{\alpha^{(1)}}\right). \tag{II.2.24}$$

After simple math a linear shift between coefficients $m^{(1)}$, $m^{(2)}$ and $b^{(1)}$, $b^{(2)}$ can be found from Eqs. (II.2.20) and (II.2.21), yielding $m^{(2)} = m^{(1)} + \Delta m$ and $b^{(2)} = b^{(1)} + \Delta b$, while

$$\Delta m = \frac{N\sum E_i\Delta y_i - \left(\sum E_i\right)\left(\sum \Delta y_i\right)}{N\sum E_i^2 - \left(\sum E_i\right)^2}, \tag{II.2.25}$$

$$\Delta b = \frac{\sum \Delta y_i - \Delta m \sum E_i}{N}, \tag{II.2.26}$$

supposing that $\Delta y_i = \Delta y\big(\alpha^{(1)}(E_i)\big)$ is substituted from Eq. (II.2.24). Finally, the absorption edge energies corresponding to the chosen α_0 and extrapolated from the exponential parts of particular absorption spectra are obtained from Eq. (II.2.19), yielding

$$\begin{aligned} E_{\alpha_0}^{(1)} &= -\frac{b^{(1)}}{m^{(1)}}, \\ E_{\alpha_0}^{(2)} &= -\frac{b^{(2)}}{m^{(2)}} = -\frac{b^{(1)}+\Delta b}{m^{(1)}+\Delta m} = E_{\alpha_0}^{(1)} + \Delta E_{\alpha_0}. \end{aligned} \tag{II.2.27}$$

For the Urbach parameters the same procedure yields

$$\begin{aligned} E_U^{(1)} &= \frac{1}{m^{(1)}}, \\ E_U^{(2)} &= \frac{1}{m^{(2)}} = \frac{1}{m^{(1)}+\Delta m} = E_U^{(1)} + \Delta E_U. \end{aligned} \tag{II.2.28}$$

It is left without a proof that for $\xi = 1 \mp \varepsilon \lesseqgtr 1$, both $\Delta E_{\alpha_0} \gtrless 0$ and $\Delta E_U \gtrless 0$ as clearly observed from Fig. II.2.4.

Having the difference between $(m^{(1)}, b^{(1)})$ and $(m^{(2)}, b^{(2)})$ pairs determined, the uncertainty in input data, i.e., transmittance spectrum $T(\lambda)$, is reflected on the final calculated value of fundamental bandgap and Urbach parameter according to the following approach:

(i) E_{α_0} and E_U are evaluated from absorption coefficient spectra according to the procedure presented in Subsection 2.2.3.

(ii) Relative experimental error, ε, of measured transmittance spectra is estimated, determining $\xi = 1 \pm \varepsilon$.

(iii) Two new values, $E_{\alpha_0}^{(\pm)}$ and $E_U^{(\pm)}$, one greater and one less than the original quantity, are obtained for both E_{α_0} and E_U according to the equations above. The ± values then represent the limiting values (error bands) spread around E_{α_0} and E_U due to the transmittance uncertainty ε. Corresponding differences $\Delta E_{\alpha_0}^{(\pm)}$ and $\Delta E_U^{(\pm)}$ are evaluated.

(iv) Final values of E_{α_0} and E_U are then defined as:

$$\begin{aligned} E_{\alpha_0} &\equiv E_{\alpha_0} \pm \Delta E_{\alpha_0}, && \text{(II.2.29)} \\ E_U &\equiv E_U \pm \Delta E_U, && \text{(II.2.30)} \end{aligned}$$

where ΔE_{α_0} and ΔE_U are the averages of $\Delta E_{\alpha_0}^{(\pm)}$ and $\Delta E_U^{(\pm)}$.

3. Experimental techniques

High-temperature measurements of optical properties of CdTe as described in this part of the thesis are based on measuring of the transmittance spectra of a sample placed in the two-zone furnace perpendicularly to an optical beam. To ensure well-defined thermodynamic conditions at high temperatures, the sample is placed in a sealed quartz ampoule (see Fig. II.3.1). It is important to prepare a sufficiently thin sample to enable transmittance measurements; however, the sample has to be thick enough to withstand vibrations and shaking during the preparation of the ampoule. Procedure with a 0.5 mm thick sample has been successfully examined. In the following text the fabrication process of samples as well as of the quartz ampoule and the experimental setup are described in detail.

3.1 Preparation of samples for high-temperature measurements

Starting with an approximately 2 mm thick CdTe wafer cut using a diamond-wire saw Model 6234 from Well Diamond Wire Saws, Inc. from an as-grown CdTe crystal, the wafer is checked for the presence of gains and twins at first. If there is a monocrystalline piece large enough (i.e., with dimensions greater than intended dimensions of the sample being prepared), the wafer is subsequently cut on a steal-wire saw. Different sample geometries had been tried before the shape shown in Fig. II.3.1d was adopted. A square-shaped sample is firstly cut by making two series of parallel cuts. Consequently, corners are removed by another two series of parallel cuts, resulting in a sample of desired shape. Though this procedure is more difficult and takes more time than cutting of a rectangular sample, its advantage is evident: the sample of such a shape, when placed into the sample holder (Fig. II.3.1c) inside the quartz ampoule, occupies nearly the whole inner area of the ampoule. The diameter of the optical beam, controlled by an iris diaphragm aperture size, entering the furnace can thus be larger than that in the case of a rectangular sample, which results in higher signal yield at the detector. The thickness of the shaped sample is then mechanically reduced on a grinding machine. Before the desired thickness of 0.5 mm is reached, sample faces are pre-chemically polished using abrasives and then chemically polished to provide an optical-grade surface. The plano-parallelity and roughness of the surface can be tested using Noncontact 3D Surface Profiler from Zygo [84]. Finally, the sample is chemically etched in 3% bromine–methanol solution and rinsed in methanol and isopropyl alcohol before inserting it into the sample holder and completing the ampoule.

The quartz ampoule consists of the inner (Fig. II.3.1a) and outer (Fig. II.3.1b) parts. The inner part is fabricated from a quartz tube with 18.5 mm in outer diameter and a wall thickness of 1.5 mm supplied by Heraeus Quarzglas. After cutting the tube of desired length (110 mm), one end is rounded on a grinding plate, while onto the other one the optical-grade quartz window is fused. The most challenging work is the fusing of a quartz tube with 4 mm in diameter to the body of the ampoule according to Fig. II.3.1a. It requires the experience of a skilled glassworker to make a vacuum-tight connection without infolding of the fused quartz into the ampoule. The 4 mm quartz tube serves then as the outlet to vacuum system.

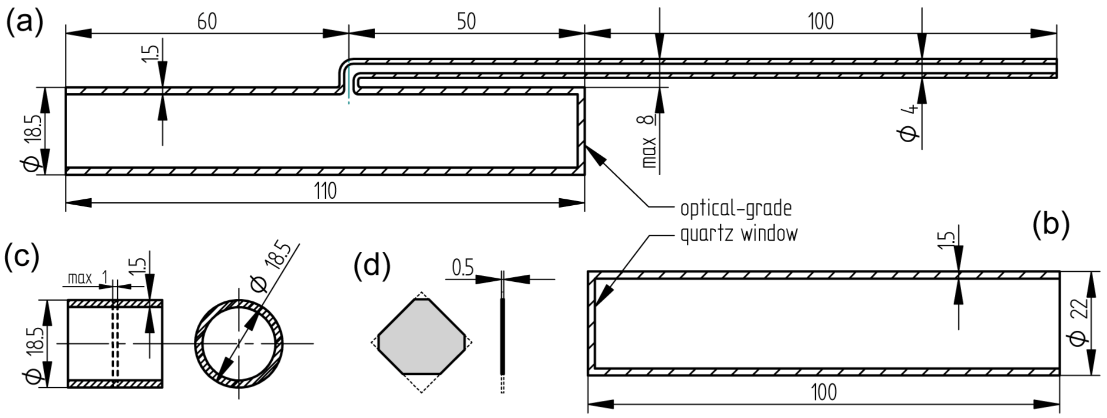

Figure II.3.1: Drawings of particular parts of the quartz ampoule: (a) inner ampoule, (b) outer ampoule, (c) sample holder, (d) front and side views of the shape of a sample.

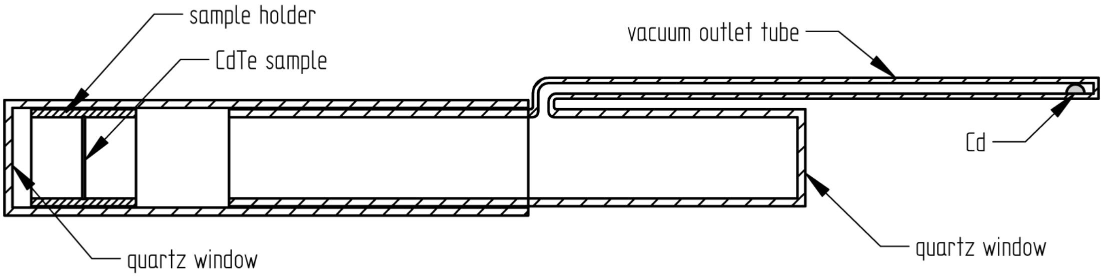

Figure II.3.2: Assembled quartz ampoule for high-temperature transmission measurements.

The outer part of the ampoule is fabricated from a quartz tube with 22 mm in outer diameter and the same wall thickness of 1.5 mm as in the case of the inner part. One end of an approximately 100 mm long tube is rounded, whereas the quartz window of optical quality is fused onto the other one. When both parts of the ampoule are put together, the matching between the outer diameter of the inner part and the inner diameter of the outer part makes it possible to seal both parts together using an oxygen–hydrogen torch while evacuating the ampoule at the same time. If the inner ampoule is hard to be inserted into the outer one, ampoules are etched in hydrofluoric acid for several tens of minutes to reduce the wall thickness.[1]

The sample holder (Fig. II.3.1c) is fabricated from a piece of the same tube that is used for the inner ampoule. Its ends are grinded and using a diamond-blade circular saw a notch is made in the middle of the tube perpendicularly to its axis. The edges of the notch are smoothed by an oxygen–hydrogen torch to prevent the sample from scratching when being inserted. The notch should be planar and thin so as to enable the insertion of the sample without unnecessary space around it. The sample placed into the sample holder should not protrude out of the holder and should withstand vibrations during the manipulation and sealing of the ampoule.

Before completion of the ampoule, all its parts, i.e., the inner and outer ampoule, and sample holder, are thoroughly cleaned by etching in chromosulfuric acid and then etched

---

[1] The matching of both parts of the ampoule should be checked at the whole beginning of the fabrication process. If it were left after the quartz windows are fused, then hydrofluoric acid etching for more than 15–20 minutes could damage the surface of the windows and could cause vacuum leaks.

in hydrofluoric acid for 15 minutes. After the etching, all parts are rinsed by deionized water and placed to the laboratory hot-air dryer. Then, the process proceeds in the following steps:

(i) Studied sample is placed in the sample holder that is inserted into the outer part of the ampoule. A droplet of elementary Cd is put into the inner ampoule.

(ii) Inner part of the ampoule is inserted into the outer one in such a way that the vacuum outlet tube and sample orientations in the ampoule are the same as in Fig. II.3.2. Sample must not fall out of the sample holder! A Cd droplet should be on the opposite side of the ampoule than the sample.

(iii) Vacuum outlet is connected to a system of vacuum pumps by Leybold–Heraeus (rotary pump, turbomolecular pump), which is started.

(iv) Both parts of the ampoule are sealed together using an oxygen–hydrogen torch by fusing the overlapping walls of the inner and outer ampoules starting from the vacuum outlet tube and proceeding ahead. Beware of exposing both the sample and Cd droplet to oxygen–hydrogen flame for more than a moment!

(v) The sealed ampoule is pumped down to pressure of approximately 10^{-5} mbar, which is enough for the sample to withstand long-term high-temperature measurements.

(vi) Vacuum outlet tube is sealed in the middle by an oxygen–hydrogen torch to completely seal the ampoule and to disconnect it from the vacuum-pumping system.

The quartz ampoule fabricated in this way should look like that in Fig. II.3.2. It is now ready for measurement.

3.2 Experimental setup

Measurements presented in Part II of this thesis were carried out in the experimental arrangement shown in Fig. II.3.3. The 50 W tungsten halogen lamp biased to 12 V by Protek PL-3005S DC Regulated Power Supply is used to generate incandescent light. Right away from the circular aperture of the lamp cover, the light beam is periodically interrupted by an optical chopper maintained by the Stanford Research Systems Model SR540 Chopper Controller at the frequency of about 180 Hz. After the reflection on a spherical mirror, the light is led on a system of two plano-convex lenses in order to produce a collimated beam. The amount of light passing around the quartz ampule with a studied sample through the custom-made Elsklo two-zone tube furnace (30 mm tube diameter × 500 mm length) is reduced by an iris diaphragm placed into the light path in front of the entrance of the furnace. The aperture of the diaphragm is set so that only the light incident on the sample is allowed to propagate through the furnace. The furnace entrance is closed up by an optical-grade quartz window to prevent unwanted air-flow from disturbing the settling of desired thermodynamic conditions. The temperature in both zones (one zone is desired for controlling the Cd temperature, the other one is for controlling the temperature of a sample) is controlled by the Eurotherm 3504 Process Controller via the type S thermocouples. To precisely monitor temperature, thermocouples are placed directly within the furnace in the vicinity of the sample and Cd. The temperature of zones' windings is monitored simultaneously. Only the long-wave part ($\lambda > 800$ nm) of the light beam

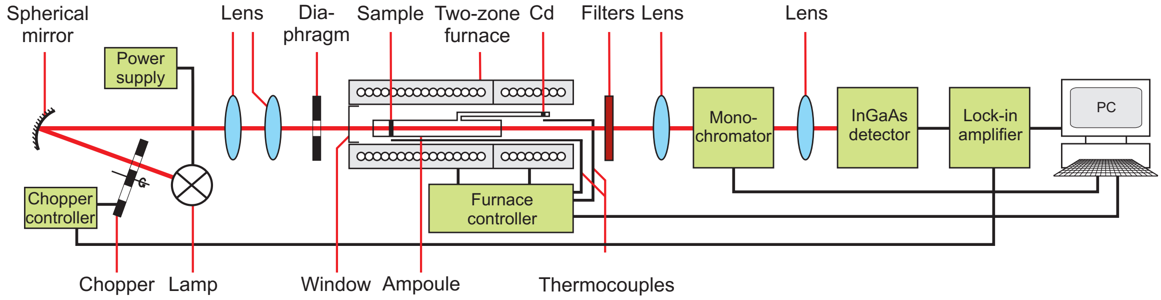

Figure II.3.3: Experimental setup for measurements of high-temperature absorption edge.

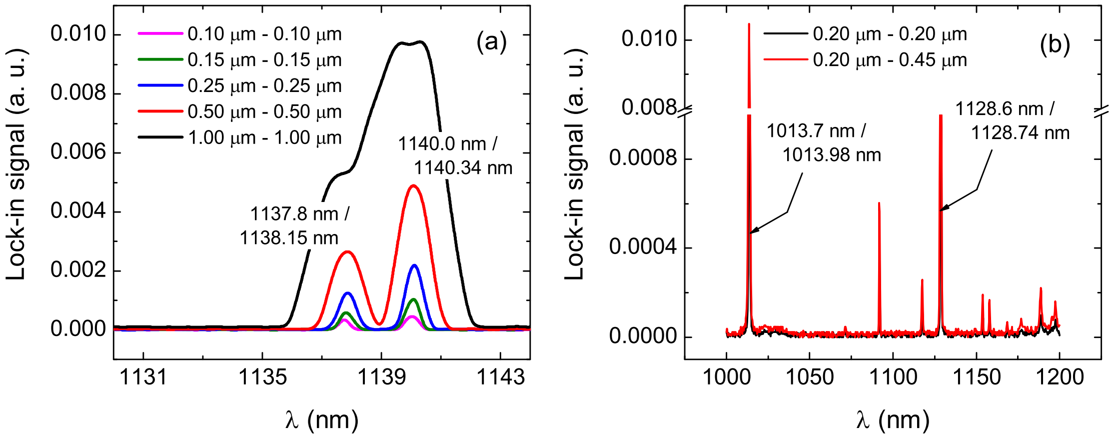

Figure II.3.4: Recorded spectra of (a) sodium-vapour lamp and (b) mercury-vapour lamp for different widths of the entrance–exit slits of the monochromator. The first number in peak description is the value measured by presented setup, the value following the slash was found in literature [85, 86].

leaving the furnace transmits through the longpass filters and is focused by a lens on the entrance slit of the Princeton Instruments Acton SpectraPro 2300i Monochromator. With a 1200 g/mm grating blazed at 776 nm, both the entrance and exit slit widths set to 0.5 mm, and grating rotation speed of 30 nm/min, it is able to record an 800–1400 nm spectrum in 20 minutes. The output from the monochromator is focused by a lens on the ThorLabs PDA-10CD-EC InGaAs Amplified Detector with the gain of 40 dB. The amplified signal is led via the shielded coaxial cable to the Stanford Research Systems SR830 DSP Lock-In Amplifier, which is directly connected to the PC, controlling and synchronizing all parts of the setup.

The experimental arrangement described above optimizes the throughput and provides sufficient signal-to-noise ratio and spectral resolution. Experiments with a sodium- and mercury-vapour lamps in place of a halogen lamp allowed to perform the wavelength calibration of the monochromator and to find the optimal settings for the monochromator, detector, and lock-in amplifier by recording two near sodium emission lines, 1138.15 nm and 1140.34 nm (Fig. II.3.4a), and two mercury emission lines, 1013.98 nm and 1128.74 nm (Fig. II.3.4b). Based on these observations the monochromator and detector were set as described above, and lock-in amplifier as follows: time constant 100 ns and sensitivity around 10 mV to optimally utilize the measurement range. The comparison of measured and tabulated spectral lines maxima revealed that the wavelength accuracy in a near-infrared region is better than 0.4 nm with a resolution around 1 nm.

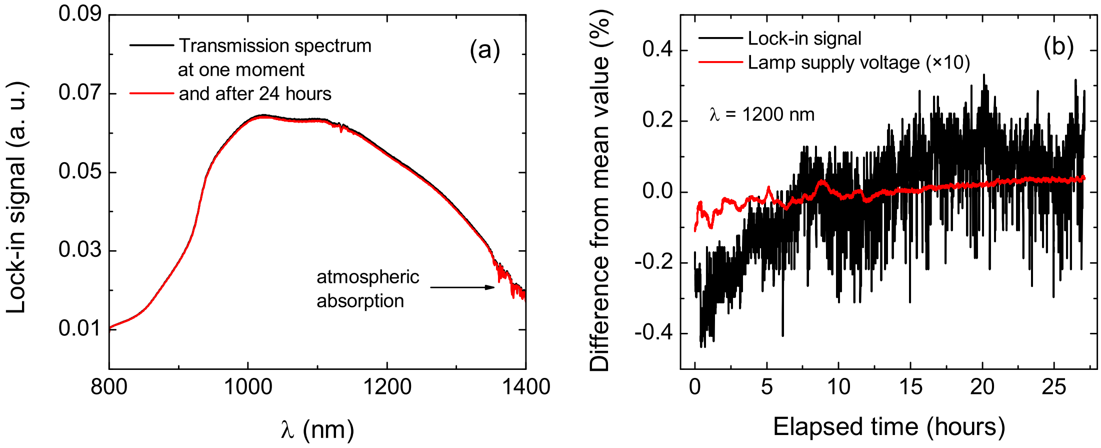

Figure II.3.5: (a) Transmittance spectra without the sample measured at one moment and after 24 hours. The difference is less than 1%. (b) Temporal stability test of the setup showing the differences of the lock-in signal recorded at a particular wavelength and halogen-lamp power-supply voltage from their mean values.

Temporal stability of the setup was tested as well since high-temperature measurements usually take many hours to accomplish. Any drift of the calibration as well as changes in the intensity of a light source (either because of aging of tungsten filament or power-supply fluctuations), unintended stir of optical elements or other equipment would deteriorate the measurements before completion. That is why all parts of the setup were permanently mounted on a robust optical table, paying special attention on fixing the thermocouples so as not to screen the light passing through the furnace.

Transmittance spectra of the furnace without the sample measured 24 hours one after another are depicted in Fig. II.3.5a. These spectra, the shape of which results from concurrent effects of the monochromator, detector, and lock-in amplifier on a lamp emission spectrum after propagating through several optical elements and throughout the furnace, are characteristic for the setup and will serve as reference spectra for calculation of experimental transmittance according to Eq. (II.2.12). The difference between the spectra is less than 1%. A signal at the output from the lock-in amplifier at $\lambda = 1200$ nm and the light source power-supply voltage recorded several times per minute for more than 24 hours are shown in Fig. II.3.5b. It is nicely demonstrated that after the first few hours needed for all instruments to warm up and a signal to settle down, the fluctuations of the output signal are approximately $\pm 0.3\%$. The stability of the power-supply voltage is much better. Therefore, one can expect that the overall error of spectral measurements does not exceed 1–2%.

4. Results and Discussion

In this chapter high-temperature optical measurements of the absorption edge of single-grain CdTe samples grown and prepared at the Institute of Physics of Charles University are presented. These are some of the first results; extensive study has not been completed yet. Basic information about the samples is summarized in Table II.4.1. Applicability of models discussed in Chapter 2 is demonstrated and deeply analyzed. Obtained results are compared to existing ones and are to be published soon [87].

4.1 Transmittance spectra

In Fig. II.4.1 "raw" spectra of transmittance of samples as recorded directly on the lock-in amplifier are depicted. These spectra, representing $I_s(\lambda)$ in Eq. (II.2.12), are later used together with previously recorded reference spectrum $I_r(\lambda)$ for the calculation of experimental transmittance. It became evident from the first experiments that minimizing the stray light and light passing around the samples is important for pushing the above-bandgap transmittance down to zero to minimize the residual transmittance. In Figs. II.4.1 the amount of the above-bandgap signal is markedly reduced with the help of an iris diaphragm placed in front of the furnace as discussed in Chapter 3. As will be seen later, this enables to extend the upper limit of measurable absorption coefficient up to 120 cm^{-1}. Higher values are not reachable on samples of such a thickness. Transmittance spectra of S49I1 and S49I2 undoped CdTe samples, calculated with the help of Eq. (II.2.12) from raw transmittance spectra already reported, are to be found in Figs. II.4.2a and II.4.2b. The spectra were measured from the lowest ($\sim$300 K) to the highest ($\sim$1200 K) temperature with the step of 50 K. Difference between Cd temperature and sample temperature was

Table II.4.1: Sample properties

Sample	S49I1	S49I2
Material	CdTe	CdTe
Thickness L (mm)	0.45	0.44

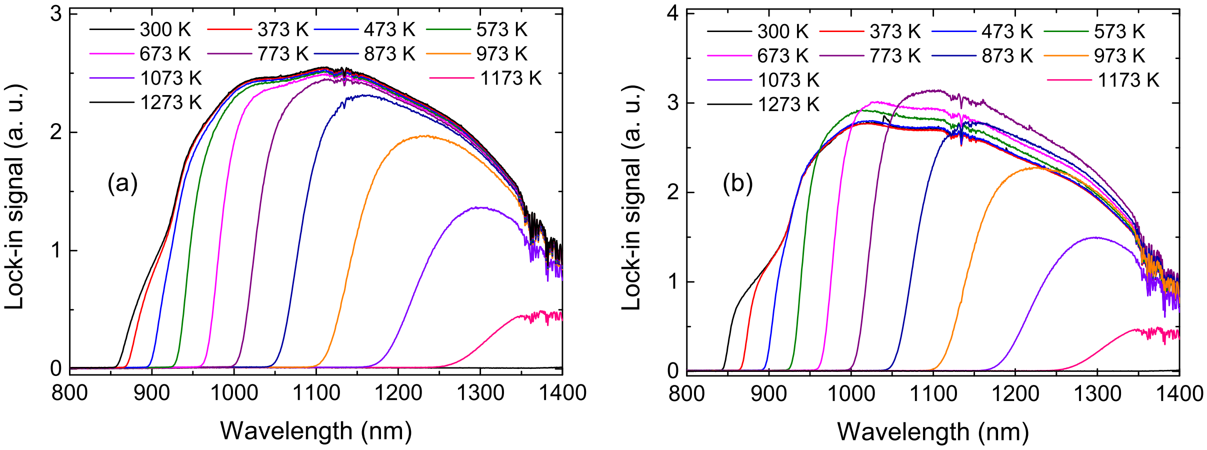

Figure II.4.1: "Raw" transmittance spectra of (a) S49I1 and (b) S49I2 detectors recorded directly on the lock-in amplifier.

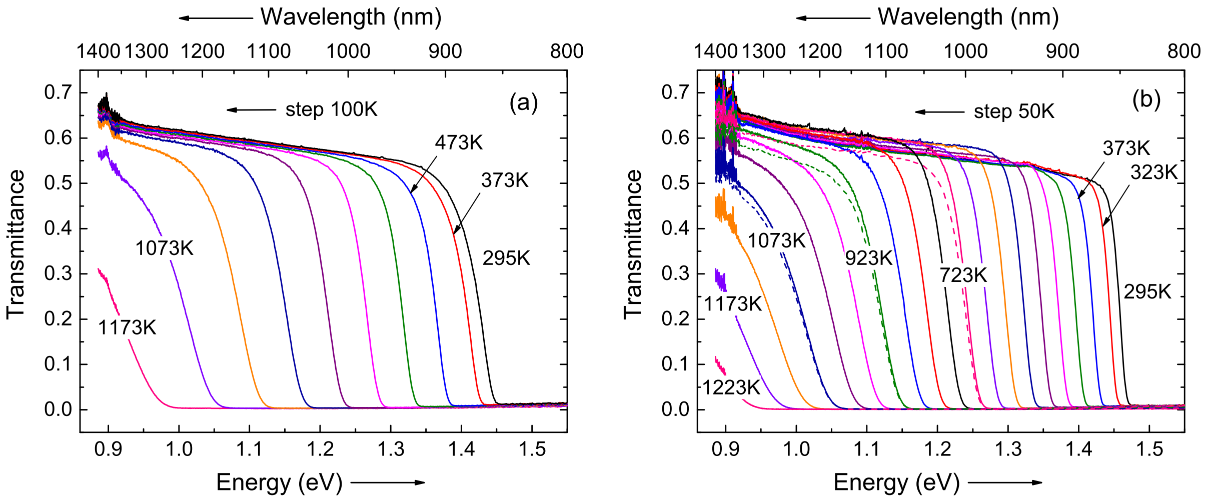

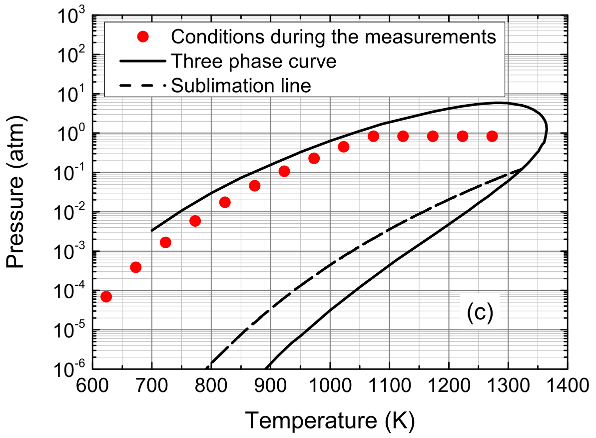

Figure II.4.2: Transmittance spectra of (a) S49I1 and (b) S49I2 detectors. Dashed lines in (b) represents measurements at the same temperatures during the cooling down back to room temperature. (c) Three phase equilibrium curve of CdTe(s) according to [89]. Red points mark the thermodynamic conditions (a Cd overpressure) during the measurements presented in this thesis.

maintained at 50 K up to 1073 K; above this value the Cd temperature was fixed at 1023 K so as not to exceed the pressure of 1 atm in the ampoule. Thermodynamic conditions during the experiment are shown in Fig. II.4.2c by red dots. The vicinity of these points to the three phase equilibrium curve implies that the measurements were performed under nearly saturated Cd overpressure. Slight variations of the maximum transmittance level in Fig. II.4.2b that appear above ∼600 K correlate with the temperature of Cd approaching and exceeding its melting point of 594 K [86]. Temperature gradient inside the ampoule could cause Cd condensating on the back optical window, thus affecting the transmitted signal. Another explanation could stem from modifications of the surface of CdTe sample resulting in a change of optical constants and overall sample transmissivity as discussed in the following paragraph.

The spectra of S49I2 were also measured at the same temperatures during the cooling down back to room temperature. They are presented by dashed lines in Fig. II.4.2b for chosen temperatures of 723 K, 923 K, and 1073 K. The transmittance spectrum measured during the cooling phase is slightly lower than the spectrum measured during the heating. This slight shift, likely caused by the formation of a thin surface layer due to Te sublimation, has already been observed during the characterization of annealed samples by means of IR microscopy or IR absorption measurements [17, 63, 88]. To recover the initial transmittance values, the surface layer would have to be removed after annealing. This would, however, require the ampoule being opened after the cooling phase of the

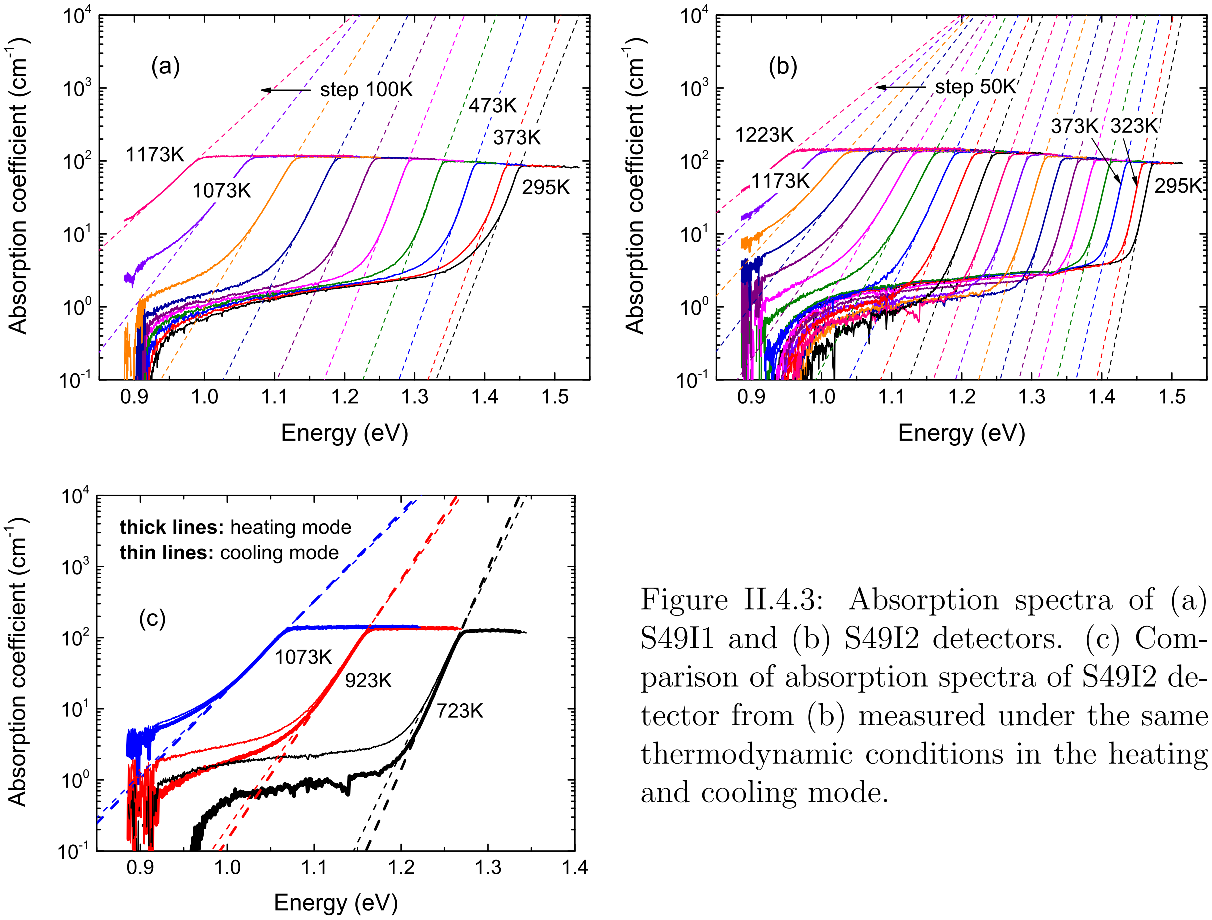

Figure II.4.3: Absorption spectra of (a) S49I1 and (b) S49I2 detectors. (c) Comparison of absorption spectra of S49I2 detector from (b) measured under the same thermodynamic conditions in the heating and cooling mode.

experiment, practically limiting the measurement to one up–down cycle. Investigations of this kind were not performed in the thesis.

4.2 Spectra of absorption coefficient. Absorption edge

The self-consistent procedure from Subsection 2.2.3 has been used to calculate the spectra of absorption coefficient from the transmittance spectra presented in Fig. II.4.2. Analogously to [63] the results for $\alpha_0 = 10^4$ cm^{-1} are to be found in Fig. II.4.3. The extrapolations to α_0 of the Urbach tails according to Eq. (II.2.13) are shown by dashed lines.

The deviation between transmission spectra recorded at the same temperatures during heating/cooling mode is naturally passed on the calculated absorption spectra and is observed in the whole temperature range. By comparing the transmittance spectra of heating and cooling modes in Fig. II.4.2b, it can be found that they are a ξ_1-multiple of one another with $\xi_1 \sim 0.94$ ($\varepsilon_1 \sim 0.06$). One can therefore utilize the results of Section 2.3 to expect the corresponding spectra of the absorption coefficient being shifted linearly from each other. This linear shift along the vertical axis is seen in Fig. II.4.3c; however, the logarithmic scale enhances the difference at low $\alpha(\hbar\omega)$.

As discussed in Section 2.3 the mutual relation ($\xi_1 < 1$) between the transmittance spectra implies that the absorption coefficient $E_{\alpha_0}^{(\uparrow)}$ evaluated in the heating mode is therefore less than $E_{\alpha_0}^{(\downarrow)}$ corresponding to the cooling mode. The difference of these two values, $\Delta E_{\alpha_0} = |E_{\alpha_0}^{(\uparrow)} - E_{\alpha_0}^{(\downarrow)}|$, is less than 0.3% and 0.5% for $\alpha_0 = 10^3$ cm^{-1} and 10^4 cm^{-1}, respectively. Similarly, $E_U^{(\uparrow)} < E_U^{(\downarrow)}$. The smallest deviation of E_U, $\Delta E_U = |E_U^{(\uparrow)} - E_U^{(\downarrow)}|$, was observed at the highest temperature; the maximum deviation of $\Delta E_U \approx 2$ meV was identified at lowest temperatures. The latter value corresponds well to the value calculated directly from Eq. (II.2.28) for $\xi_1 = 0.94$. With the uncertainty of the measured transmittance spectra (see Section 3.2) estimated to be approx. 1–2%, $\varepsilon_2 < 0.02$, the total uncertainty of $\varepsilon = \sqrt{\varepsilon_1^2 + \varepsilon_2^2} \sim 7\%$ is assumed for input data. The total error of bandgap calculations estimated with the help of the analysis presented in Section 2.3, considering transmittance fluctuations and differences between heating and cooling modes (ε_1), uncertainty in experimental data (ε_2), and the effects of mathematical processing, should not exceed 2% at any temperature. The total error of the Urbach parameter is expected to be less than 1–2 meV at any temperature for all studied samples. Values of $E_{\alpha_0}^{(\uparrow)}$ and $E_U^{(\uparrow)}$ obtained at the heating mode are later used for the discussion of temperature dependencies with the above mentioned errors.

Evaluation of the fundamental bandgap energy E_g from absorption measurements in thick samples is complicated by rather high α resulting from the Urbach band tail below E_g, which completely surpasses the square-root interband absorption $\alpha(\hbar\omega) \sim \sqrt{\hbar\omega - E_g}$. The possibility of using samples with the thickness of only a few micrometers that would enable direct observation of interband absorption [70] is limited to low temperatures only since heating highly above room temperature induces quick degradation of thin samples. Relatively thick samples are also necessary to withstand handling during the fabrication of the ampoule (Section 3.1). High temperature bandgap energy therefore had to be estimated by indirect techniques. Some of them are summarized as follows:

(i) Evaluation of E_g from the foot of a transmission curve [3].

(ii) Identification of E_g with the energy corresponding to a drop of the derivative of $\alpha(\hbar\omega)$ [74].

(iii) Evaluation of E_g that best fits a presumed linear temperature dependence from the absorption spectra calculated with a fixed $\alpha_0 = 10^4$ cm^{-1} [63].

(iv) Evaluation of E_g from the absorption spectra calculated with a fixed α_0 (= 10^3 cm^{-1}, 10^4 cm^{-1}) according to the self-consistent method presented in Subsection 2.2.3.

(v) Self-consistent calculation of E_g with a fixed α_0 and a requirement for the temperature dependence of E_g being linear.

(vi) Self-consistent calculation of E_g with a requirement for the temperature dependencies of both E_g and α_0 being linear.

Each of the procedures above is a theoretical construction which is not substantiated by relevant argumentation. The first three methods have already been reported in the literature and are mentioned for completeness' sake; the published results achieved by utilizing these methods are used for comparison. On the contrary, the last three methods represent new approaches developed at IoP CU in order to improve the calculation of the absorption edge and to give sustainable reasons for such procedures. Applicability of the different methods on the experimental data and discussion of obtained results are the main topics of the following analysis.

In Fig. II.4.4 the temperature dependence of the absorption edge energy of studied samples (see Table II.4.1) evaluated according to the self-consistent procedure (iv) for $\alpha_0 = 10^3$ cm^{-1} is shown. The results for $\alpha_0 = 10^4$ cm^{-1} are not depicted in this figure;

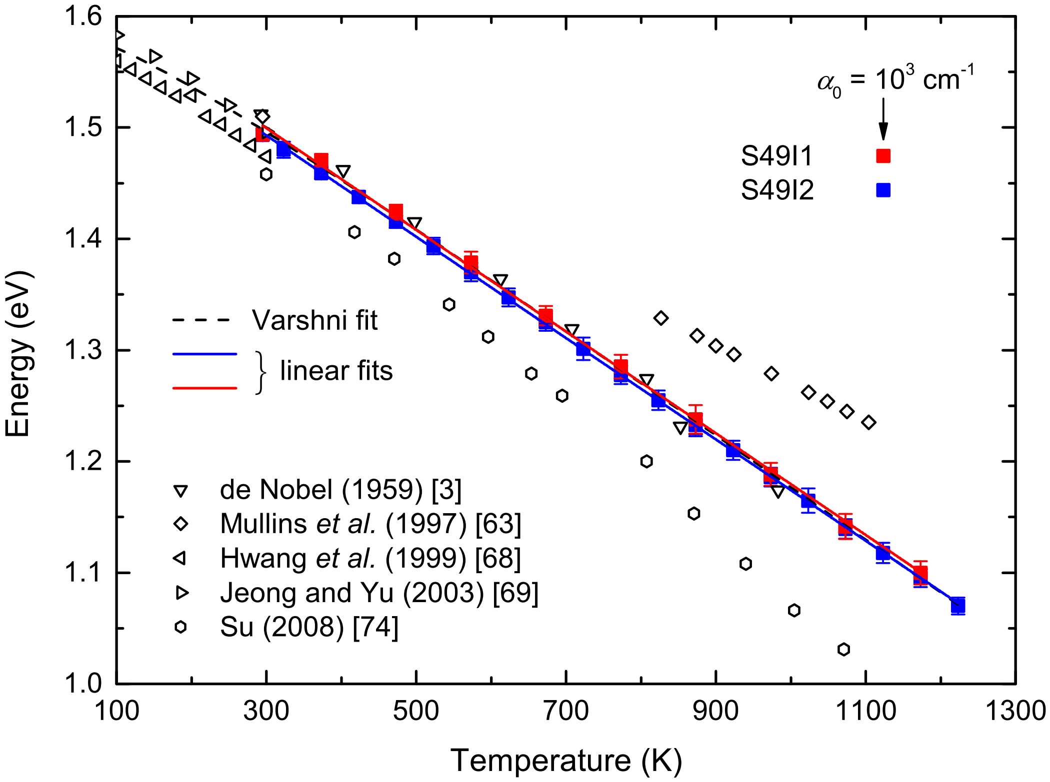

Figure II.4.4: Temperature dependence of absorption edge energy of studied samples evaluated according to the self-consistent procedure from Subsection 2.2.3. Only the results for $\alpha_0 = 10^3$ cm^{-1} are shown. Comparison to published results is given as well.

those for S49I2 are to be found later in Fig. II.4.5. It is clearly seen that calculated points for S49I1 and S49I2 samples follow the same curve in the whole temperature range.

In addition, the results of calculations (i)–(iii) published in the literature are included for comparison. Though it is disputable to extrapolate the above room temperature measurements down to 0 K, the Varshni fit according to Eq. (II.1.1) with the Debye temperature $\beta = 160$ K [74] of S49I1 and S49I2 data fitted together is figured for illustration as well. This fit, although extrapolated from its linear part down to low temperatures, is in good agreement with low temperature data of other authors [3, 68, 69]. The fitting results are shown in Table II.4.2.

Apart from Varshni fit, it is interesting to interpolate the calculated data by a linear function according to Eq. (II.1.4) since for high temperatures it holds that $T \gg \beta = 160$ K and Varshni equation becomes linear anyway. These fits with $T_0 = 300$ K are also to be found in Fig. II.4.4. The results of fitting procedures are summarized in Table II.4.3. Obtained slopes that mostly lie within the interval of $-(3.5\text{–}4.5)\times 10^{-4}$ eV/K are slightly higher of what is reported in the literature where the values of $-(3.0\text{–}3.6)\times 10^{-4}$ eV/K can be found [63]. The published data [63] were, however, determined from the measurements of incandescence spectra in a narrower temperature range 800–1100 K in contrast to presented 300–1200 K transmittance measurements.

Detail analyses of both the self-consistent procedure from Subsection 2.2.3 used for the processing of measurements performed on S49I2 detector and the Pikhtin–Yas'kov dispersion formula (II.2.10) showed that using a self-consistent treatment on present measurements is not necessary as the results of E_g obtained with the iterative procedure involved and without this procedure (assuming that the refractive index is constant, $n = 2.85$,

Table II.4.2: Results of Varshni fits according to Eq. (II.1.1) with $\beta = 160\,\mathrm{K}$ [74] of S49I1 and S49I2 data fitted together. Reported errors represent statistical uncertainty of the fits.

α_0 (cm^{-1})	$E_g(0)$ (eV)	γ (eV/K)
10^3	1.590 ± 0.002	$(4.49 \pm 0.03) \times 10^{-4}$
10^4	1.597 ± 0.005	$(4.04 \pm 0.09) \times 10^{-4}$

Table II.4.3: Results of linear fits according to Eq. (II.1.4) with $T_0 = 300\,\mathrm{K}$. Reported errors represent statistical uncertainty of linear fits.

Sample		S49I1	S49I2
E_g at 300 K (eV)	$\alpha_0 = 10^3$ cm^{-1}	1.499±0.002	1.493±0.001
	$\alpha_0 = 10^4$ cm^{-1}	1.531±0.005	1.507±0.004
$\frac{\mathrm{d}E_g}{\mathrm{d}T}$ at 300 K (10^{-4} eV/K)	$\alpha_0 = 10^3$ cm^{-1}	−4.57±0.06	−4.55±0.02
	$\alpha_0 = 10^4$ cm^{-1}	−4.00±0.13	−3.71±0.09

and not varying with temperature and wavelength) differ only about 1 meV, which is less than the expected error of calculations. The reason for this finding can be explained with the help of Figs. II.2.1 and II.2.2: the thickness ~0.5 mm of studied samples limits the maximum measurable values of the absorption coefficient to ~100 cm^{-1} whereas the absorption edge energy is evaluated at energies corresponding to $\alpha_0 = 10^3$–10^4 cm^{-1} from extrapolation starting as much as 0.1 eV below E_g, see Fig. II.2.2. As seen from Fig. II.2.1, the refractive index n of CdTe changes very little 0.1 eV below E_g in a narrow energy interval used for the exponential extrapolation according to the Urbach rule (approx. 1.41–1.45 eV in Fig. II.2.2) in comparison to the immediate vicinity of E_g (~1.50 eV in Fig. II.2.2) and, within the bounds of estimated calculation errors, n can be considered to be constant up to 100 cm^{-1}. Therefore, one can simply calculate the absorption coefficient of CdTe from Eq. (II.2.9) by supposing $n \sim 2.8$–2.9. The self-consistent method is generally needed for precise calculation of the absorption coefficient on very thin samples when values greater than 10^4 cm^{-1} are directly measurable; since the refractive index changes rapidly close to E_g.

It is remarkable that results obtained for S49I1 and S49I2 samples are in excellent agreement with the results of de Nobel [3] measured 50 years ago. The procedure (i) of de Nobel has been furthermore applied on measured transmittance data from Fig. II.4.2b to obtain results depicted in Fig. II.4.5 by blue diamonds. It is nicely illustrated that this method systematically leads to an underestimation of the bandgap energy, for which there are two reasons easy to understand: (a) because of the Urbach tail the bandgap energy is hidden somewhere in the absorption tail what (b) makes its identification difficult since $\alpha^{(\mathrm{Urbach})}(\hbar\omega = E_g) \gg \alpha^{(\mathrm{interband})}(\hbar\omega = E_g) \sim 0$. Thus the agreement in results is rather accidental.

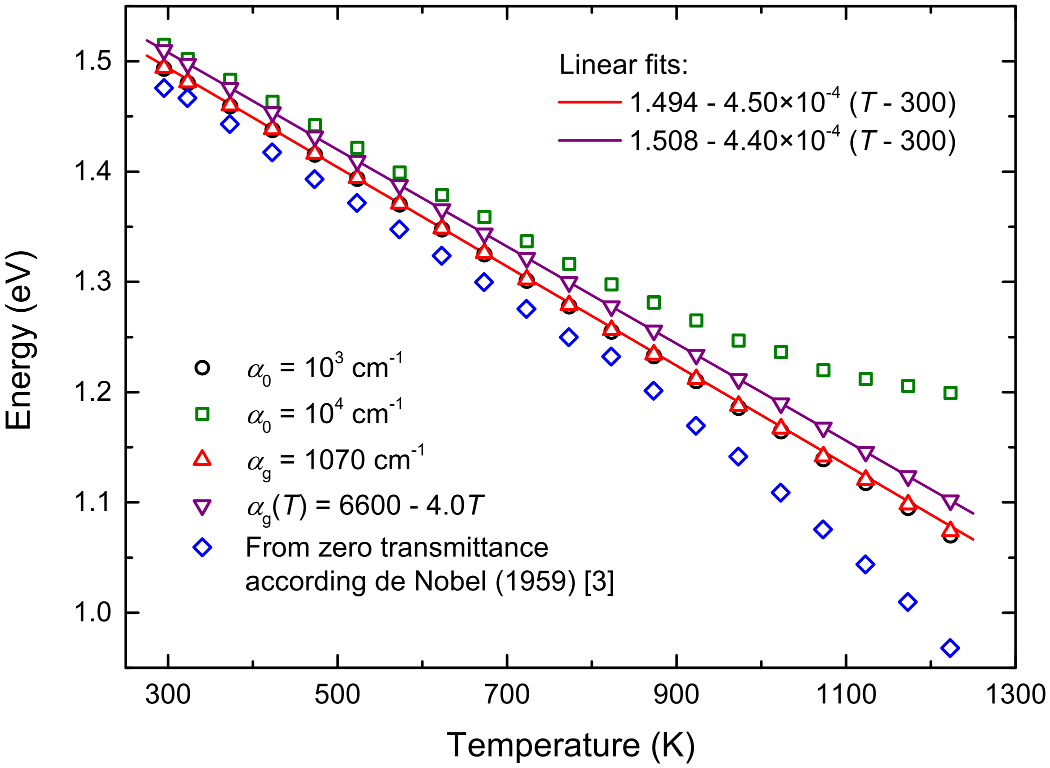

Figure II.4.5: Temperature dependence of absorption edge energy of S49I2 sample evaluated according to different methods discussed in the text. Note that results for $\alpha_0 = 10^3$ cm^{-1} (black circles) and $\alpha_g = 1070$ cm^{-1} (red triangles) are almost identical due to close α_0 to α_g.

To overcome the inaccuracy in the determination of the bandgap energy and to give sustainable reasons for a chosen theoretical construction for indirect calculation of $E_g(T)$, deeper analysis is performed by taking the expected theoretical dependence of $E_g(T)$ into account. The task (v) is completed by supposing that $E_g(T)$ is a linear function of temperature according to Eq. (II.1.4), followed by checking if such an assumption is realizable through the search for a proper α_0 that allows the linearity of $E_g(T)$ to be fulfilled. It has been found that, e.g., the temperature dependence of the absorption edge of S49I2 detector can be excellently described by Eq. (II.1.4) if one sets $\alpha_0 = \alpha_g = 1070$ cm^{-1}. Then, the following relation is obtained:

$$E_{\alpha_g}(T) = 1.494 - 4.50 \times 10^{-4}\big(T\,(\mathrm{K}) - 300\,\mathrm{K}\big) \quad (\mathrm{eV}) \qquad \text{if } \alpha_g = 1070\ \mathrm{cm}^{-1}. \tag{II.4.1}$$

The fit according to the latter equation describes experimental data very well, deviating by less than 2 meV from measured data points in the whole temperature interval. This is clearly shown in Fig. II.4.6. Although this procedure removes problems with “correct” estimation of α_0 as the most suitable value is found via the fitting algorithm, the question still remains about the justification of a constant α_0. This restrictive assumption is thrown away in procedure (vi) from the above list by supposing that α_0 may be temperature dependent, $\alpha_0 = \alpha_g(T)$. Analogously to $E_g(T)$, a linear function is assumed. This treatment resulted in

$$\alpha_g(T) = 6600 - 4.0\,T\,(\mathrm{K}) \qquad (\mathrm{cm}^{-1}) \tag{II.4.2}$$

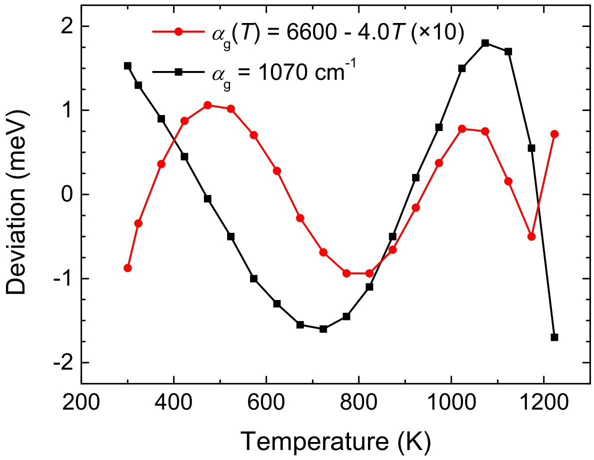

Figure II.4.6: Deviation of the least-square fit of linearly temperature dependent E_{α_g} from the experimental data evaluated for constant $\alpha_g = 1070\ \mathrm{cm}^{-1}$ and for temperature dependent $\alpha_g(T)$ according to Eq. (II.4.2).

and consequently

$$E_{\alpha_g}(T) = 1.508 - 4.40 \times 10^{-4}\big(T\,(\mathrm{K}) - 300\,\mathrm{K}\big) \quad (\mathrm{eV})$$
$$\text{for } \alpha_g \text{ from Eq. (II.4.2).} \qquad \text{(II.4.3)}$$

The presented model with temperature dependent $\alpha_g(T)$ applies well on the experimental data as the deviations from the experiment plotted in Fig. II.4.6 decreased more than ten times in comparison to the case with constant $\alpha_g = 1070\ \mathrm{cm}^{-1}$. It thus can be concluded that $\alpha_g(T)$ and $E_g(T)$ expressed, respectively, by Eqs. (II.4.2) and (II.4.3) represent the best choice for the approximation of real absorption bandgap edge.

The temperature dependence of absorption edge energy determined by different methods is plotted in Fig. II.4.5. It is apparent that constant α_0 less (greater) than $\alpha_g = 1070\ \mathrm{cm}^{-1}$ results in a concave (convex) shape of temperature dependence of E_{α_g}. This finding entails that using constant $\alpha_0 = 10^4\ \mathrm{cm}^{-1}$ according to [63] would not allow to use a linear fit of $E_g(T)$. The same behaviour would be observed for S49I1 sample as well as the linear fit of experimental data processed with $\alpha_0 = 10^4\ \mathrm{cm}^{-1}$ deviates at high temperatures much more from linear dependence than the same data processed with $\alpha_0 = 10^3\ \mathrm{cm}^{-1}$. This implies that optimal constant α_g for this detector is close to $10^3\ \mathrm{cm}^{-1}$ similarly to S49I2, for which this value was estimated to be $1070\ \mathrm{cm}^{-1}$. The treatment with linear $\alpha_g(T)$ could be reproduced analogously for S49I1 detector, however, it is not reported in the text. Nevertheless, due to the similarity of absorption coefficients of S49I1 and S49I2 detectors, one can expect that the temperature dependence of the absorption edge of S49I1 is well described by Eqs. (II.4.2) and (II.4.3).

4.3 Optical and electronic bandgaps

All values of energy band edges evaluated so far represent an “optical” bandgap energy, E_g, corresponding to rapid increase of $\alpha(\hbar\omega)$ induced by direct interband absorption. However, due to the Coulomb interaction of an electron–hole pair created during the single-photon absorption, bound exciton states exist with energy lower than the bandgap. Thus, E_g does not depict the exact “electronic” bandgap energy, E_{ge}, that represents the minimum energy necessary for creation of *free* carriers as the carriers are generated to bound states. E_{ge} can be calculated from the optical bandgap energy under the assumption that the exciton binding energy, E_{ex}, is known, as it holds

$$E_{ge} = E_g + E_{ex}. \qquad \text{(II.4.4)}$$

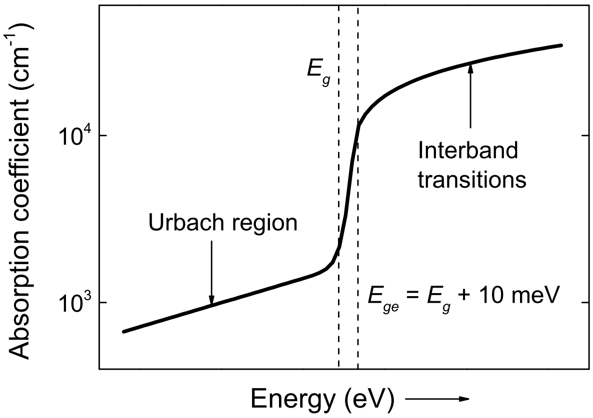

Figure II.4.7: Schematic profile of the spectrum of absorption coefficient near the bandgap energy E_g.

The value of $E_{ex} = 10$ meV observed at low temperatures [70] can be used to recalculate the evaluated optical band edges to the electronic ones. The difference between optical and electronic bandgaps is depicted schematically in Fig. II.4.7. The Urbach exponential tail is followed by an abrupt increase of absorption coefficient above 10^3 cm^{-1} (energy around E_g in Fig. II.4.7) and reaches fast the values above 10^4 cm^{-1} corresponding to interband absorption (energy greater than E_{ge} in Fig. II.4.7). The optical band edge involves the electron–hole Coulomb interaction of 10 meV, which must be taken into account to obtain the electronic bandgap energy. However, due to the estimated error of calculations as well as the calculation itself being an indirect technique, the distinction between the gaps resulting in an additional correction of 10 meV is a theoretical concept rather than a significant correction to calculations.

4.4 Urbach parameter

It is well recognized from Fig. II.4.3 that the absorption coefficient near the absorption edge can be excellently described by the Urbach-like exponential rule according to Eq. (II.2.13) characterized by the slope E_U. The fitting procedure used for the evaluation of the bandgap energy in the previous sections yielded, in addition to $E_g(T)$, the temperature dependence of E_U as well, see Fig. II.4.8a. Although the calculated data deviate not much from the values presented in [63], the overall shape of the dependence is completely different from what was reported therein. In contrast to the original work of Urbach [82] where $E_U \sim k_B T$ was seen on AgBr, it was found on S49I2 sample that $E_U(T)$ is significantly less than $k_B T$ and the temperature dependence is not linear. The similar course of $E_U(T)$ was observed also in $\mathrm{Cd_{0.97}Zn_{0.03}Te}$ and CdS [90], GaAs [91, 92] and InP [92]. A comparison with the exponential temperature dependence of the Urbach parameter proposed in [63] is not much significant since a detail view of the data taken for the analysis [63] raises a query of an adequacy of this result due to unsuitable data range with completely missing mid-temperature data, see Fig. II.4.8a.

The shape of the temperature dependence of the Urbach absorption edge in GaAs was thoroughly studied in [91]. It was argued that the temperature dependencies of both E_U and E_g have the same functional form which consecutively results in a common temperature-independent intersection of extrapolated Urbach absorption edges—the Urbach focus. It was observed in GaAs in the temperature range 350–950 K [91]; in [70] the Urbach focus was reported in CdTe at low temperatures. The same analysis was examined on the data obtained from S49I2 detector (300–1200 K), however, no common intersection was found. On the contrary, the intersections of each two adjacent Urbach

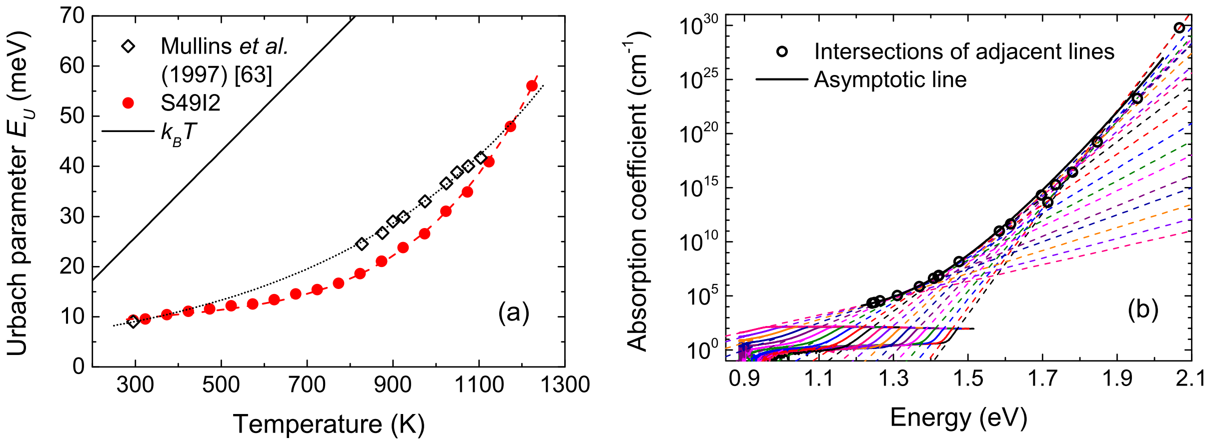

Figure II.4.8: (a) Temperature dependence of the Urbach parameter E_U of S49I2 detector (red points) compared to values from [63]. Dashed red line is the interpolation of experimental data from this thesis; black dotted line represents the data from [63]. (b) Intersections of the extrapolated Urbach parts of the spectra of absorption coefficient (open circles) and the asymptotic line of intersections.

extrapolations were found to form a particular curve that acts as an asymptotic line for extrapolated curves, see Fig. II.4.8b. In addition, analytic expressions for the energy $E_I(T)$ and the absorption coefficient $\alpha_I(T)$ corresponding to the points of intersection, $[E_I(T),\, \alpha_I(T)]$, can be derived, the details of which can be found in [87]. The absence of the common intersection of extrapolated $\alpha(\hbar\omega)$ in the studied sample at high temperatures implies that, in contrast to GaAs, there is no apparent connection between the temperature dependencies of E_U and E_g in this temperature range in CdTe.

4.5 Summary

High temperature measurements of the optical absorption edge of bulk CdTe samples were performed in the temperature interval 295–1223 K by measuring transmittance spectra of samples placed in a fused quartz ampoule within a two zone furnace in order to precisely control the thermodynamic conditions within the ampoule (a Cd overpressure). Several techniques of processing of experimental data were analyzed and compared. Both the experimental and calculation errors were deeply analyzed. Temperature dependence of the optical bandgap energy that best fits the experimental data was found to be linear, defined by the room temperature value $E_g(300\,\mathrm{K}) = 1.508$ eV and the slope $\mathrm{d}E_g/\mathrm{d}T = -4.4 \times 10^{-4}$ eV/K, the values of which were determined by the extrapolation of the spectra of absorption coefficient according to the Urbach exponential rule to the temperature dependent absorption edge at $\alpha_g(T) = 6600 - 4.0T\,(\mathrm{K})\ (\mathrm{cm}^{-1})$. The difference between the optical and electronic bandgaps was discussed. Advanced analysis was performed concerning the temperature dependence of the Urbach parameter with respect to its relation to $E_g(T)$ through the study of the Urbach focus.

Conclusion

The submitted thesis was focused on the study of transport and optical properties of CdTe and CdZnTe samples as a part of the long-standing research being conducted at the Institute of Physics of Charles University in Prague (IoP CU). To accomplish this challenging task new experimental techniques were introduced to the laboratories of IoP CU: the transient-current technique (TCT) and high-temperature measurements of the absorption edge. The improvements of existing experimental setup (in the case of TCT) and development of a new unique setup (in the case of high-temperature measurements) were supplied by the simultaneous development of methods for processing of measured data. These efforts resulted in publication of four papers [25, 26, 27, 87] and provided data for this work where the most interesting results are reported and summarized.

TCT technique was the main topic of Part I of the thesis. As demonstrated, this "electrical" alternative to an "optical" Pockels effect measurement is a simple but powerful technique for investigations of the internal electric field in radiation detectors. General theory for processing of TCT and charge-collection efficiency (CCE) measurements on planar detectors involving single-carrier collection of either electrons or holes regardless of the polarization state of the detector was reported. It should be noted that the conjunction of TCT and CCE measurements into one complex method, the self-consistent procedure (SCP) or the direct-minimization procedure (DMP), both firstly reported in [26], significantly extends the application potential of such analyses. That is enabled also by the fact that standard simple methods commonly used for the evaluation of the mobility–lifetime product represent limiting cases of more general procedures (SCP, DMP). These newly developed procedures are efficient in any situation when the internal electric field can be approximated by a linear profile, no matter if the field extends all over the detector bulk or if there is an inactive region (a dead layer) with zero electric field under the detector contact. In these situations standard methods either fail or give wrong results, however, both the SCP and DMP are applicable as thoroughly demonstrated in the text. Although only several applications of the TCT were demonstrated and studied in this thesis, another ones, including investigations of the electric field at various temperatures or types of excitation (above bandgap laser illumination), are currently being studied or are about to be investigated soon at IoP CU.

In Part II of the thesis high-temperature optical measurements of the temperature dependence of absorption edge are presented. It was for the first time when measurements under a Cd overpressure were performed in order to reduce the sample sublimation or surface degradation, which were the problems affecting measurements of other authors. The optical bandgap energy was estimated from the extrapolation of the Urbach exponential tail in a spectrum of the absorption coefficient. Obtained results of temperature dependencies of both the bandgap energy and the Urbach parameter were compared to published results and deeply analyzed. The experimental setup developed in the laboratory of IoP CU was proven to be efficient for measurements under precise thermodynamic conditions. It is thus reasonable that it will be used in further research at IoP CU, e.g., for the study of pressure dependencies at a fixed increased temperature, from which a defect structure of studied samples can be deduced.

References

[1] F. A. Kröger and D. de Nobel. Preparation and electrical properties of CdTe single crystals. *J. Electron.*, 1:190, 1955.

[2] B. I. Boltaks, P. P. Konorov, and O. A. Matveev. Electrical properties of cadmium telluride. *Z. Tekh. Fiz.*, 25:2329, 1955.

[3] D. de Nobel. Phase equilibria and semiconducting properties of cadmium telluride. *Phillips Res. Rep.*, 14:361, 1959.

[4] C. Szeles, S. A. Soldner, S. Vydrin, J. Graves, and D. S. Bale. CdZnTe semiconductor detectors for spectroscopic X-ray imaging. *IEEE Trans. Nucl. Sci.*, 55:572–582, 2008.

[5] R. B. James, T. E. Schlesinger, J. C. Lund, and M. Schieber. CdZnTe spectrometers for gamma and X-ray applications. In T. E. Schlesinger and R. B. James, editors, *Semiconductors for Room Temperature Nuclear Detector Applications*, volume 43, page 335. New York: Academic Press, 1995.

[6] T. E. Schlesinger, J. E. Toney, H. Yoon, E. Y. Lee, B. A. Brunett, L. Franks, and R. B. James. Cadmium zinc telluride and its use as a nuclear radiation detector material. *Mater. Sci. Eng.*, 32:103–189, 2001.

[7] T. E. Schlesinger and R. B. James. Semiconductors for room temperature nuclear detector applications. In *Semiconductors and Semimetals*, volume 43. San Diego: Academic Press, 1995.

[8] K. Zanio. Cadmium telluride. In R. K. Willardson and A. C. Beer, editors, *Semiconductors and Semimetals*, volume 13. New York: Academic Press, 1978.

[9] A. R. West. *Basic Solid State Chemistry.* New York: John Wiley, 1988.

[10] O. Zelaya-Angel, J. G. Mendoza-Alvarez, M. Becerril, H. Navarro-Contreras, and L. Tirado-Mejía. On the bowing parameter in $\mathrm{cd}_{1-x}\mathrm{zn}_x\mathrm{te}$. *J. Appl. Phys.*, 95:6284–6288, 2004.

[11] P. Norton. HgCdTe infrared detectors. *Opto-electron. Rev.*, 10:159–174, 2002.

[12] U. Roessler. *Systematics of Semiconductor Data.* Springer-Verlag Berlin Heidelberg, 2008.

[13] R. Triboulet and P. Siffert. CdTe and related compounds; physics, defects, hetero- and nano-structures, crystal growth, surfaces and applications. In *Physics, CdTe-based Nanostructures, CdTe-based Semimagnetic Semiconductors, Defects.* Amsterdam: Elsevier, 1st edition, 2010.

[14] M. Bugár. *Doctoral thesis: Dynamics of structural defects in CdTe-based semiconductors.* Institute of Physics of the Charles University, 2011.

[15] J. Schreiber, L. Höring, H. Uniewski, S. Hildebrandt, and H. S. Leipner. Recognition and distribution of A(g) and B(g) dislocations in indentation deformation zones on 111 and 110 surfaces of CdTe. *phys. stat. sol. (a)*, 171:89–97, 1999.

[16] R. Grill and A. Zappettini. Point defects and diffusion in cadmium telluride. *Prog. Cryst. Growth Char. Mater.*, 48–49:209–244, 2004.

[17] E. Belas, M. Bugár, R. Grill, J. Franc, P. Moravec, P. Hlídek, and P. Höschl. Reduction of inclusions in (CdZn)Te and CdTe:In single crystals by post-growth annealing. *J. Electron. Mater.*, 37:1212–1218, 2008.

[18] G. F. Knoll. *Radiation Detection and Measurement.* New York: John Wiley & Sons, 2nd edition, 1989.

[19] J. Dolejší *et al.* Particle physics Textbook, 2006. `http://www-ucjf.troja.mff.cuni.cz/~dolejsi/textbook/Detectors_CZ.ppt` [Online; accessed January 2014].

[20] J. Beringer *et al.* (Particle Data Group). The review of particle physics. *Phys. Rev. D*, 86:010001, 2012.

[21] M. J. Berger and J. H. Hubbell. XCOM: Photon cross sections database. `http://www.nist.gov/pml/data/xcom/index.cfm` [Online; accessed March 2014].

[22] J. H. Hubbell and S. M. Seltzer. X-Ray attenuation and absorption for materials of dosimetric interest. `http://www.nist.gov/pml/data/xraycoef/index.cfm` [Online; accessed March 2014].

[23] A. E. Bolotnikov, G. S. Camarda, G. A. Carini, Y. Cui, K. T. Kohman, L. Li, M. B. Salomon, and R. B. James. Performance-limiting defects in CdZnTe detectors. *IEEE Trans. Nucl. Sci.*, 54:821–827, 2007.

[24] A. E. Bolotnikov, S. Babalola, G. S. Camarda, Y. Cui, R. Gul, S. U. Egarievwe, P. M. Fochuk, M. Fuerstnau, J. Horace, A. Hossain, F. Jones, K. H. Kim, O. V. Kopach, B. McCall, L. Marchini, B. Raghothamachar, R. Taggart, G. Yang, L. Xu, and R. B. James. Correlations between crystal defects and performance of CdZnTe detectors. *IEEE Trans. Nucl. Sci.*, 58:1972–1980, 2011.

[25] Š. Uxa, E. Belas, R. Grill, P. Praus, and R. B. James. Determination of electric-filed profile in CdTe and CdZnTe detectors using transient-current technique. *IEEE Trans. Nucl. Sci.*, 59:2402–2408, 2012.

[26] Š. Uxa, R. Grill, and E. Belas. Evaluation of the mobility-lifetime product in CdTe and CdZnTe detectors by the transient-current technique. *J. Appl. Phys.*, 114:094511, 2013.

[27] Š. Uxa, E. Belas, R. Grill, P. Praus, and R. B. James. Determination of electric-filed profile in CdTe and CdZnTe detectors using transient-current technique. *J. Phys. D: Appl. Phys.*, 46:395102, 2013.

[28] P. Siffert, J. Berger, C. Scharager, A. Cornet, R. Stuck, R. Bell, H. B. Serreze, and F. V. Wald. Polarization in cadmium telluride nuclear radiation detectors. *IEEE Trans. Nucl. Sci.*, 23:159–170, 1976.

[29] R. Matz and M. Weidner. Charge collection efficiency and space charge formation in CdTe gamma and X-ray detectors. *Nucl. Instr. and Meth. A*, 406:287–298, 1998.

[30] A. Zumbiehl, M. Hage-Ali, P. Fougeres, J. M. Koebel, R. Regal, and P. Siffert. Electric field distribution in CdTe and $\mathrm{Cd}_{1-x}\mathrm{Zn}_x\mathrm{Te}$ nuclear detectors. *J. Cryst. Growth*, 197:650–654, 1999.

[31] P. J. Sellin, G. Prekas, J. Franc, and R. Grill. Electric field distributions in CdZnTe due to reduced temperature and X-ray irradiation. *Appl. Phys. Lett.*, 96:133509, 2010.

[32] V. Dědič, J. Franc, P. J. Sellin, R. Grill, and V. Perumal. Study on electric field in Au/CdZnTe/In detectors under high fluxes of X-Ray and laser irradiation. *J. Instrum.*, 7:P02011, 2012.

[33] J. Fink, H. Krüger, P. Lodomez, and N. Wermes. Characterization of charge collection in CdTe and CZT using the transient current technique. *Nucl. Instr. and Meth. A*, 560:435–443, 2006.

[34] K. Suzuki, T. Sawada, and K. Imai. Effect of DC bias field on the time-of-flight current waveforms of CdTe and CdZnTe detectors. *IEEE Trans. Nucl. Sci.*, 58:1958–1963, 2011.

[35] A. Cola, I. Farella, A. M. Mancini, and A. Donati. Electric field properties of CdTe nuclear detectors. *IEEE Trans. Nucl. Sci.*, 54:868–872, 2007.

[36] J. Franc, V. Dědič, P. J. Sellin, R. Grill, and P. Veeramani. Radiation induced control of electric field in Au/CdTe/In structures. *Appl. Phys. Lett.*, 98:232115, 2011.

[37] A. Cola and I. Farella. The polarization mechanism in CdTe Schottky detectors. *Appl. Phys. Lett.*, 94:102113, 2009.

[38] H. Toyama, A. Higa, M. Yamazato, and T. Maehama. Quantitative analysis of polarization phenomena in CdTe radiation detectors. *Jpn. J. Appl. Phys.*, 45:8842–8847, 2006.

[39] K. Suzuki, T. Sawada, K. Imai, and S. Seto. Time-of-flight measurements on schottky CdTe detectors. *IEEE Trans. Nucl. Sci.*, 59:1522–1525, 2012.

[40] S. M. Sze. *Physics of Semiconductor Devices.* New York: John Wiley & Sons, 2nd edition, 1981.

[41] K. Hecht. For the mechanism of the photoelectric primary current in insulating crystals. *Zeits. Phys.*, 77:235–245, 1932.

[42] T. Kubicki, K. Lübelsmeyer, J. Ortmanns, D. Pandoulas, O. Syben, M. Toporowsky, and W. J. Xiao. Calculation of the electric field in GaAs particle detectors. *Nucl. Instr. and Meth. A*, 345:468–473, 1994.

[43] W. H. Press, S. A. Teukolsky, W. T. Vetterling, and B. P. Flannery. *Numerical Recipes in Fortran 77: The Art of Scientific Computing*, volume 1 of Fortran Numerical Recipes. London: Cambridge University Press, 2nd edition, 1997.

[44] I. Kanno. A model of charge collection in a silicon surface barrier detector. *Rev. Sci. Instrum.*, 61:129–137, 1990.

[45] W. Bohne, W. Galster, K. Grabish, and H. Morgenstern. The influence of plasma effects on the timing properties of surface-barrier detectors for heavy ions. *Nucl. Instr. and Meth. A*, 240:145–151, 1985.

[46] W. Seibt, K. E. Sundström, and P. A. Tove. Charge collection in silicon detectors for strongly ionizing particles. *Nucl. Instr. and Meth.*, 113:317–324, 1973.

[47] A. A. Quaranta, A. Taroni, and G. Zanarini. Plasma time and related delay effects in solid state detectors. *Nucl. Instr. and Meth.*, 72:72–76, 1968.

[48] K. N. Yu, C. W. Y. Yip, D. Nikezic, J. P. Y. Ho, and V. S. Y. Koo. Comparison among alpha-particle energy losses in air obtained from data of SRIM, ICRU and experiments. *Appl. Radiat. Isotopes*, 59:363–366, 2003.

[49] M. Zanichelli, M. Pavesi, L. Marchini, and A. Zappettini. Studies on charge collection and transport properties on semi-insulating materials in the presence of a non-uniform electric field. *Solid State Commun.*, 152:1212–1215, 2012.

[50] M. Zanichelli, A. Santi, M. Pavesi, and A. Zappettini. Charge collection in semi-insulator radiation detectors in the presence of a linear decreasing electric field. *J. Phys. D: Appl. Phys.*, 46:365103, 2013.

[51] Y. Eisen, A. Shor, and I. Mardor. CdTe and CdZnTe gamma ray detectors for medical and industrial imaging systems. *Nucl. Instr. and Meth. A*, 428:158–170, 1999.

[52] I. Farella, G. Montagna, A. M. Mancini, and A. Cola. Study on instability phenomena in CdTe diode-like detectors. *IEEE Trans. Nucl. Sci.*, 56:1736–1742, 2009.

[53] U. Lachish. The role of contacts in semiconductor gamma radiation detectors. *Nucl. Instr. and Meth. A*, 403:417–424, 1998.

[54] R. Stibal, J. Windscheif, and W. Jantz. Contactless evaluation of semi-insulating GaAs wafer resistivity using the time-dependent charge measurement. *Semicond. Sci. Technol.*, 6:955, 1991.

[55] R. Grill, E. Belas, J. Franc, M. Bugár, Š. Uxa, P. Moravec, and P. Höschl. Polarization study of defect structure of CdTe radiation detectors. *IEEE Trans. Nucl. Sci.*, 58:3172–3181, 2011.

[56] J. Franc, R. B. James, R. Grill, V. Dědič, E. Belas, P. Praus, G. Prekas, and P. J. Sellin. Influence of contacts on electric field in an au/(cdzn)te/au detector: A simulation. *IEEE Trans. Nucl. Sci.*, 57:2349–2358, 2010.

[57] J. Franc, R. Grill, J. Kubát, P. Hlídek, E. Belas, P. Moravec, and P. Höschl. Influence of space charge on lux–ampere characteristics of high-resistivity CdTe. *J. Electron. Mater.*, 35:988–992, 2006.

[58] G. Fonthal, L. Tirado-Mejía, J. I. Marín-Hurtado, H. Ariza-Calderón, and J. G. Mendoza-Alvarez. Temperature dependence of the band gap energy of crystalline CdTe. *J. Phys. Chem. Solids*, 61:579–583, 2000.

[59] J. Franc, P. Hlídek, P. Moravec, E. Belas, P. Höschl, L. Turjanska, and R. Varghová. Determination of energy gap in $\mathrm{Cd}_{1-x}\mathrm{Zn}_x\mathrm{Te}$ ($x = 0$—0.06). *Semicond. Sci. Technol.*, 15:561—564, 2000.

[60] J. Kubát, J. Franc, V. Dědič, E. Belas, P. Moravec, V. Babentsov, P. Höschl, and R. Grill. Photoconductivity mapping of semi-insulating CdZnTe. *IEEE Trans. Nucl. Sci.*, 58:1953–1957, 2011.

[61] G. Zha, W. Jie, X. Bai, T. Wang, L. Fu, W. Zhang, J. Zhu, and F. Xu. The study on the work function of CdZnTe with different surface states by synchrotron radiation photoemission spectroscopy. *J. Appl. Phys.*, 106:053714, 2009.

[62] R. Grill, J. Franc, P. Höschl, I. Turkevych, E. Belas, and P. Moravec. Semi-insulation Te-saturated CdTe. *IEEE Trans. Nucl. Sci.*, 52:1925–1931, 2005.

[63] J. T. Mullins, J. Carles, and A. W. Brinkman. High temperature optical properties of cadmium telluride. *J. Appl. Phys.*, 81:6374–6379, 1997.

[64] D. T. F. Marple. Optical absorption edge in CdTe: Experimental. *Phys. Rev.*, 150:728, 1966.

[65] J. Camassel, D. Auvergne, H. Mathieu, R. Triboulet, and Y. Marfaing. Temperature dependence of the fundamental absorption edge of CdTe. *Solid State Commun.*, 13:63, 1973.

[66] D. J. Olego, J. P. Faurie, S. Sivananthan, and P. M. Raccah. Optoelectronic properties of $\mathrm{Cd}_{1-x}\mathrm{Zn}x\mathrm{Te}$ films grown by molecular beam epitaxy on GaAs substrates. *Appl. Phys. Lett.*, 47:1172, 1985.

[67] J. P. Laurenti, J. Camassel, A. Bouhemadou, B. Toulouse, R. Legros, and A. Luson. Temperature dependence of the fundamental absorption edge of mercury cadmium telluride. *J. Appl. Phys.*, 67:6454, 1990.

[68] Y. Hwang, Y. Um, H. Kim, G. Jeen, and H. Park. Temperature dependence of the absorption edge of $\mathrm{Cd}_{1-x}\mathrm{Mn}_x\mathrm{Te}$ crystals. *J. Kor. Phys. Soc.*, 34:405, 1999.

[69] T. S. Jeong and P. Y. Yu. Temperature dependence of the photocurrent in p-Type CdTe. *J. Kor. Phys. Soc.*, 43:1101–1104, 2003.

[70] P. Horodyský and P. Hlídek. Free-exciton absorption in bulk CdTe: Temperature dependence. *phys. stat. sol. (b)*, 243:494–495, 2006.

[71] A. El-Mongy, A. Belal, H. El Shaikh, and A. El Amin. A comparison of the physical properties of CdTe single crystal and thin film. *J. Phys. D: Appl. Phys.*, 30:161, 1997.

[72] X. Mathew. Band gap of CdTe thin films—–the dependence on temperature. *J. Mater. Sci. Lett.*, 21:529–531, 2002.

[73] S. Gilliland, J. Gonzáles, H. S. Güder, A. Segura, I. Mora, and V. Muñoz. Pressure and temperature dependence of the band-gap in CdTe. *phys. stat. sol. (b)*, 235:441–445, 2003.

[74] Ch. H. Su. Energy band gap, intrinsic carrier concentration, and fermi level of CdTe bulk crystal between 304 and 1067 k. *J. Appl. Phys.*, 103:084903, 2008.

[75] Y. P. Varshni. Temperature dependence of the energy gap in semiconductors. *Physica*, 34:149–154, 1967.

[76] R. Pässler. Parameter sets due to fittings of the temperature dependencies of fundamental bandgaps in semiconductors. *phys. stat. sol. (b)*, 216:975–1007, 1999.

[77] C. D. Thurmond. The standard thermodynamic functions for the formation of electrons and holes in ge, si, GaAs, and GaP. *J. Electrochem. Soc.*, 122:1133–1141, 1975.

[78] R. Pässler. Comparison of different analytical descriptions of the temperature dependence of the indirect energy gap in silicon. *Solid-State Electron.*, 39:1311–1319, 1996.

[79] R. Pässler. Moderate phonon dispersion shown by temperature dependence of fundamental band gaps of various elemental and binary semiconductors including wide–band gap materials. *J. Appl. Phys.*, 88:2570–2577, 2000.

[80] A. N. Pikhtin and A. D. Yas'kov. Refraction of light in semiconductors. *Fiz. Tekh. Poluprovodn.*, 22:613–626, 1988.

[81] P. Hlídek, J. Bok, J. Franc, and R. Grill. Refractive index of CdTe: Spectral and temperature dependence. *J. Appl. Phys.*, 90:1672–1674, 2001.

[82] F. Urbach. The long-wavelength edge of photographic sensitivity and of the electronic absorption of solids. *Phys. Rev.*, 92:1324–1324, 1953.

[83] M. V. Kurik. Urbach rule. *phys. stat. sol. (a)*, 8:9–45, 1971.

[84] P. Moravec, P. Höschl, J. Franc, E. Belas, R. Fesh, R. Grill, P. Horodyský, and P. Praus. Chemical polishing of CdZnTe substrates fabricated from crystals grown by the vertical-gradient freezing method. *J. Electron. Mater.*, 35:1206–1213, 2006.

[85] P. Risberg. A revision of the term systems for Na I and K I based on hollow-cathode observations. *Ark. Fys.*, 10:583–605, 1956.

[86] David R. Lide. *CRC Handbook of Chemistry and Physics.* Boca Raton: CRC Press/Taylor and Francis Group, 87th edition, 2006.

[87] E. Belas, Š. Uxa, R. Grill, P. Hlídek, L. Šedivý, and M. Bugár. High temperature optical absorption edge of CdTe single crystal. [to be published soon].

[88] M. Bugár, E. Belas, J. Procházka, P. Hlídek, R. Grill, J. Franc, and P. Höschl. Ir transmittance of CdTe after high-temperature annealing. *Nucl. Instr. and Meth. A*, 633:S83–S85, 2011.

[89] R. F. Brebrick and R. Fang. CdTe II: Defect chemistry. *J. Phys. Chem. Solids*, 57:451–460, 1996.

[90] J. T. Mullins, D. M. Huntley, R. C. Aylmore, and A. W. Brinkman. Optical absorption tails in $Cd_{0.97}Zn_{0.03}Te$ and CdS at elevated temperatures. *J. Cryst. Growth*, 184/185:1114–1117, 1998.

[91] S. R. Johnson and T. Tiedje. Temperature dependence of the urbach edge in GaAs. *J. Appl. Phys.*, 78:5609–5613, 1995.

[92] M. Beaudoin, A. J. G. DeVries, S. R. Johnson, H. Laman, and T. Tiedje. Optical absorption edge of semi-insulating GaAs and InP at high temperatures. *Appl. Phys. Lett.*, 70:3540–3542, 1997.